Study on Attitude and Orbit Control Characterization for a CubeSat Equipped with Pulsed Plasma Thrusters

著者	Rodrigo Cordova-Alarcon Jose
その他のタイトル	パルスプラズマスラスタを搭載したキューブサットのための軌道・姿勢制御特性の評価に関する研究
学位授与年度	令和元年度
学位授与番号	17104甲工第476号
URL	http://hdl.handle.net/10228/00007751

STUDY ON ATTITUDE AND ORBIT CONTROL CHARACTERIZATION FOR A CUBESAT EQUIPPED WITH PULSED PLASMA THRUSTERS

A DISSERTATION SUBMITTED TO THE DEPARTMENT OF
APPLIED SCIENCE FOR INTEGRATED SYSTEMS
ENGINEERING OF KYUSHU INSTITUTE OF TECHNOLOGY
IN PARTIAL FULFILLMENT OF THE REQUIREMENTS
FOR THE DEGREE OF DOCTOR OF PHILOSOPHY

by

Jose Rodrigo Cordova Alarcon

May 2019

STUDY ON ATTITUDE AND ORBIT CONTROL CHARACTERIZATION FOR A CUBESAT EQUIPPED WITH PULSED PLASMA THRUSTERS

Approved by:

Mengu Cho (Prof.), Advisor
Kyushu Institute of Technology

Kazuhiro Toyoda (Prof.), [Committee Member2]
Kyushu Institute of Technology

Keiichi Okuyama (Prof.), [Committee Member3]
Kyushu Institute of Technology

Kojyu Hiraki (Prof.), [Committee Member4]
Kyushu Institute of Technology

Date Approved: [May 20, 2019]

ACKNOWLEDGEMENTS

TABLE OF CONTENTS

LIST OF TABLES

LIST OF FIGURES

LIST OF SYMBOLS AND ABBREVIATIONS

AV4	Aoba VELOX IV
AOCS	Attitude and Orbit Control System
LEO	Low-Earth Orbit
EPS	Electric Propulsion System
ACS	Attitude Control System
PPT	Pulsed Plasma Thruster
PIL	Processor-in-the-Loop
HIL	Hardware-in-the-Loop
STM	Structural Thermal Model
MCC	Mission Control Center
LHG	Lunar Horizon Glow

SUMMARY

The spacecraft control systems have played an important role in the accomplishment of complex missions, such as remote sensing, astronomy, orbit transfer maneuvers and rendezvous. Along with the miniaturization and radiation-hardened components, the proposal and launch of CubeSats missions have increased significantly in the last years.

Considering the potential advantage that CubeSats platforms offer for the development and validation of new technologies, this research is aimed to the development and test of attitude and orbit control systems based on electric propulsion system for their usage in Earth orbits and their potential use in a future lunar mission. Recent advances in low-power propulsion systems potentiate CubeSats orbit control capabilities for the extension of their mission lifetime and increase of orbit maneuver range, in order to reach an optimal operational orbit.

As a study case, Aoba VELOX-IV (AV4) satellite is considered for this research. AV4 is a CubeSat mission project developed by Nanyang Technological Institute and Kyushu Institute of Technology. Its launch is programmed in 2019 and it will serve as technology validation platform for a future lunar mission. Because we needed to derive the success criteria of the PPT future lunar mission with 60m/s as ΔV budget and I_{bit} as 0.025 mNs, we analyzed the mission lifetime and orbit maintenance capabilities through numerical simulations, which takes into account the LP165p Moon gravitational field model. Our analysis shows that the deployment of the satellite into different orbits within frozen orbits will not be suitable for a one-year term mission; however, initial orbits whose mission lifetime is below 1 year can be extended with the proposed orbit maintenance strategy.

To verify the attitude and orbit control system (AOCS) in laboratory, an experimental testbed based on an air bearing table was developed. The AV4 sensors, actuators and OBC are placed on the air-bearing table. By implementing a Hardware-in-the-loop simulation strategy, the author demonstrated the validation of the attitude and orbit

control system algorithms in ground by using pulsed plasma thrusters ever achieved in ground. The testing methods used to validate the AV4 AOCS are explained in this thesis.

Finally, the author shows that the AV4 AOCS meets the requirements stablished for the accomplishment of the horizon detection and orbit maintenance in low-Earth orbit (LEO) orbit.

CHAPTER 1. INTRODUCTION

1.1 Problem statement

In recent years, the launch of CubeSats missions have increased because of its low cost, high potential to perform technology demonstration missions, and the accomplishment of complex missions, such as orbit correction, debris mitigation and disposal, transfer orbit maneuvers, formation flying and rendezvous. The utilization of electric propulsion systems (EPS) in CubeSats have allowed them to increase its capabilities to perform orbit maneuvering and attitude control, particularly in outer space mission; however, there has not been reported their performance in previous CubeSat mission with an integrated attitude control system (ACS) based on EPS so far. Moreover, CubeSats mission in Moon require the use of EPS to perform orbit correction maneuvers and guarantee a long-term mission, since they are piggyback from a main mission and their deployment on stable lunar orbit is not guaranteed. Additionally, magnetic actuation cannot be used for attitude control in Moon orbit and reaction wheels cannot be desaturated if they reach their maximum speed, so the use of an EPS become a feasible solution. To demonstrate their performance on ground, the experimental testbeds for the validation and verification of ACS based on EPSs are limited, since those only work in vacuum environments.

1.2 Motivation

The purpose of this research is the demonstration of the momentum reduction capability of CubeSats via pulsed plasma thruster (PPT) ignitions on laboratory, considering the Aoba VELOX IV (AV4) mission as a study case. For this purpose, several testbeds were developed as part of the AOCS development process, including a satellite simulator, processor-in-the-loop testbed and hardware-in-the-loop testbed. Those testbeds will also serve as tools for the validation and verification of AOCS for future missions developed in Kyutech.

Since AV4 will serve as a technology demonstration for a future lunar mission, this research is also aimed towards the numerical demonstration of orbit correction maneuvers capability of CubeSats using PPTs in lunar orbit. The satellite simulator developed for the evaluation of AV4 project was used for this purpose.

1.3 Objectives

- Analysis on the enhancement of lunar orbit lifetime by orbit correction maneuvers, considering the deployment of a CubeSat mission equipped with PPT unit similar to AV4.
- Development of Attitude and Orbit Control System (AOCS) for AV4 satellite as study case, which was conceived to demonstrate the momentum reduction capability using PPT, as well to execute pointing maneuvers for the observation of Earth horizon and perform orbit correction maneuvers by implementing the strategy proposed in the first research objective.
- Development of testing platforms for the validation and verification of the AV4 AOCS
    - Development of a flight simulator for the design and validation of the AV4 AOCS, as well as related mission analysis for other CubeSat projects.
    - Development of a processor-in-the-loop (PIL) testbed based on the Texas Instruments microcontroller TMS320F2807, which is used for the AV4 OBC computer, to verify the AV4 AOCS software written in C programming language.
    - Development of a hardware-in-the-loop (HIL) testbed for the evaluation of the AOCS software performance by using similar and sensors and actuators.

Figure 1.1 illustrates the methodology that was followed during this research in order to accomplish the aforementioned objectives. The development of the AV4 AOCS serves as a platform to carry out the research related with the testing platforms for the validation and verification of AOCS, as well the feasibility analysis for the utilization of EPS in CubeSats to perform orbit correction maneuvers to increase the mission lifetime in Moon orbit.

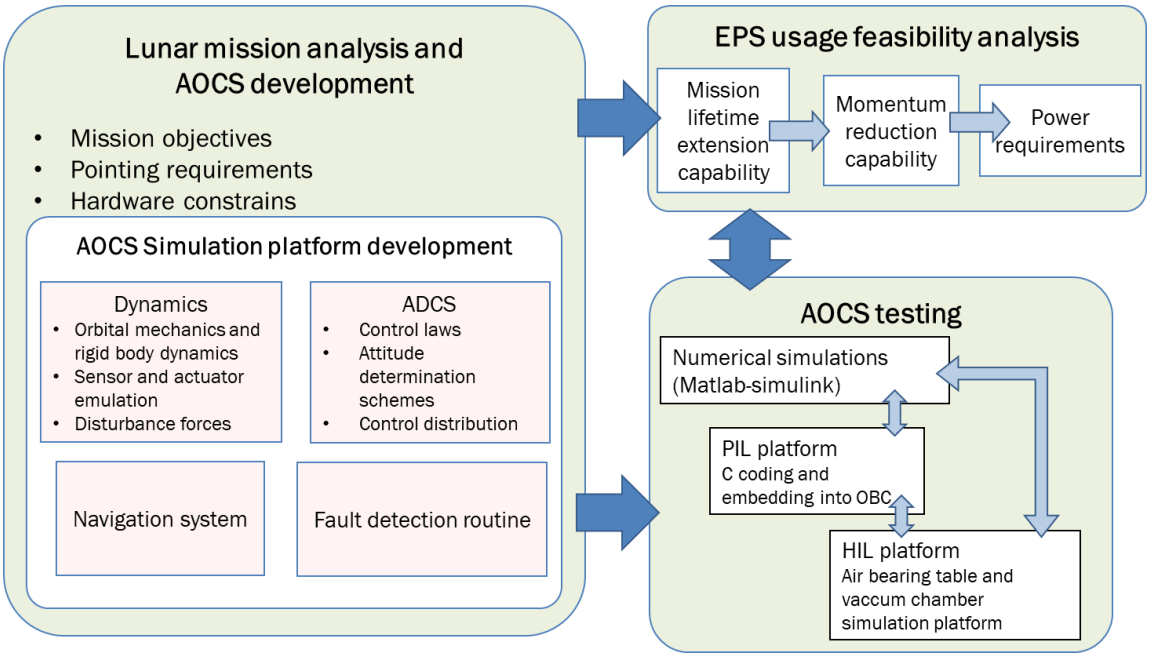

Figure 1.1. Research methodology.

1.4 Thesis Outline

- Chapter 2 is dedicated for the discussion of the up-to-date CubeSat missions launched for the demonstration/utilization of electric propulsion systems. Even when few of them were launched successfully, none of them have reported the on-orbit performance of their electric propulsion systems. This chapter also covers the current status of the technology developed for the experimental verification of the ACS, where the air-bearing table is the most popular platform used for this purpose; however, operating those platforms in vacuum environment is very challenging. It is reported one platform whose operation is based on magnetic levitation, which it was possible to test the performance of an electric propulsion system in vacuum environment.
- Chapter 3 covers a general description of the AV4 project and its subsystems, as well as the requirements of the AOCS for the execution of its scientific mission objectives, which are aimed towards a future lunar mission for the observation of the lunar horizon glow (LHG). Based on the AV4 mission objectives and the

required attitude maneuvers to align the AV4 payloads to a target attitude, the AOCS software and modes of operation were designed and its main components are described in this chapter too.

- Chapter 4 introduces the mathematical models of the dynamics of a spacecraft in orbit, such as orbital mechanics, rigid body dynamics, and time. With this mathematical models, a basic satellite simulator was developed and utilized for numerical analyses related with orbit and attitude disturbances, mission lifetime, AOCS stability and performance, sizing of sensor and actuators, and other applications for other projects.
- Chapter 5 describes the algorithms implemented in the AV4 AOCS, which includes the information of inputs, outputs, and the AOCS modules such as fault detection, navigation, attitude determination, attitude control and actuators command.
- Chapter 6 is dedicated for the research performed for the analysis of the mission lifetime extension capability of a CubeSat equipped with PPT unit in Moon orbit. Since the Moon possess an irregular gravity field, there are ranges of unstable orbits that shorten the orbit lifetime of any spacecraft. Therefore, this analysis serves as a guideline to define the optimal orbits which the future lunar mission can be deployed, as well as the features of its propulsion system to perform orbit correction maneuvers in order to increase its mission lifetime.
- Chapter 7 covers the testbeds developed for the validation and verification of the AV4 AOCS software, including the outcomes obtained throughout the testing campaign to verify the stability and performance of the AOCS software embedded into de AV4 OBC firmware.
- Chapter 8 is dedicated for concluding remarks and future work that can be performed to continue this research.

CHAPTER 2. BACKGROUND

2.1 Types of propulsion systems for small satellites and CubeSats

The increasing demand on complex satellite missions based on CubeSats taking advantage of their dimensions, development cost and simplified development and deployment, have led to the need of development of propulsion systems onboard. These propulsion systems can be used for active attitude control, reaction wheel desaturation, orbit maintenance, rendezvous and docking, in either Earth or interplanetary missions. The required delta-V (ΔV) for proposed missions ranges on the order of m/s for ACS desaturation and small orbit correction maneuvers to several km/s for interplanetary missions [1].

In this section, the propulsion systems developed for CubeSats are categorized, as shown in Table 2.1, as chemical, electric and propellant-less [2].

Table 2.1 List of propulsion systems developed for small satellites CubeSats.

Category	Product	Thrust	Specific Impulse (s)
Chemical	Hydrazine	0.5 – 30.7 N	200-235
	Cold Gas	10 mN – 10 N	40 – 70
	Alternative (Green) Propulsion	0.1 – 27 N	190 – 250
Electric	Pulsed Plasma and Vacuum Arc Thrusters	1 – 1300 μN	500 – 3000
	Electrospray Propulsion	10 – 120 μN	500 – 5000
	Hall Effect Thrusters	10 – 50 mN	1000 – 2000
	Ion Engines	1 – 10 mN	1000 – 3500
Propellant-less	Solar Sails	0.25 – 0.6 mN	N/A

Many of the requirements stated in current version of the CubeSat Standard (Version 13) impose constraints in the development of propulsion systems. Particularly the requirement 3.1.3 of the CubeSat Design Specifications specify that no pyrotechnics are permitted on a CubeSat without a waiver. Additionally, limits on the amount of stored chemical energy with which a CubeSat can be launched (100 W-Hours) significantly decrease the amount of chemical propellant that can be launched onboard a CubeSat. For example, 100 W-Hours

is equivalent to 360 kJ of stored energy, equivalent to 0.019 kg of hydrazine, a common monopropellant for spacecraft. Therefore, a waiver to launch a CubeSat with sufficient chemical propellant would be required, in order to perform any sort of orbital maneuver or reaction wheels desaturation. So far, no waivers have been granted for CubeSats launched as secondary payloads from P-PODS. There are other limitations imposed to CubeSats in general rather than those inherent to the propulsion system. These include the use of hazardous materials, material outgassing, magnetic field strength outside the CubeSat envelope, and maximum mass of a CubeSat [1].

Therefore, Due to their high specific impulse (> 500 s), relative low power consumption (< 10 W), dimensions (< 0.5 U) and fewer regulations of hazardous materials, this research focuses on low-thrust EPSs such as pulsed plasma thrusters (PPT), Vaccum Arc Thrusters (VAT) and electrospray thrusters

2.2 CubeSats missions using electric propulsion systems

In recent years, CubeSats missions have become more demanding due to the fact that those are developed with relative low budget, along with the growing interest to carry out technology demonstration missions for their utilization in further missions that involves even more complex operations, including formation flying and interplanetary missions. For this reason, the demand of low-thrust propulsion systems has increased considerably, in such a way that those are available on market. However, most of these propulsion systems for CubeSats are more expensive than the cost of the satellite itself and may not be affordable for neither academic institutions nor start-ups. Because of the mass, size, and usage of hazardous material constraints, limited types of propulsion systems for CubeSats have been utilized, such as cold gas propulsion thrusters, electrospray thrusters, vacuum arc thrusters (VATs) and Pulse Plasma Thrusters (PPTs) [3].

Cold gas propulsion thrusters consist on pressurized tank or a self-pressurization feed system between the propellant tank and the nozzle. Without combustion, the gas is depressurized to the nozzle and creates an impulsive force. A power supply is required to control the valves and power up the thermal control system to keep the temperature of the propellant within minimum levels of operation [3]. In Figure 2.1, an example of a commercialized cold-gas propulsion system is shown.

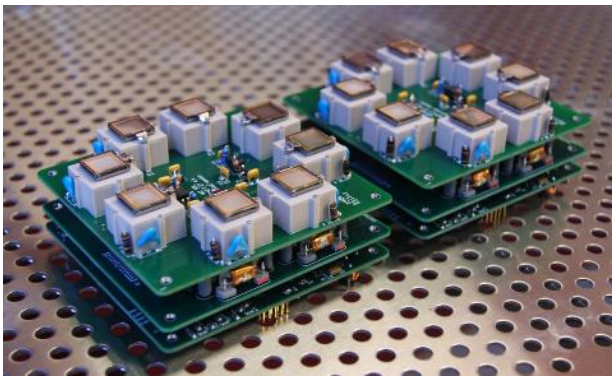

Figure 2.2 An EPT (iEPS) system developed in the Space Propulsion Laboratory at Massachusetts Institute of Technology (MIT), United States, United States (source: http://spl.mit.edu/electrospray-thruster-engineering)

Electrospray thrusters produce their impulsive force by ejecting high-velocity charged particles and/or ions. A strong electric field is applied by electrodes aligned precisely, where the transported liquid's surface tension is overcome, in such a way that the liquid's meniscus becomes a conic shape, where expelled particles are produced [4]. One example of this type of thruster is shown in Figure 2.2, which was developed in the MIT, PPTs create a pulsed, high-current discharge across the exposed surface of the propellant, ionizing and accelerating the vaporized propellant particles to high speeds. In order to create such discharges, a capacitor is charged and discharged approximately once every

Figure 2.1 A cold-gas micro propulsion system developed by VACCO industries (source: http://www.cubesat-propulsion.com/jpl-marco-micro-propulsion-system/)

second and each pulse last few micro-seconds [5]. The Figure 2.3 shows a PPT unit developed and commercialized by Clyde Space Ltd.

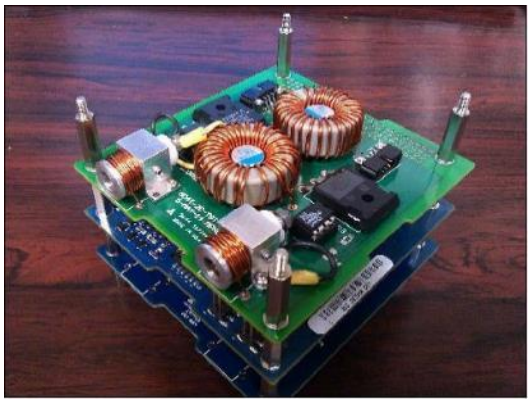

Figure 2.4 The VAT (μCAT) developed by the Micro-propulsion and Nanotechnology Laboratory at the George Washington University, United States (source: https://directory.eoportal.org/web/eoportal/satellite-missions/b/bricsat-p)

VATs use vacuum arcs to produce high-velocity plasma jets directly or accelerated electrostatically from another sources of plasma. The propellant is an ablated cathode material where ionized plasma is created efficiently from the cathode arcing [3]. In Figure 2.4, a VAT denominated μCAT is shown, which was developed in the Micro-propulsion and Nanotechnology Laboratory at the George Washington University.

Recently, several CubeSat missions equipped with low-thrust propulsion system have been launched for their demonstration of either orbit correction or attitude control capability; however, the details of their performance on orbit is limited or not available.

In Table 2.2, the list of CubeSats missions equipped with an electric propulsion system is presented. For example, Illinois Observing Nanosatellite (ION) is a 2U CubeSat equipped with VAT and developed by the University of Illinois, but unfortunately the launch was not successful in 2006 due to failure in the Dnepr rocket [3]. The KKS-1 is an educational CubeSat developed by Tokyo Metropolitan College of Industrial Technology equipped with 3-axis micro-thrusters (μLPs) that was launched in 2009, but its in-flight operation could not be performed due to a satellite trouble [6]. STRaND-1, a 3U CubeSat, was developed by SSTL and Surrey Space Centre and launched in 2013 but communications failed after 5 weeks of operations. It was equipped with a PPT unit

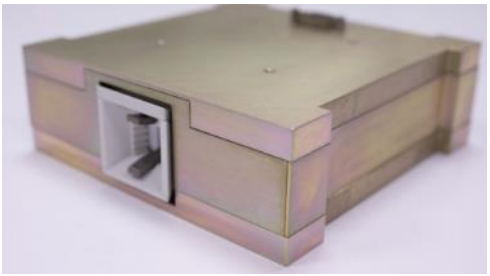

Figure 2.3 The PPT unit developed by Clyde Space Ltd. (source: https://www.clyde.space/products/50-cubesat-pulsed-plasma-thruster)

as part of its payloads [7]. WREN is a femto-satellite (5cm x 5cm x 5cm) satellite developed by the start-up company Stadiko for the testing of a miniaturized PPT unit, but only beacon signals have been received [8]. AeroCube 8A-D mission, launched in 2015, consists of two 1.5U CubeSats equipped with electrospray thrusters (EPTs) developed by the MIT, United States. No information regarding the operation on orbit has been presented the public domain [7]. BRICsat-P is a 1.5U CubeSat developed by US Naval Academy Satellite Lab in collaboration with George Washington University. It is equipped with a micro-cathode arc thruster (μCAT) and was launched in 2015. It is reported that BRICSat-P satellite achieved an angular momentum reduction from 30 º/s within 1.5 º/s after 48 hours by utilizing its thruster, but no details have been reported so far [9]. SERPENTS is a 3U CubeSat developed by the SERPENS (Sistema Espacial para Realização de Pesquisa e Experimentos com Nanossatélites) university consortium and deployed in 2015 from ISS, for the testing of a PPT unit [10]. The 2U CubeSat Aoba-VELOX 3, developed by NTU Singapore and Kyutech Japan, was launched on 9th December 2016 and was deployed from the International Space Station (ISS) on 16 January 2017. This 2U CubeSat satellite is used to demonstrate the operation of PPT for attitude control and orbit maintenance [11]. PEGASUS is a 2U CubeSat was developed by Fachhochschule Wiener Neustadt as part of the QB50 project and launched in 2017. It is equipped with PPT information related to its operations is not available so far [12].

Table 2.2 List of small satellite missions which used an electric propulsion system.

Product	**Developer**	**Satellite**	**Size**	**Year**
VAT	University of Illinois	Illinois Observing Nanosatellite (ION)*	2U	2006
μLP	Tokyo Metropolitan College of Industrial Technology	KKS-1	$15cm^3$	2009
PPT	SSTL	STRaND-1	3U	2012
PPT	Stadoko UG	WREN*	$5cm^3$	2013
EPT	MIT	AeroCube 8A-D	1.5U	2015
uCAT	US Naval Academy Satellite Lab	BRICsat-P	1.5U	2015
PPT	SERPENS	SERPENS	3U	2015
PPT	NTU	AOBA-VELOX 3	2U	2016

µPPT	Fachhochschule Wiener Neustadt	PEGASUS	2U	2017
NanoFEEP/gallium propellant	TU Dresden/Morpheus	UWE-4	1U	2018

*FEEP: Field Emission Electric Propulsion

2.3 Experimental testing platforms of attitude control systems

The verification process of an attitude control system (ACS) for a spacecraft is usually performed by utilizing experimental testing platforms, which provide reliability to the overall spacecraft system. In this research, the Hardware-in-the-Loop (HIL) simulation technique as a verification method for spacecraft's ACS is addressed. The HIL test provide the ACS designer with the capability of verifying several parameters of reliability, performance and robustness of several ACS modules in simulated space environment conditions. In this regard, several approaches have been implemented, such as air bearings, three axis gimbals, pinata rigs, underwater vehicles and zero G-flights, being the air bearings the most popular, despite of their limited degrees of freedom in their 2 axes. Up to date, several variations of testing platforms based on air bearings were developed for the verification of ACS developed for formation-flying and rendezvous missions, where additional degrees of freedom (lineal and rotational) are included. For CubeSat missions, HIL testing methods are usually skipped and ACS testing is limited only by a reduced functional test, due to the required resources and high cost facilities which usually is unsustainable for university projects; however, if the testing platform is flexible enough, their investment is thus justifiable.

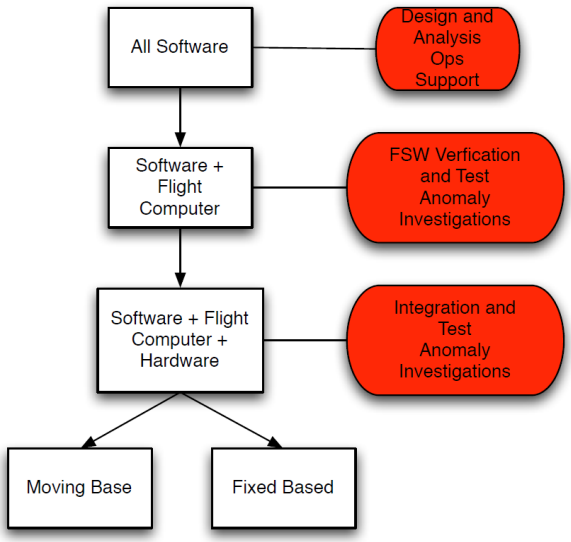

Figure 2.5. ACS design phases.

The hardware-in-the-loop method

The Attitude Control System (ACS) cannot be fully verified in real conditions before flight because the flight hardware cannot be directly submitted into space environment. Therefore, a complete validation and verification process is followed during the development of the ACS, from numerical modeling and simulation to the integration of the flight hardware into the spacecraft. Within the ACS testing phases (Figure 2.5), the Hardware-In-the-Loop (HIL) test technique can be considered as a verification process which provides reliability to the developed ACS integrated by flight hardware [13] [14].

The HIL testing platform is a hybrid software - hardware simulation architecture, where real sensors and actuators are included in the simulation loop. Several variations of a HIL test can be implemented by including some of the ACS hardware elements of the fully integrated system. By performing simulations by utilizing a HIL testing platform, unexpected behaviors and/or failures arising from the integration of the component in the global system can be detected [15]. The HIL test provide the ACS designer with the capability of testing the whole mission, assessing different ACS design modules in the presence of external effects from other ACS modules as typically performed within a numerical simulation, except for the use of a simulation of the space environment without threatening the real system, and verifying several parameters of reliability, performance and robustness [16]. In Figure 2.6, the typical configuration of a HIL test platform is shown.

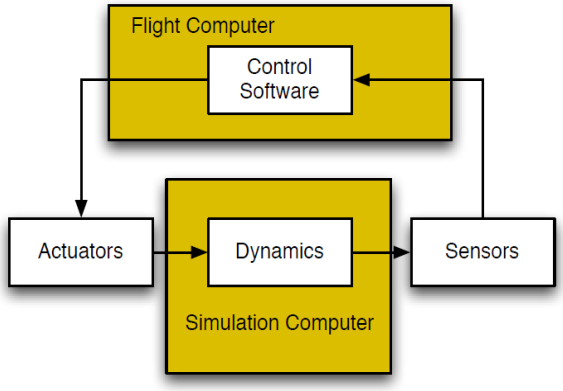

Figure 2.6. General architecture of a HIL testbed.

Several types of testing platforms that reproduce the space environment conditions and used for the verification of attitude determination and control systems have been utilized, including (Figure 2.7):

- Air bearings
- Three axis gimbals
- Pinata Rigs
- Underwater vehicles

- Zero-G flights

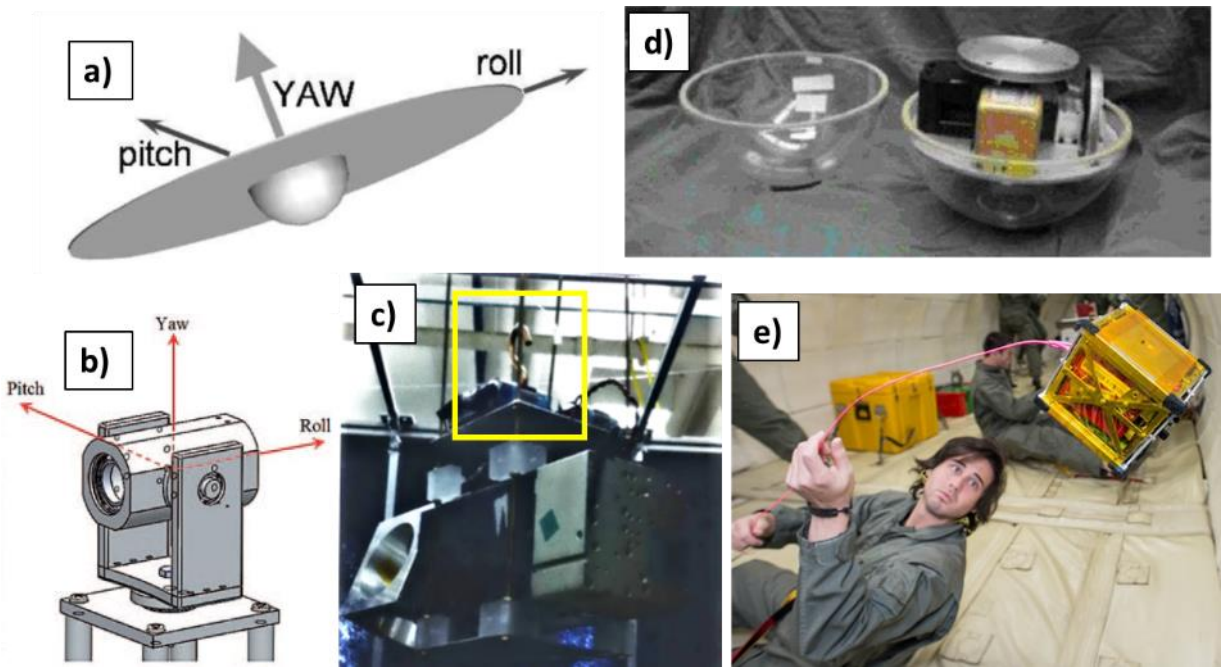

Figure 2.7. Types of experimental testing platforms. a) Air bearing [16]. b) 3-axis gimbal [62]. c) Piñata rig [63]. d) Underwater vehicle [64]. e) Zero-G flight [65].

In this research, air bearing-based platforms are considered, which have been used for spacecraft attitude determination and control hardware verification and software development for nearly 50 years, almost coincident with the beginnings of the space race [17]. Despite of its notorious constrains in terms of angular displacement, they provide three-axis angular movement in a frictionless environment, similar to the outer space. Because it is well known that there are many disturbance-torques on the system, such as atmospheric drag, small bearing friction and gravity center offset, those disturbance sources must be modeled in order to validate the testing environment and minimized until becoming compatible with the torque normally found in the space environment [18].

The air bearing operation principle consists on pressurized air passing through small holes in the grounded section of the bearing, creating a thin film between the ground and the moving element where the spacecraft instrumentation is placed. Thus, the air film becomes an effective lubricant. An air bearing platform can support a total mass of several kilograms

with a relative flow rate. The two elements of the air bearing platforms are portions of concentric spheres, machined and lapped to small tolerances [17].

Several variations of air-bearing based testing platforms have been implemented in order to fulfil a particular requirement of the verification testing campaign. In Figure 2.8a, a traditional configuration of an air bearing table is shown, where it is possible to test an ACS for a spacecraft equipped with reaction wheels and magnetic torque rods [13]. A miniaturized version of an air-bearing testing platform is shown in Figure 2.8b, where it was designed to verify the attitude control algorithms for CubeSats [19]. For advanced applications such as formation flying, rendezvous and docking, a planar air bearing was included. The testbed showed in Figure 2.8c has two separate air bearing environments: a spherical air bearing with three rotational degrees of freedom and a planar air bearing with one rotational and two translational degrees of freedom [20]. In Figure 2.8d, this test-bed was used for validation of the control strategy for a free-floating robot performing rendezvous maneuvers [21].

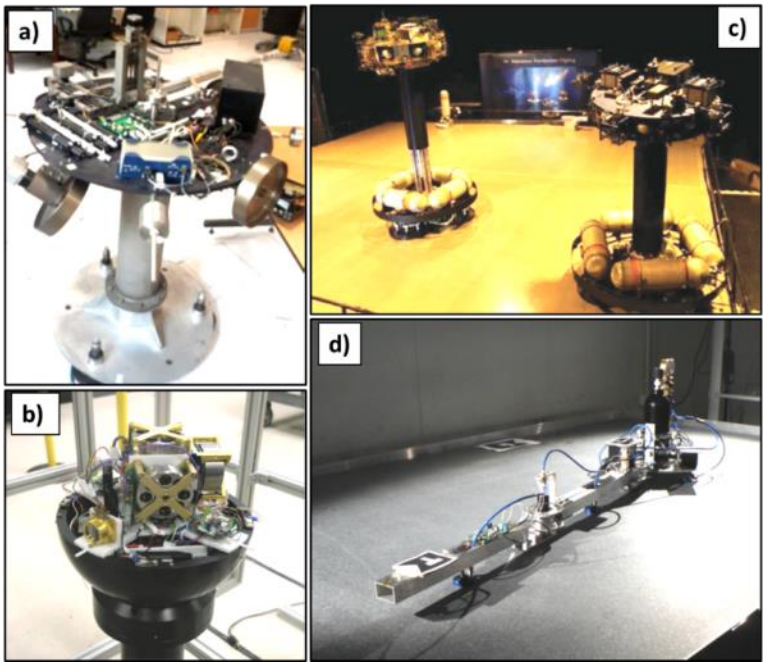

Figure 2.8. Variations of air-bearing based test platforms. a) Traditional air-bearing testbed. b) Miniaturized version. c) Formation-flying testbed including planar air-bearings. d) Rendezvous and docking testbed.

For CubeSat programs, the verification test is often performed by only numerical simulations with no HIL. Usually CubeSats functional test is carried out in ambient condition; then, they are tested under the environmental tests, followed by a reduced functional test. CubeSat's functional test in orbit-like conditions is rarely performed because it would require resources and facilities at high cost which usually is unsustainable for university projects. Additionally, the operational orbit is usually unknown when the CubeSat is in the early stages of its development; therefore, reproducing the possible orbit

conditions in ground would result in a big effort in terms of budget and time. For this reason, HIL approach represents the right balance between performance and cost of the testing activity [15].

A typical configuration of a HIL platform consist on the following elements:

- Air bearing-based platform
- Unit under test
  - Spacecraft, or
  - Spacecraft's ACS prototype and OBC, or
  - General-purpose ACS (including sensors, actuators and OBC)
- Power unit
  - Included in the spacecraft
  - Battery pack
- Data acquisition system
  - Ground station, or
  - Wireless communication system
- Additional space environment simulators (optional)
  - Magnetic field simulator
  - Sun simulator

If the HIL simulation platform is flexible enough (e.g. considering a general-purpose ACS as the unit under test), it can be used for several spacecraft projects and not only for a specific mission, thus the investment can be justified [15].

Several reports related with experimental test campaigns of EPS for CubeSats are published. So far, it is only reported an experimental testbed based on magnetic levitation system, actuated with electrospray thrusters in vacuum environment (one axis is controlled), where the capability of an EPS for attitude control was demonstrated (Figure 2.9).

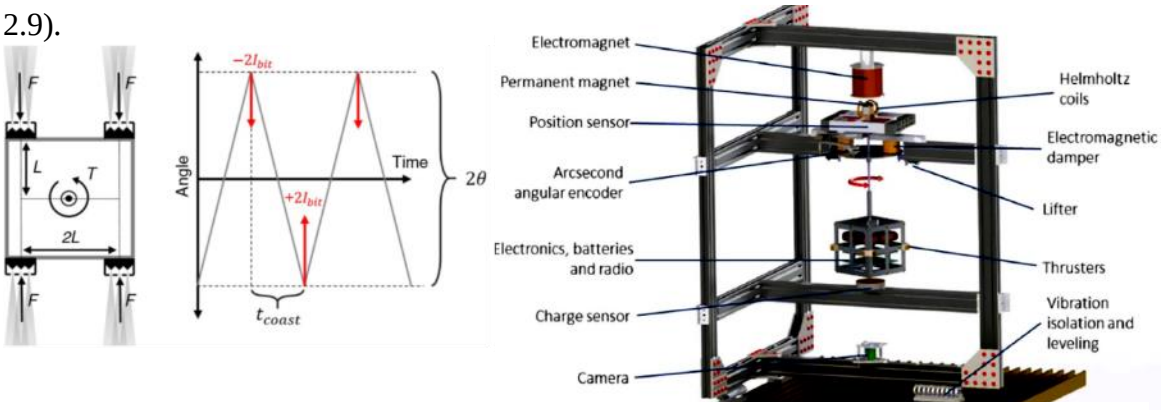

Figure 2.9. Attitude Control system testing platform in vacuum environment

CHAPTER 3. AOBA VELOX MISSIONS

Aoba VELOX-IV (AV4) is a two-unit CubeSat (Figure 3.1), which will serve as technology demonstration platform for the development of a future lunar mission, whose main mission objective is envisaged to carried out investigation of the Lunar Horizon Glow (LHG) and provide evidence of the observations of previous missions.

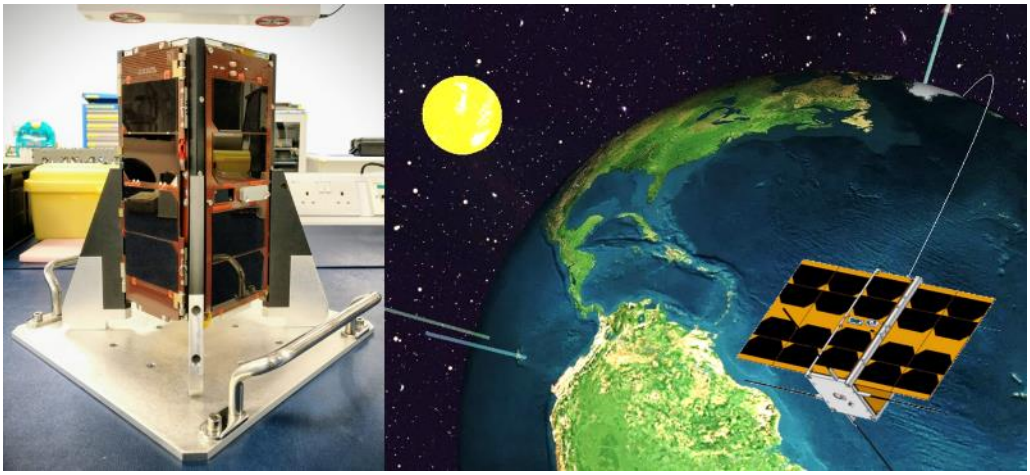

Figure 3.1 AV4 satellite

The first observations of LHG comes from Surveyor missions in 1966 and 1968 by onboard TV cameras while monitoring western horizon after the sunset (Figure 3.2), and the analysis of Surveyor images has suggested that dust grains with ~5μm radius were present in the heights of 3-30cm above the lunar surface [22] [23]. In addition, Apollo astronauts reported that they also witnessed the LHG [24]. Unexpected excess brightness appeared in several photographic sequences from Apollo missions, which was unrelated to the inner coronal and zodiacal light (CZL), but instead was associated with the lunar horizon. Glenar, D. A. analyzed the photographic sequences taken by Apollo mission and produced a quantitative picture of the exospheric dust distribution at the location and time of the Apollo 15 orbital sunset measurements, concluding that there does not appear to be a correlation between the detection or non-detection of horizon glow and any particular solar UV or solar plasma condition [25]. In the other hand, Apollo 17 astronauts observed and sketched the CLZ and LHG at 110 km altitude while approaching the orbital sunrise (Figure 3.3) [26], but since Apollo era, LHG has not been observed. The Lunokhod-II

astrophotometer also detected a brighter twilight as expected. It is assumed that meteoroid impact plumes may play an important role in the generation of vast population of lunar dust, enough to produce the LHG [27]. Therefore, LHG may be a high varying phenomenon whose physical mechanism is still investigated.

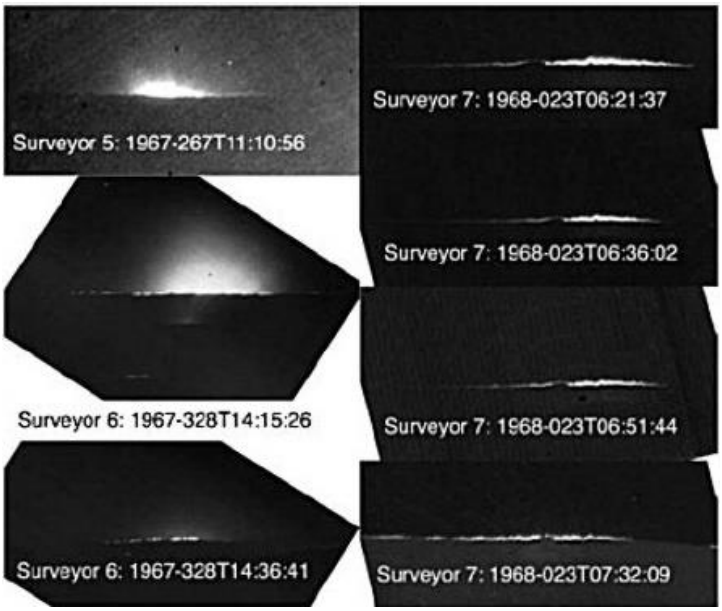

Figure 3.2 Images of LHG taken by Surveyor missions (Source: NASA photos, Criswell, 1973; Rennilson and Criswell, 1974; Colwell et.al.,2007)

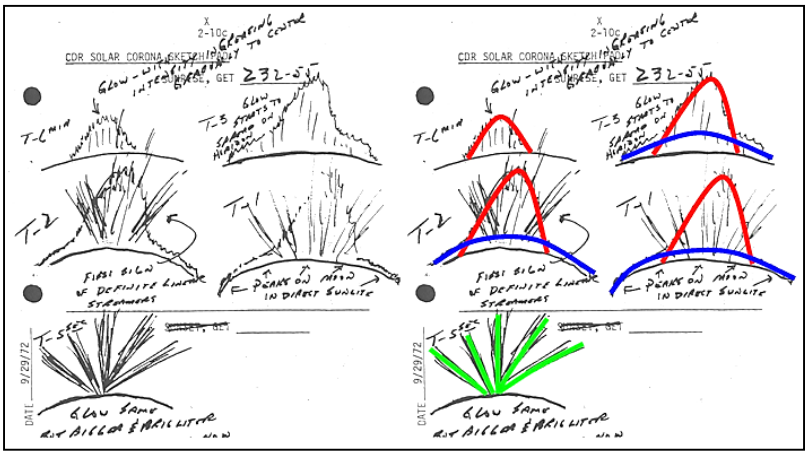

Figure 3.3 A sketch by Apollo 17 astronaut Eugene Cernan. Coronal and Zodiacal Glow in Red Line (CZG), Lunar Horizon Glow (LHG) in blue line, crepuscular rays in green lines formed by shadowing and scattered light. Stubbs, T. J. et.al. 2007

AV4 is the second joint satellite program between Nanyang Technological University (NTU Singapore) and Kyushu Institute of Technology (Kyutech), which will be launched by Japan's national agency, the Japan Aerospace Exploration Agency (JAXA) in 2018. AV4 project consists on the technology demonstration of AOCS capabilities based on 3-axis reaction wheels and pulsed plasma thrusters (PPT) developed by NTU, for orbit maintenance capabilities and attitude control maneuvers, as well as the usage of a COTS monochrome low-light camera for the observation of the LHG. To accomplish this objective, several technological issues shall be covered to demonstrate the feasibility of the use of a CubeSat platform for such mission. Therefore, the next mission success criteria were proposed to be met in this technology demonstration mission:

Minimum Success Criteria:

- Obtain on-orbit data regarding momentum dumping of angular momentum via PPT
- Obtain on-orbit data regarding orbit maneuvering capability via PPT
- Capturing images of horizon while passing from day side to night side

Full Success Criteria:

- Momentum dumping of 0.0001 (Nms) angular momentum around short axis via PPT within 1 hour
- Orbit maneuvering of ΔV=80m/s via PPT in 1 year
- Capturing several images of the horizon as sequence while passing day side to night side
- Capturing Earth night view image via low-light camera

Extra Success Criteria:

- Achieve more than ΔV=80m/s of orbit maneuvering via PPT
- Capturing the Earth-rim image with upper-atmosphere luminous phenomena such as aurora from the eclipse side via low-light camera
- Proliferation of low-light camera image and obtain new science data from the image

For a safe operation, AV4 satellite considers three main modes of operation, which are determined mainly by the battery level: Normal mode, safe-hold mode and survival mode (Figure 3.4). During normal mode, the satellite will perform its mission task normally. In case that the battery levels reach a minimum threshold value, the satellite will change to safe-hold mode and the satellite will align its solar paddles towards the Sun. In case that the battery level reaches a critical value, the satellite will change its mode of operation to survival mode and only its critical subsystems will be enabled. Only by ground station command, the satellite can recover its normal mode of operation.

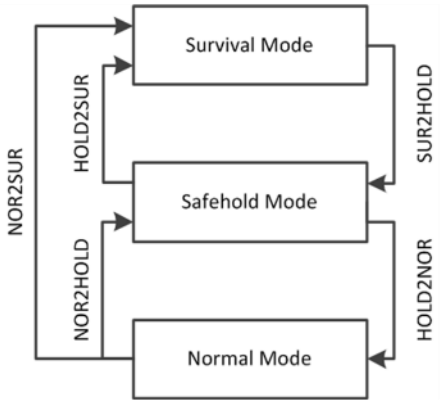

Mode Change	Condition
SUR2HOLD	GS Uplink Command
HOLD2NOR	GS Uplink Command
NOR2HOLD	GS Uplink Command or Vbat < Vth1
HOLD2SUR	Vbat < Vth2
NOR2SUR	Vbat < Vth2

Figure 3.4 AV4 modes of operation

To meet the aforementioned success criteria, an AOCS scheme is proposed. In the next sections, details about the AOCS is mentioned.

3.1 AV4 AOCS Features

The AOCS is designed to meet the AV4 mission requirements for a low-Earth-orbit (LEO) and directly applicable to a lunar mission (Figure 3.5). Pointing towards Earth horizon to observe sunrise and sunset and orbit maintenance tasks to increase the AV4 mission lifetime can be performed by the AOCS. The AOCS hardware consists on coarse and fine sun sensors, gyroscope, reaction wheels (RW) and PPTs. Satellite position and reference time will be determined by ground station via two-line element (TLE) information and the satellite will propagate them until the next revisit. The AV4 AOCS can also desaturates the RW during attitude control maneuvers.

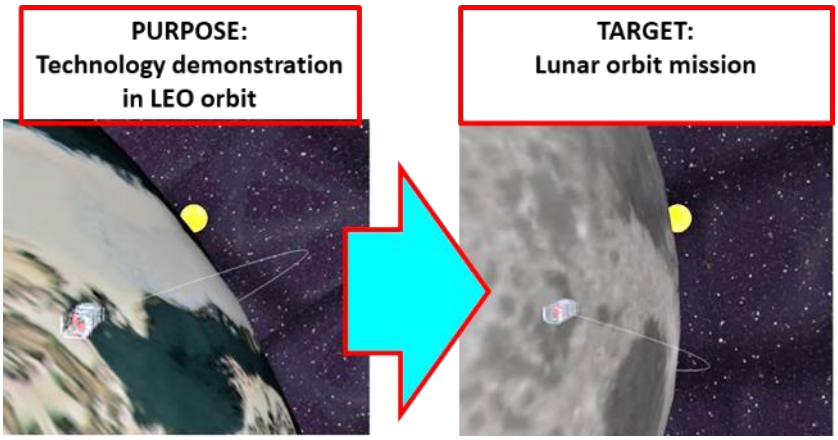

Figure 3.5 AV4 mission objectives

3.1.1 Hardware summary

According to mass/size restrictions, as well as power budget limitation, essential AOCS hardware is used to perform the maneuvers required to accomplish AV4 mission objectives. In Table 3.1, the AOCS hardware features are summarized.

Table 3.1 AOCS Hardware Features

Type	**Features**
Coarse sun sensors	Six SLCD-71N8 coarse sun sensors distributed along the satellite body. 60 half angle.
Fine sun sensors	Two GOM Space NanoSense FSS-4 fine sun sensors placed in +z and −z axis. 60 half angle.
Gyroscope	One three-axis gyroscope ICG20330 from Invent Sense, with a noise of 5 mdps/$\sqrt{\ }$Hz
Reaction Wheels	Three reaction wheels aligned with x, y and z axis, angular momentum 2[gm^2s^{-1}] at 4800 rpm, featuring a DC brushless motor Faulhaber 2610 006B with integrated speed controller
Pulsed Plasma Thrusters	Four heads placed in +z satellite face, operation frequency at 1 Hz, 25.20322 μNs as impulse bit and 60 as Δv

The OBC design is based on a DSP TMS320F28075 microcontroller. The OBC will gather all the AOCS software (c coding) as shown in figure 2. Information of the sensors will be saved into the OBC RAM and the interface between OBC and actuators will be placed in the same board. The AOCS software is designed in MATLAB environment

programming. For further validation and verification tasks, a processor-in the- loop and hardware-in-the-loop schemes will be implemented.

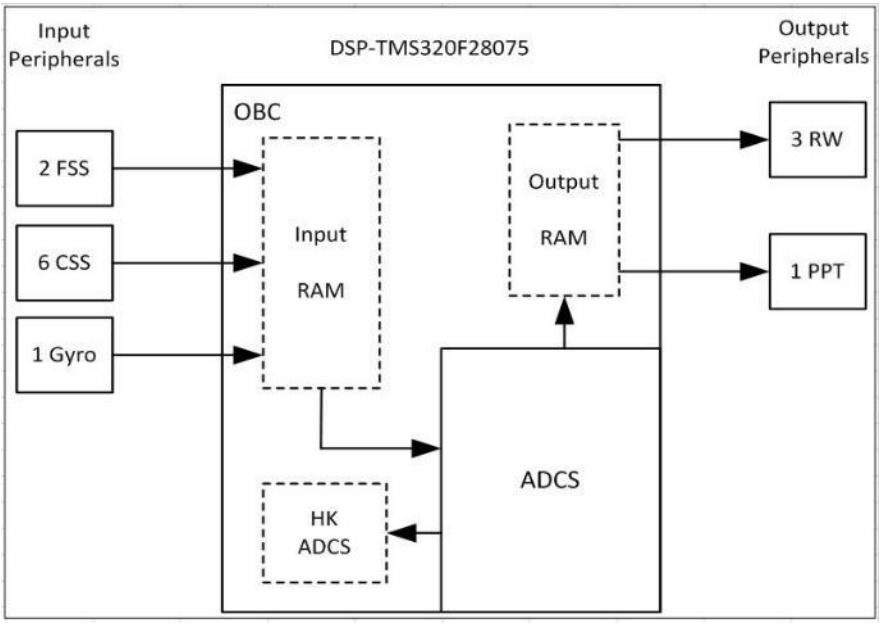

Figure 3.6 AOCS hardware implementation

3.1.2 Concept of operation

After its deployment and subsystems initialization, the AOCS starts its normal operations. In Figure 3.7, the proposed AOCS concept of operation of AV4 is shown, which includes the conditions that must be met in order to change between modes of operation. After the deployment of AV4 from its launcher, the detumble mode is set as default for the reduction of its initial angular rate. Once reaching the minimum threshold value of angular rate, the satellite will align its solar paddles towards the Sun, which is the nominal mode of operation. In science mode, the satellite can change between modes of operation to perform either sun point mode, horizon observation or orbit maintenance maneuvers (Figure 3.8) via ground station commands. In Table 3.2, details of the AOCS mode of operations are mentioned:

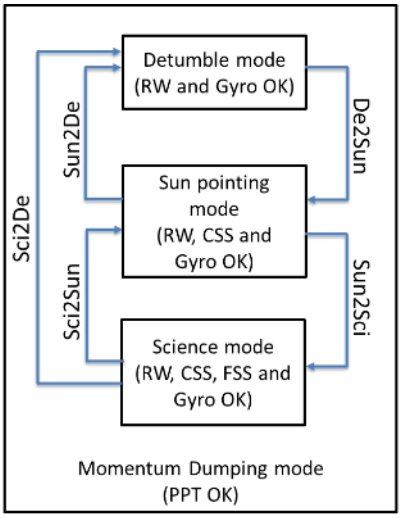

Mode Change	Condition
De2Sun*	• Normal / Safehold mode, Angular rate < w1, GS Uplink Command
Sun2Sci	• Normal mode, GS Uplink Command
Sci2Sun	• GS Uplink Command • Safehold mode
Sun2De	• Angular rate > w1
Sci2De	• Angular rate > w1
Momentum Dumping mode	• RW speed > w_rw

Figure 3.7 AOCS concept of operation

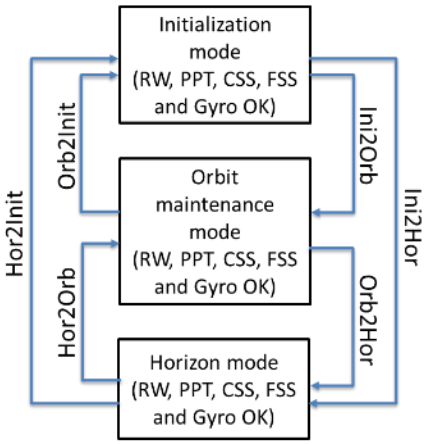

Mode Change	Condition
Ini2Orb	• GS Uplink Command
Ini2Hor	• GS Uplink Command
Orb2Hor	• GS Uplink Command
Orb2Init	• GS Uplink Command • TLE and Time data needs update
Hor2Orb	• GS Uplink Command
Hor2Init	• GS Uplink Command • TLE and Time data needs update

Figure 3.8 AOCS science mode concept of operation

Table 3.2 AOCS modes of operation according to AV4 concept of operation

Mode of operation	**Features**	**Hardware required**
Detumble mode	Reduction of angular rate via reaction wheels.	RWs, gyroscope
Sun-pointing mode	Alignment with a specified satellite body axis and Sun direction is performed. During eclipse, the satellite attitude is not controlled.	Coarse sun sensors, RWs, gyroscope

Initialization mode	Initialization of EKF. Solar paddles aim towards Sun	Coarse and fine sun sensors, gyroscope, RWs
Science mode	Satellite controls its attitude to the target. Orbit maintenance and horizon observation can be performed. If horizon detection task is performed through sun-tracking control, solar paddles will be aligned towards Sun automatically to prevent that camera will be exposed to the Sun light for a long period.	Coarse and fine sun sensors, gyroscope, RWs and PPT
Momentum dumping mode	PPTs provide a torque in such a way that RW speed is reduced without interfering with the current attitude control task, leading to their desaturation until a low-limit speed is reached.	Gyroscope, RWs and PPT

3.2 The AOCS software scheme

Based on the AV4 AOCS hardware and modes of operation, the AOCS software is designed to meet the requirements stablished in its mission success criteria. Thus, the following modules of the AOCS software were proposed (Figure 3.9):

- Fault detection: Provide autonomy to AV4 during critical circumstances by choosing the modes of operation. The unexpected increase of angular velocity, ground station commands reception and on-board computer (OBC) commands are consider.
- Navigation system: It propagates the satellite orbital ephemeris until new TLE information is received. Also, it calculates the reference coordinate systems for each mode of operation, as well as the sun and moon reference position.
- Attitude determination and control: It determines and propagate the 2-axis attitude of the satellite depending on the sun sensor data availability. It also calculates the control torque for each mode of operation.
- Actuators command: By conditioning the calculated control torque from the attitude control module, this element set the commands to operate the AOCS actuators according to their configuration and features.

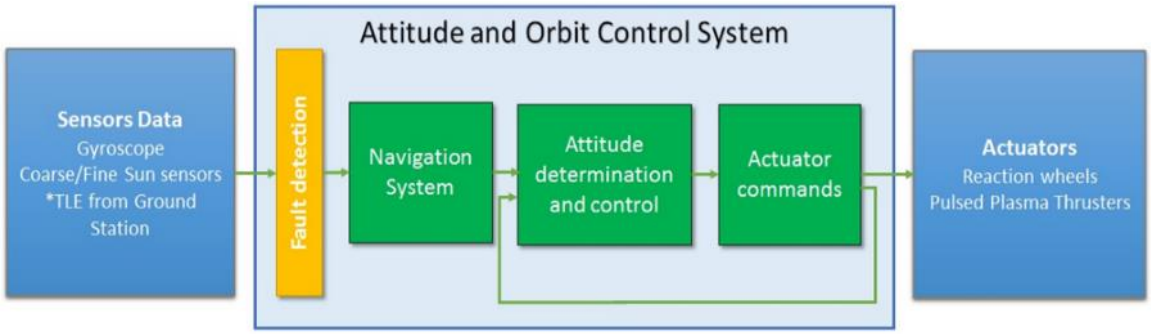

Figure 3.9 AV4 AOCS software scheme and its components

3.2.1 Fault detection

This element monitors the data obtained from AOCS sensors and OBC commands. Regarding the health of sensors data, this submodule detects abnormal data, isolate and decide the mode of operation according the Table 3.3. During normal operation, the next scenarios are considered for the software design of this subroutine:

- Monitoring the status of the satellite angular rate by reading the information of gyroscopes, as well as speed of reaction wheels for the initialization of desaturation control via PPT.
- Receiving new TLE information for the initialization of the orbit propagator and the extended Kalman filter.
- Receiving OBC commands such as hardware failure and low-level battery.
- Changes among operation modes from ground station.
- Time calibration
- AOCS software reset

Depending on the mode of operation, this subroutine enables/disables the AOCS subroutines. For example, during detumble mode, the navigation and attitude determination system is disabled. During science mode, all subroutines are required.

Table 3.3 Fault chart

Sensors	***Index***	***Type of failure***	***Impact on mission***	***Countermeasure***

FSS or CSS or GYRO	1	Outlier failure	Very low	Use previous data
FSS -x or -z	2	Total failure	Low	Use CSS to obtain sun vector information
CSS -x or -z	3	Total failure	Low	Use FSS -x to obtain sun vector information
CSS ±y and/or +x and/or +z	4	Total failure	Medium	ADS disabled, use only attitude control maneuvers based on sun tracking
GYRO	5	Total failure	High	ADS disabled, use only attitude control maneuvers based on sun tracking, estimate angular rates along sun vector
GYRO and FSS	6	Total failure	High	ADS disabled, use only attitude control maneuvers based on sun tracking, estimate angular rates along sun vector
GYRO and CSS	7	Total failure	Very high	ADS disabled, use only attitude control maneuvers based on sun tracking, estimate angular rates along sun vector when possible
CSS and FSS	8	Total failure	Critical	ADS disabled, detumble mode available
GYRO, CSS and FSS	9	Total failure	Critical	ADS and ACS disabled

3.2.2 Navigation

This submodule is used to determine the position and velocity of the satellite, calculates the sun and moon position and determines the appropriate reference frames for a specific attitude pointing strategy (Figure 3.10). The orbit propagator consists on the software implementation of the special general perturbation (SGP4) as the default propagator. For experimental purposes, the restricted three body problem (Earth+J2 perturbation - Sun - Moon - satellite system) solved with fourth-order Runge-Kutta method was implemented too. Once the TLE information is received (from either NORAD or another ground station network), the initial position and velocity is computed and used as inputs for the orbit propagator. For attitude and orbit control tasks, an orbit reference is computed based on the actual orbital state. The reference acceleration vector is computed via the optimal in-plane orbit maneuvers strategy. The reference coordinate system calculator uses the satellite position and velocity information, as well as the

position of other celestial bodies. Orthogonal vectors are used to determine the appropriate transformation matrices for a specific attitude pointing strategy

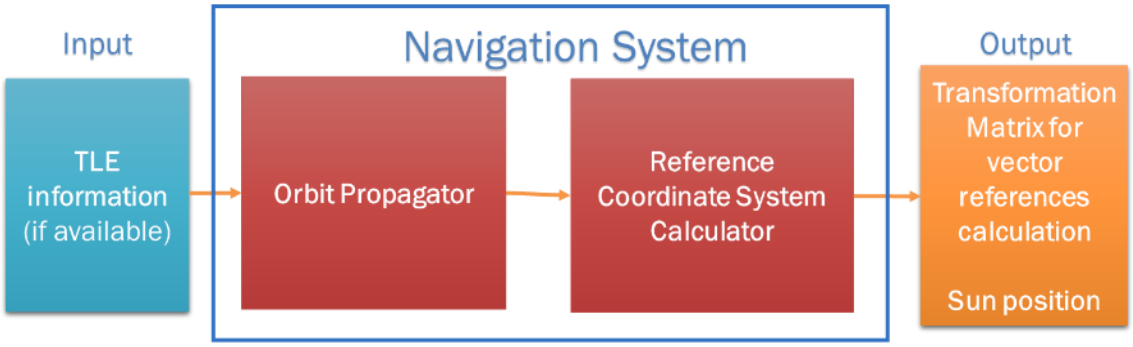

Figure 3.10 AV4 navigation submodule

3.2.3 Attitude determination and control system

This element determines and control the attitude of the satellite. Followed by a specific mode of operation, this element computes the required torques to change the attitude of the satellite (Figure 3.11). It also detects whether the reaction wheels reach a certain angular rate limit and sends the required commands to PPTs for their desaturation. During science mode, the Extended Kalman Filter (EKF) is used to estimate and propagate the attitude of the satellite. Because it is well known that at least two vector measurements are required to determine the satellite three-axis attitude information, the attitude determination strategy relies only on the sun vector information and the initial condition used for the attitude estimation and propagation, as well as a specific reference frame. Due to these limitation, we refer to this method as pseudo-three axis attitude determination.

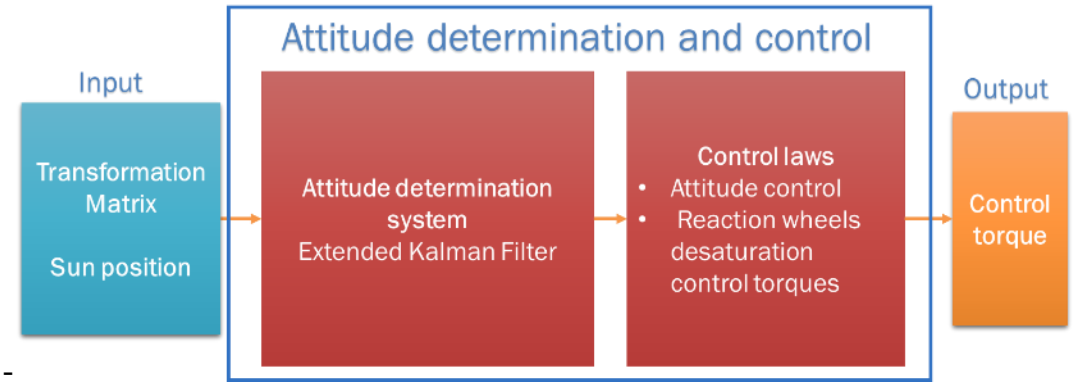

-

Figure 3.11 AV4 attitude determination and control submodule

3.2.4 Actuators command

Once the control torque commands are calculated, the actuator commands are computed in terms of reaction wheels speed and spin direction, as well as the ignition of a specific PPT head, according to the mode of operation (Figure 3.12). For example, during orbit maintenance mode, the PPT heads are ignited alternatively. During the desaturation of a reaction wheel, the corresponding PPT head produces ignition until the reaction wheels reaches a minimum threshold value.

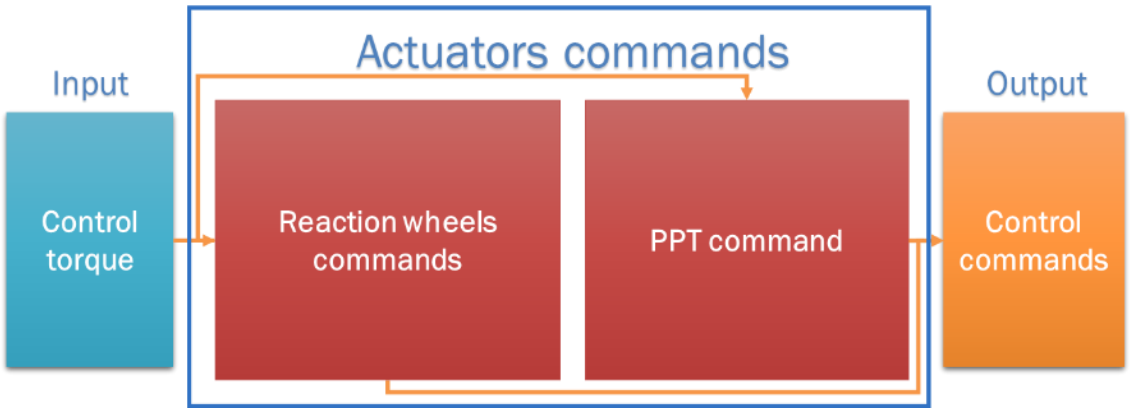

Figure 3.12 AV4 Actuators commands

CHAPTER 4. SATELLITE DYNAMICS

This chapter is dedicated to the description of the satellite orbit dynamics and attitude equations, which were considered through this research.

4.1 Time

A practical and precise time system must be agreed in order to describe the translational motion of the massive bodies and the spacecraft. In this research, several conventions were used according to the numerical method implemented for the calculation of a physical planetary parameter.

4.1.1 Solar time and Universal time

A solar day is an interval of successive transits of the Sun over a local meridian. In other words, from high noon to high noon it takes 24 hours or one revolution of the Earth (360°). This means that the time can be divided into hours, minutes and seconds, as well as into degrees, arcminutes and arcseconds. The Universal time (UT), which is referred to UT1 nowadays, is determined by the sun passing through the Greenwich meridian [27], [29]. The universal time coordinated (UTC) is the most commonly time system used. It is based on the international atomic time (TAI), which is the fundamental unit of time of the Systeme International (SI) system, defined as 9,192,631,770 cycles of the radiation corresponding to the ground state hyperfine transition of Cesium 133. Its epoch is adjusted by adding leap seconds to keep the UTC 0.9s of UT1 [13], [28].

The Julian day number is the result of combining the solar cycle (28 years), the Metonic cycle (19 years) and the Roman indication (15 years) in order to find a common starting point, which was determined by Joseph Scaliger in 1582 [27]. This starting point was determined to be on 1 January 4713 BC at 12:00pm. The Julian date at any UT of the day is calculated as $JD = J_0 + UT/24$, where J_0 is the Julian day number at 0h UT. The conversion from Gregorian year (y), month (m) and day (d) to Julian day is given by [29]:

$$J_0 = 367y - \text{INT}\left\{\frac{7\left[y + \text{INT}\left(\frac{m+9}{12}\right)\right]}{4}\right\} + \text{INT}\left(\frac{275m}{9}\right) + d + 1{,}721{,}013.5 \tag{4.1}$$

4.1.2 Sidereal time

The sidereal time is related with the Earth's rotation and measured from the vernal equinox relative to a local meridian (termed as local sidereal time θ_{LST}), in counter-clock wise direction as seen from the North pole. The Greenwich sidereal time θ_{GST} is measured from the vernal equinox as a reference point and Greenwich meridian, which means that a sidereal day takes 23h 56min of a solar day (Figure 4.1). The conversion between θ_{GST} and θ_{LST} for a specific west or east longitude λ (negative or positive value respectively) can be performed by using [28]:

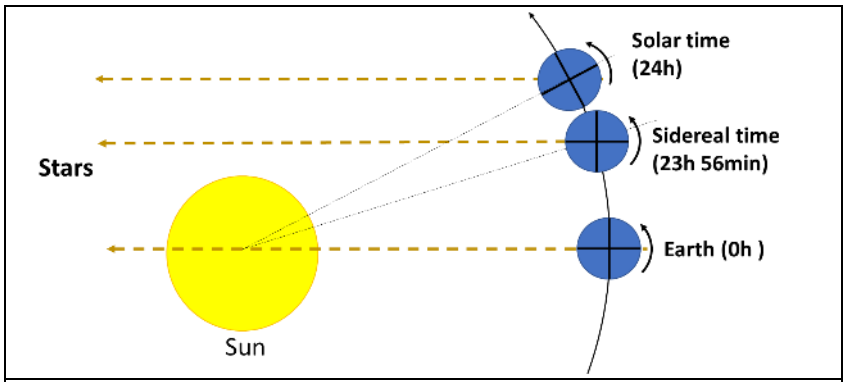

Figure 4.1 The sidereal and solar time

$$\theta_{LST} = \theta_{GST} + \lambda \tag{4.2}$$

If the universal time is known, it is possible to calculate the θ_{GST0} in radians (at 0hh 00mm 00ss UT1 of a desired date), considering the epoch J2000, by using the following equation:

$$\theta_{GST0} = 1.753368560 + 628.3319706889T_{UT1} + 6.7707 \times 10^{-6}T_{UT1}^2 - 4.5 \times 10^{-10}T_{UT1}^3 \tag{4.3}$$

where T_{UT1} is the number of Julian centuries elapsed from J2000 epoch, which is calculated by considering the Julian date at 0hh 00mm 00ss of the day (JD_0):

$$T_{UT1} = \frac{JD_0 - 2{,}451{,}545.0}{36{,}525} \tag{4.4}$$

The calculation of the Greenwich sidereal time at any time *UT1* of the day is performed by taking the rotational speed of the Earth $\omega_{\oplus}$, which is equal to 0.250 684 477 337 462 15 degrees/solar minutes (0.525032341581579 rad/s):

$$\theta_{GST} = \theta_{GST0} + \omega_{\oplus} UT1 \tag{4.5}$$

4.2 Coordinate Reference Frames

The description of an orbit requires the definition of a reference frame which possess an origin, fundamental plane, direction and sense [28]. It is common to define a coordinate axis by using the right-hand rule, unless the left-hand rule it is required for a specific purpose. In the following subsections, the coordinate reference frames utilized in this research are mentioned.

4.2.1 Earth-centered inertial reference frame

The well-known Earth centered inertial (ECI) reference frame, uses the J2000 as epoch time (2000 January 01, 12:00hrs UT). The $\boldsymbol{x}_i$ axis points towards the vernal equinox, $\boldsymbol{z}_i$ points towards the mean Earth's North pole and $\boldsymbol{y}_i$ axis completes the right-hand rule [14]. The ECI frame is used in this research to describe the spacecraft motion along its orbit and calculate the position of the Sun and Moon from the center of Earth.

4.2.2 Earth-centered Earth-fixed reference frame

The Earth-centered Earth-fixed (ECEF) reference frame rotates in z-axis with an angular velocity $\omega_{\oplus}$ (Earth rotation speed). Its $\boldsymbol{x}_e$ axis coincides with the intersection between equator and Greenwich meridian, $\boldsymbol{z}_e$ axis points towards the North pole and $\boldsymbol{y}_e$ completes the right-hand rule. In Figure 4.2, the ECI and ECEF reference frames are illustrated. Slight rotations in $\boldsymbol{x}_e$ and $\boldsymbol{y}_e$ axis exist along the Earth rotation due to the

gravitational influence of the Sun and Moon, called precession and nutation respectively [28].

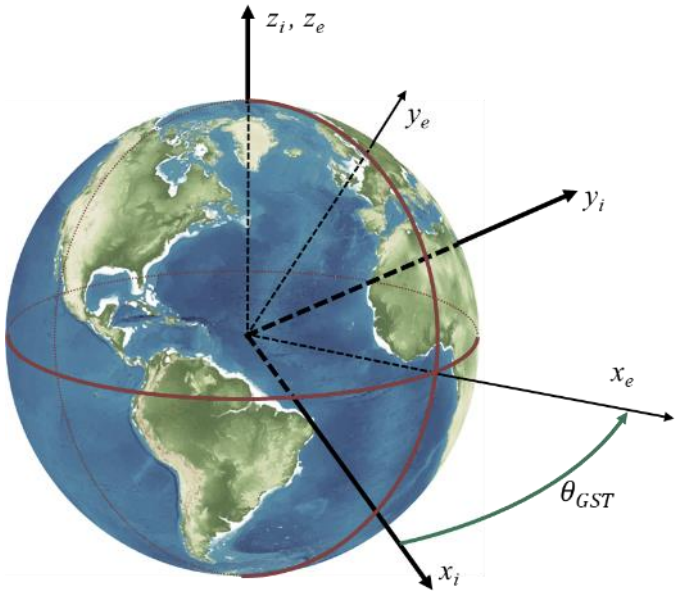

Figure 4.2 ECI and ECEF reference frames

4.2.3 Spacecraft body-centered reference frame

Pointing maneuvers can be performed based on a customized $\boldsymbol{x}_o$, $\boldsymbol{y}_o$ and $\boldsymbol{z}_o$ reference frame. Its origin is the satellite center of mass. Depending on the operation mode, the spacecraft body-centered SBC reference frame is established based on unit vectors that can be defined in a common reference frame [27].

Velocity vector alignment: $\boldsymbol{z}_o$ axis is aligned with the velocity vector $\boldsymbol{v}$, $\boldsymbol{x}_o$ axis is perpendicular to $\boldsymbol{z}_o$ axis and the normal of plane orbit $\boldsymbol{\eta}$, $\boldsymbol{y}_o$ completes the right-hand rule.

$$\begin{gathered} \boldsymbol{z}_o = \boldsymbol{v} \\ \boldsymbol{x}_o = \boldsymbol{\eta} \times \boldsymbol{z}_o = (\boldsymbol{r} \times \boldsymbol{v}) \times \boldsymbol{z}_o \\ \boldsymbol{y}_o = \boldsymbol{z}_o \times \boldsymbol{x}_o \end{gathered} \tag{4.6}$$

Orbit maintenance vector alignment: $\boldsymbol{z}_o$ axis is aligned with the calculated thrust vector $\boldsymbol{f}$ to perform an optimal orbit correction maneuver, $\boldsymbol{x}_o$ axis is perpendicular to $\boldsymbol{z}_o$ axis and the normal vector of the thrust-sun plane, $\boldsymbol{y}_o$ completes the right-hand rule.

$$\begin{gathered} \boldsymbol{z}_o = \boldsymbol{f} \\ \boldsymbol{x}_o = \boldsymbol{z}_o \times \boldsymbol{\eta} = \boldsymbol{z}_o \times (\boldsymbol{f} \times \boldsymbol{s}) \\ \boldsymbol{y}_o = \boldsymbol{z}_o \times \boldsymbol{x}_o \end{gathered} \tag{4.7}$$

Horizon observation: $\boldsymbol{z}_o$ axis is aligned with the location of the Earth horizon $\boldsymbol{\xi}$, $\boldsymbol{x}_o$ axis is perpendicular to $\boldsymbol{z}_o$ axis and the normal vector of the Earth-Sun-satellite plane defined by the satellite position $\boldsymbol{r}$ and sun direction $\boldsymbol{s}$ (this is required to observe the orbit sunrise and sunset), $\boldsymbol{y}_o$ completes the right-hand rule.

$$\begin{gathered} \boldsymbol{z}_o = \boldsymbol{\xi} \\ \boldsymbol{x}_o = \boldsymbol{\eta} \times \boldsymbol{z}_o = (\boldsymbol{r} \times \boldsymbol{s}) \times \boldsymbol{z}_o \\ \boldsymbol{y}_o = \boldsymbol{z}_o \times \boldsymbol{x}_o \end{gathered} \tag{4.8}$$

Once obtaining the unit vectors $\boldsymbol{x}_o$, $\boldsymbol{y}_o$ and $\boldsymbol{z}_o$, a transformation matrix that relates the target reference frame *O* and the initial reference frame *I*:

$$T_I^O = [\boldsymbol{x}_o \quad \boldsymbol{y}_o \quad \boldsymbol{z}_o] \tag{4.9}$$

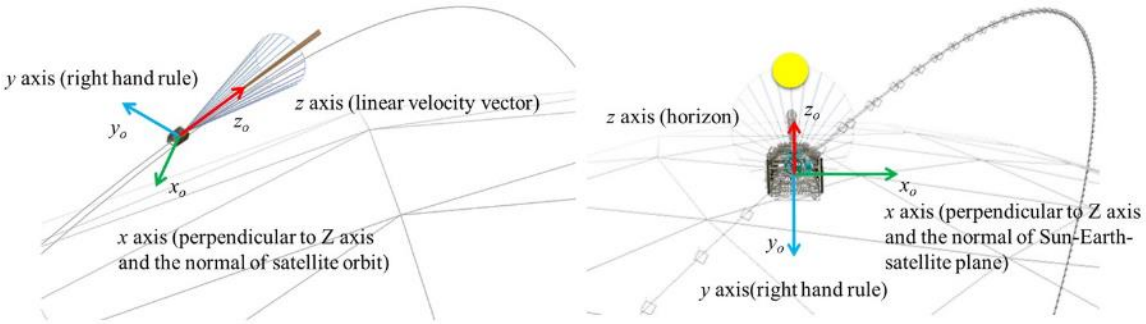

Figure 4.3 Left: Velocity reference frame. Right: Horizon reference frame

4.2.4 Spacecraft body-centered body-fixed reference frame

The origin of the spacecraft body centered body fixed SBCBF reference frame is the satellite center of mass. The direction of $\boldsymbol{x}_b$, $\boldsymbol{y}_b$ and $\boldsymbol{z}_b$ axis is defined by developers considering the spacecraft geometry.

4.3 Attitude Representation

There are several ways to represent the attitude of a body related with a specific reference frame. Unit quaternions and transformation matrices as attitude representation are considered in this research.

4.3.1 Unit quaternions

The attitude of a body can be represented as a rotation angle β along a certain unit vector $\boldsymbol{\lambda}$ expressed in a certain reference frame. Therefore, it is necessary to use four elements to express the attitude, as well as a quaternion. Quaternions are widely used because of the avoidance of trigonometric operations, which represents an advantage for computation routines. Another advantage is the prevention of singularities presented in progressive rotations using Euler angles. A quaternion can be defined as a four-dimensional vector which contains a scalar q_4 and a vector $\boldsymbol{q}$, in such a way that:

$$\begin{gathered}\mathbf{q} = [\boldsymbol{q} \quad q_4] = [q_1 \quad q_2 \quad q_3 \quad q_4] \\ q_1^2 + q_2^2 + q_3^2 + q_4^2 = \mathbf{q}^\top \mathbf{q} = 1\end{gathered} \tag{4.10}$$

where:

$$\begin{aligned}q_4 &= \cos\frac{\beta}{2} \\ \boldsymbol{q} &= \boldsymbol{\lambda}\sin\frac{\beta}{2}\end{aligned} \tag{4.11}$$

The product between two quaternions $\mathbf{q}_a$ and $\mathbf{q}_b$ is non-commutative and it is defined by the following equation:

$$\mathbf{q}_a \otimes \mathbf{q}_b = \begin{bmatrix} q_4 & -q_3 & q_2 & q_1 \\ q_3 & q_4 & -q_1 & q_2 \\ -q_2 & q_1 & q_4 & q_3 \\ -q_1 & -q_2 & -q_3 & q_4 \end{bmatrix}_a \begin{bmatrix} q_1 \\ q_2 \\ q_3 \\ q_4 \end{bmatrix}_b \tag{4.12}$$

which can also be expressed as:

$$\mathbf{q}_a \otimes \mathbf{q}_b = \begin{bmatrix} q_{a,4}\boldsymbol{q}_b + q_{b,4}\boldsymbol{q}_a + \boldsymbol{q}_a \times \boldsymbol{q}_b \\ q_{a,4}q_{b,4} - \boldsymbol{q}_a^{\top}\boldsymbol{q}_b \end{bmatrix} \tag{4.13}$$

4.3.2 Transformation matrix

The use of transformation matrices in space engineering is widely used. Ground station tracking, orbital mechanics and attitude and orbit control are some of the most common applications. In principle, a transformation matrix can be interpreted as:

- A way to represent a vector in two reference frames.
- A rotation of a vector in a reference frame.
- A relationship between two reference frames.

The rotation matrix *R* which describes the relationship between the reference frame *a* and a reference frame *b* is written as R_a^b (Transformation from the reference frame a to b). The matrix *R* has the following properties: $R^{\top}R = I^{3\times3}$, $\det(R) = 1$ and $R_a^b = (R_a^b)^{-1} = (R_a^b)^{\top}$. The transformation of a vector *v* from a reference frame *a* to another *b* is expressed as $\boldsymbol{v}_b = R_a^b \boldsymbol{v}_a$.

In terms of a rotation angle β along a vector $\boldsymbol{\lambda}$, a transformation matrix *R* is calculated as follows:

$$R_a^b(\beta, \boldsymbol{\lambda}) = I + S(\boldsymbol{\lambda}) \sin\beta + (1 - \cos\beta) S^2(\boldsymbol{\lambda}) \tag{4.14}$$

By using quaternions, equation (4.14) yields:

$$R_a^b(\mathbf{q}) = I + 2q_4 S(\boldsymbol{q}) + 2S^2(\boldsymbol{q}) \tag{4.15}$$

where $S(\cdot)$ is a skew matrix which is used as a cross product operator between two vectors $\boldsymbol{x}$ and $\boldsymbol{y}$:

$$\boldsymbol{x} \times \boldsymbol{y} = S(\boldsymbol{x})\boldsymbol{y} = \begin{bmatrix} 0 & -x_3 & x_2 \\ x_3 & 0 & -x_1 \\ -x_2 & x_1 & 0 \end{bmatrix} \begin{bmatrix} y_1 \\ y_2 \\ y_3 \end{bmatrix} \tag{4.16}$$

The most common way to perform sequences of reference frame transformations is by using rotation angles (e.g. θ, ϕ and ψ) along the $\boldsymbol{x}$, $\boldsymbol{y}$ and $\boldsymbol{z}$ axis of a specific reference frame as follows:

$$\begin{aligned} R_x(\theta) &= \begin{bmatrix} 1 & 0 & 0 \\ 0 & \cos\theta & -\sin\theta \\ 0 & \sin\theta & \cos\theta \end{bmatrix} \\ R_y(\phi) &= \begin{bmatrix} \cos\phi & 0 & \sin\phi \\ 0 & 1 & 0 \\ -\sin\phi & 0 & \cos\phi \end{bmatrix} \\ R_z(\psi) &= \begin{bmatrix} \cos\psi & -\sin\psi & 0 \\ \sin\psi & \cos\psi & 0 \\ 0 & 0 & 1 \end{bmatrix} \end{aligned} \tag{4.17}$$

The time derivative of a transformation matrix is calculated as follows:

$$\dot{R}_a^b = -\mathrm{S}(\boldsymbol{\omega}_a^b) R_a^b \tag{4.18}$$

where $\boldsymbol{\omega}_a^b$ is the angular velocity of the frame *a* relative to the reference frame *b*. It can be noticed that $\boldsymbol{\omega}_a^b = -\boldsymbol{\omega}_b^a$.

4.4 Orbit Mechanics

The satellite orbit dynamics in ECI reference frame can be described with the differential equation commonly known as the restricted three body problem (Figure 4.4) with orbital distributions, which is shown in the next equation [28]:

$$\ddot{\boldsymbol{r}}_{E,sc} = \boldsymbol{a}_M + \boldsymbol{a}_E + \boldsymbol{a}_S + \boldsymbol{a}_{sp} + \boldsymbol{a}_{ad} + \boldsymbol{a}_F \tag{4.19}$$

where $\boldsymbol{a}_M$, $\boldsymbol{a}_E$, $\boldsymbol{a}_S$, $\boldsymbol{a}_{sp}$, $\boldsymbol{a}_{ad}$ and $\boldsymbol{a}_F$ are the spacecraft acceleration terms due to the gravitational influence of the Moon, Earth, and Sun, as well as the radiation pressure term,

atmospheric drag term and thrust force respectively. $\boldsymbol{r}_{E,sc}$ is the spacecraft position relative to the Earth's center in ECI frame and:

$$\begin{aligned} \boldsymbol{a}_E &= \boldsymbol{a}_{\nabla \boldsymbol{U}_{E,sc}} \\ \boldsymbol{a}_M &= -\mu_M \left(\frac{\boldsymbol{r}_{M,sc}}{r_{M,sc}^3} - \frac{\boldsymbol{r}_{M,E}}{r_{M,E}^3} \right) \\ \boldsymbol{a}_S &= -\mu_S \left(\frac{\boldsymbol{r}_{S,sc}}{r_{S,sc}^3} - \frac{\boldsymbol{r}_{S,E}}{r_{S,E}^3} \right) \\ \boldsymbol{a}_{sp} &= -\frac{p_{sr} c_r A_S}{m_{sc}} \frac{\boldsymbol{r}_{sc,S}}{r_{sc,S}} \\ \boldsymbol{a}_{ad} &= -\frac{1}{2} \frac{c_D A_d \rho}{m_{sc}} \frac{\dot{\boldsymbol{r}}_{E,sc}}{\dot{r}_{E,sc}} \end{aligned} \tag{4.20}$$

where μ_M and μ_S are the standard gravitational parameters of the Earth and Sun, respectively. The term $\boldsymbol{a}_{\nabla \boldsymbol{U}_{M,sc}}$ is obtained by considering the Earth gravity model EGM2008, which depends on the position of the spacecraft, $\boldsymbol{r}_{E,sc}$, in ECEF frame, where a transformation of reference frames between ECI and ECEF is required. The Sun and Moon position values were obtained by numerical methods based on series expansion [28] [30]. The calculation of the solar radiation pressure term depends on the solar radiation pressure, p_{sr}, the body reflectivity, c_r, the exposed area to the Sun, A_S, the spacecraft mass, m_{sc}, and the spacecraft-Sun vector, $\boldsymbol{r}_{sc,S}$. Details of the atmospheric drag term are mentioned in section 4.7.2. To determine the Sun-eclipse phases in Moon orbit, we assumed the geometry of the umbra as a simple cylindrical shape [28].

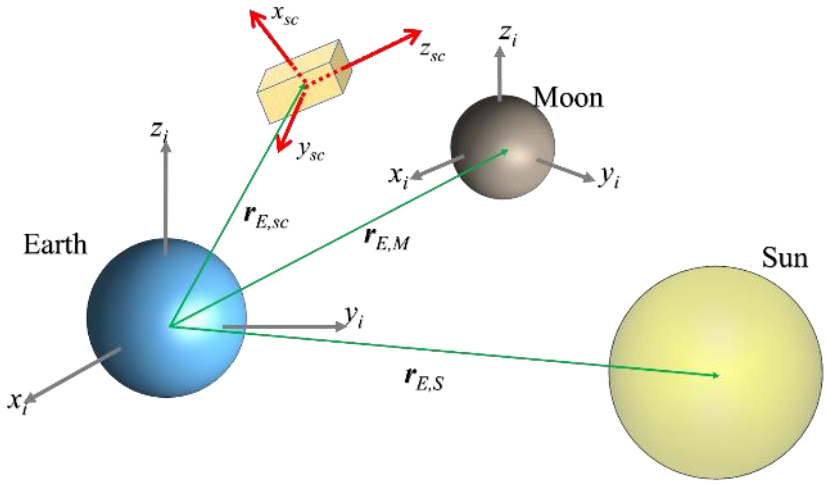

Figure 4.4 Restricted three body problem for spacecrafts orbiting the Earth

For satellites orbiting the Moon, the terms of equation (4.19) and (4.20) related with satellite position are updated as follows:

$$\ddot{\boldsymbol{r}}_{M,sc} = \boldsymbol{a}_M + \boldsymbol{a}_E + \boldsymbol{a}_S + \boldsymbol{a}_{sp} + \boldsymbol{a}_F \tag{4.21}$$

where:

$$\begin{aligned} \boldsymbol{a}_M &= \boldsymbol{a}_{\nabla U_{M,sc}} \\ \boldsymbol{a}_E &= \boldsymbol{a}_{\nabla U_{E,sc}} - \mu_E \left(\frac{\boldsymbol{r}_{E,sc}}{r_{E,sc}^3} - \frac{\boldsymbol{r}_{E,M}}{r_{E,M}^3} \right) \\ \boldsymbol{a}_S &= -\mu_S \left(\frac{\boldsymbol{r}_{S,sc}}{r_{S,sc}^3} - \frac{\boldsymbol{r}_{S,M}}{r_{S,M}^3} \right) \\ \boldsymbol{a}_{sp} &= -\frac{p_{sr} c_r A_S}{m_{sc}} \frac{\boldsymbol{r}_{sc,S}}{r_{sc,S}} \end{aligned} \tag{4.22}$$

The term $\boldsymbol{a}_{\nabla U_{M,sc}}$ is obtained by considering the LP165p lunar gravity model with degree and order 100, which gives a reliable approximation for the calculation of the smallest mascon and depends on the position of the spacecraft, $\boldsymbol{r}_{M,sc}$, in a Moon-Centered-Moon-Fixed (MCMF) coordinate system, whose transformation matrix to Inertial Celestial Reference Frame (ICRF) is given in the IAU/IAG 2000 Report [31]. The orbital disturbance due to the Earth gravity potential, $\boldsymbol{a}_{\nabla U_{E,sc}}$ is added to this equation since Earth gravity field has a strong influence on spacecraft's lunar orbit [32]. In this research, the Earth gravity model EGM2008 at the 5th degree is considered.

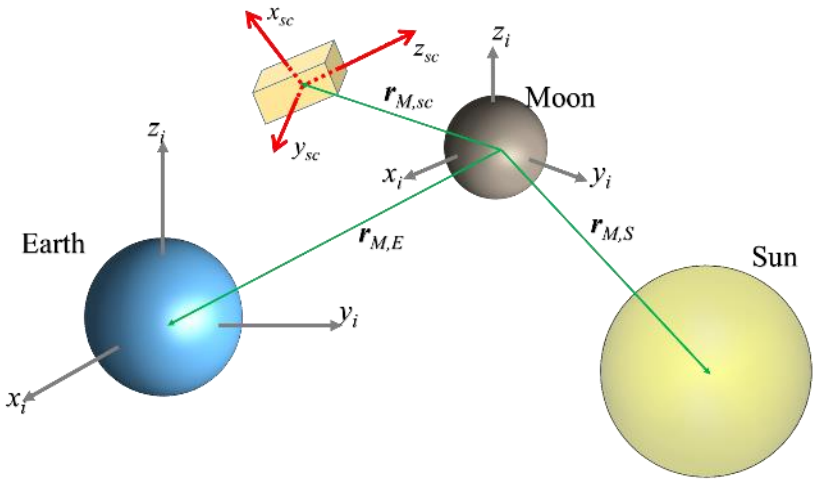

Figure 4.5 Restricted three body problem for spacecrafts orbiting the Moon

4.5 Rigid Body Mechanics

In Figure 4.6, the body fixed reference frame is shown. For example, satellites, aircraft, or robots are often modeled as rigid bodies (no body deformations are allowed) since their rotational dynamics are often expressed as Eulerian mechanics. The Euler's equation $\dot{\boldsymbol{H}} = \boldsymbol{L}$ and Euler's rotational equation of motion generally govern this field [32].

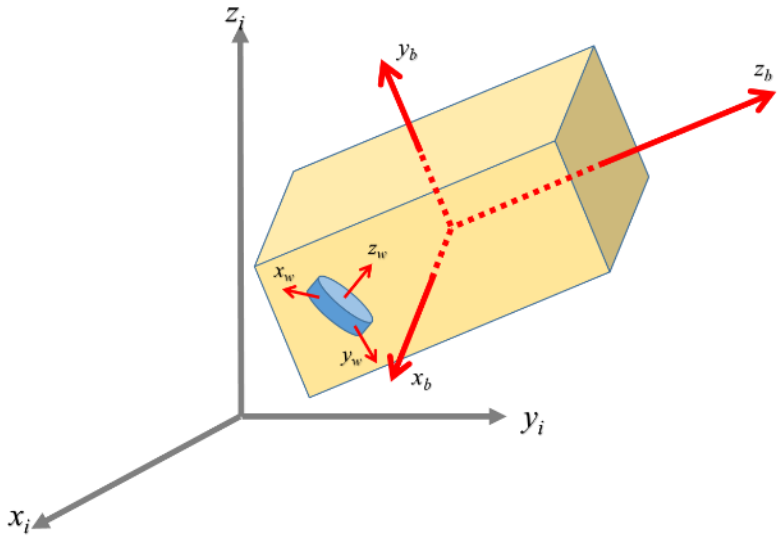

Figure 4.6 Spacecraft and reaction wheels reference frame

To describe the attitude dynamics of the satellite in SBCBF frame relative to an inertial reference frame (in this case, the ECI frame), the following rigid body differential equation is used:

$$\dot{\boldsymbol{H}} = -\boldsymbol{\omega}_b^i \times (\boldsymbol{H}) + \boldsymbol{\tau}_s \tag{4.23}$$

where $\boldsymbol{\omega}_b^i$ is the angular rate of the spacecraft's body *b* relative to the inertial frame *i* and $\boldsymbol{\tau}_s$ is the sum of the external torques due to the space environment disturbances. The angular momentum $\boldsymbol{H}$ is defined in this work as:

$$\boldsymbol{H} = J\boldsymbol{\omega}_b^i + AJ_w\boldsymbol{\omega}_w^b \tag{4.24}$$

Where J and J_w is the spacecraft and reaction wheel inertial matrices respectively, $\boldsymbol{\omega}_w^b$ is the reaction wheels *w* speed relative to body frame *b* and A contains the information related with the spin direction of each reaction wheel.

4.6 Attitude Kinematics

Considering the attitude representation in terms of quaternions, it is possible to obtain the differential equation of the satellite attitude kinematics. The time derivative of equation (4.11) is [34]:

$$\frac{d\mathbf{q}_b^i}{dt} = \begin{bmatrix} -\dfrac{d\beta}{dt}\sin\beta \\ \dfrac{d\boldsymbol{\lambda}}{dt}\sin\beta + \boldsymbol{\lambda}\dfrac{d\beta}{dt}\cos\beta \end{bmatrix} \tag{4.25}$$

It can be observed that $d\beta/dt = \left\|\boldsymbol{\omega}_b^i\right\|$, $\boldsymbol{\lambda}\cdot d\beta/dt = \boldsymbol{\omega}_b^i$, $d\boldsymbol{\lambda}/dt = -\boldsymbol{\omega}_b^i \times \boldsymbol{\lambda}$ and $\left\|\boldsymbol{q}_b^i\right\| = \|\boldsymbol{\lambda}\|\sin\beta$. Therefore, equation (4.25) is simplified as:

$$\frac{d\mathbf{q}_b^i}{dt} = \begin{bmatrix} q_{b,4}^i \cdot \boldsymbol{\omega}_b^i - \boldsymbol{\omega}_b^i \times \boldsymbol{q}_b^i \\ -\boldsymbol{q}_b^{i\,\top}\boldsymbol{\omega}_b^i \end{bmatrix} \tag{4.26}$$

Equation (4.26) can also be expressed as follows:

$$\frac{d\mathbf{q}_b^i}{dt} = \dot{\mathbf{q}}_b^i = \begin{bmatrix} q_{b,4}^i & -q_{b,3}^i & q_{b,2}^i & q_{b,1}^i \\ q_{b,3}^i & q_{b,4}^i & -q_{b,1}^i & q_{b,2}^i \\ -q_{b,2}^i & q_{b,1}^i & q_{b,4}^i & q_{b,3}^i \\ -q_{b,1}^i & -q_{b,2}^i & -q_{b,3}^i & q_{b,4}^i \end{bmatrix} \begin{bmatrix} \omega_{b,1}^i \\ \omega_{b,2}^i \\ \omega_{b,3}^i \\ 0 \end{bmatrix} \tag{4.27}$$

4.7 Space Environment Disturbance Torques

The rigid body dynamics of a spacecraft in orbit cannot be analyzed without considering the main disturbance torques. Therefore, the sizing of sensors and actuators, as well as the development attitude control laws must be done by considering the main disturbance torques that may reduce the maneuverability and operation capacity of the spacecraft's AOCS. In Table 4.1, the major external torques are listed [14].

Table 4.1 External disturbances

Type	**Source**	**Features**
Aerodynamic	Planetary atmosphere.	Drag and lift on the spacecraft. A strong function of altitude and position relative to the sun.
Albedo Pressure	Sun reflection from the earth.	Average is 0.34 of the solar flux for the earth. Varies depending on the latitude and longitude of the spacecraft, season and specific surface properties of the planet over which the spacecraft is flying.
Gravity gradient	Inertia and distance from the planet.	Due to the distributed nature of a satellite. If the satellite has off-diagonal inertia terms it will produce a body fixed torque for a planet pointing spacecraft. The diagonal terms can cause a gravity-gradient modal frequency.
Leaks	Onboard gas and liquid supplies.	Acts like a cold gas thruster.
Outgassing	Moisture embedded in the structure	Caused by the heating of surfaces and resulting emission of gas. This often happens with composite solar arrays and can produce large forces.
Thruster Plumes	Interaction of rocket exhaust plumes and the structure.	Thruster plumes are mathematically the same as aerodynamics forces and torques. They are modeled in two broad regimes, near-field and far-field. Far field is when a thruster plume impinges on a surface far enough away from the thruster so that the flow is not a continuum. In near-field the flow is denser and fluid dynamic models may be appropriate.

Radiation Pressure	Temperature of the planet.	Black body radiation of the planet. 400 W for the earth.
Residual Dipole	Residual dipole on the spacecraft.	This torque is caused by the interaction of an external magnetic field and internal dipoles due to current loops, etc.

In this research, the aerodynamic, gravity gradient and solar radiation pressure external disturbances are considered.

4.7.1 Gravity gradient torques

This external disturbance torque is produced due to the misalignment between the satellite minor axis of inertia and the nadir vector, which means that the larger is the misalignment between those vectors, the disturbance torque will increase. The following expression can be used to calculate the gravity gradient torque [35]:

$$\boldsymbol{\tau}_g = 3\mu_E \left\| \boldsymbol{r}_{E,sc} \right\|^{-3} (\boldsymbol{n}_b \times J\boldsymbol{n}_b) \tag{4.28}$$

where $\boldsymbol{n}_b = R_i^b(\mathbf{q})\boldsymbol{n}_i$, $\boldsymbol{n}_i = -\boldsymbol{r}_{E,sc}$.It can be noticed from equation (4.19) and (4.20) that the most significant orbital force is produced by the gravity influence on the Earth. If the spacecraft is orbiting the Earth at high altitudes beyond LEO, the external torque due to the gravity gradient becomes smaller.

4.7.2 Aerodynamic torque

Particularly at low altitudes, this external torque can be the major disturbance torques for all spacecrafts orbiting the Earth and also decays exponentially at larger altitudes. A misalignment between the spacecraft's center of pressure along the orbital velocity vector and the center of mass, which is determined by the exposed area *A* to the incoming particles from the atmosphere, causes that disturbance torque, which is calculated as follows [35]:

$$\boldsymbol{\tau}_d = -\frac{1}{2} \mathrm{c}_D \rho A \|\boldsymbol{v}_b\|^2 \boldsymbol{v}_b \times \left(\boldsymbol{r}_{cp} - \boldsymbol{r}_{cm}\right) \tag{4.29}$$

where c_D is the drag coefficient (usually close to 2.0), $\boldsymbol{v}_b = R_i^b(\mathbf{q})\boldsymbol{v}_i$, $\boldsymbol{v}_i = \dot{\boldsymbol{r}}_{E,sc}$, $\boldsymbol{r}_{cp}$ and $\boldsymbol{r}_{cm}$ are the spacecraft's center of pressure and center of mass respectively and ρ the

atmospheric density in kg/m^3 whose value can be calculated, for example, by considering the exponential model [28]:

$$\rho = \rho_o \exp\left[-\frac{h_{ellp} - h_o}{H}\right] \tag{4.30}$$

where ρ_o is reference density, h_o the base altitude, h_{ellp} the current altitude and the scale height *H*. The reference values can be selected according to the following table [28]:

Table 4.2 Exponential atmospheric model

Altitude h_{ellp} (km)	**Base altitude** h_o (km)	**Nominal density** ρ_o (km/m^3)	**Scale height** H (km)
300-350	300	2.418×10^{-11}	53.628
350-400	350	9.158×10^{-12}	53.298
400-450	400	3.725×10^{-12}	58.515
450-500	450	1.585×10^{-12}	60.828
500-600	500	6.967×10^{-13}	63.822
600-700	600	1.454×10^{-13}	71.835
700-800	700	3.614×10^{-14}	88.667
800-900	800	1.170×10^{-14}	124.64
900-1000	900	5.245×10^{-15}	181.05
1000-	1000	3.019×10^{-15}	268.0

If we consider the surface of each face of the spacecraft's body, particularly for those which possess deployable solar paddles, equation (4.29) becomes [36]:

$$\boldsymbol{\tau}_d = -\sum_{i=1}^{n} F_i \times \left(\boldsymbol{r}_{cp,i} - \boldsymbol{r}_{cm}\right) \tag{4.31}$$

where *i* subscript indicates the *i*-th surface considered for the calculation of the aerodynamic torque in body frame. The drag force F_i is calculated as follows:

$$F_i = \frac{1}{2} c_D \rho (A_i \|\boldsymbol{v}_b\|^2 \boldsymbol{v}_b) \tag{4.32}$$

where A_i can be found by calculating the dot product between the velocity vector $\boldsymbol{v}_b$ and the normal vector of the i-th surface A_i.

CHAPTER 5. AOCS ALGORITHM

In this chapter, details of the AOCS algorithms for AV4 project will be provided. Based on the mission objectives and hardware constrains, several algorithms were considered for attitude determination and control tasks that results into effective attitude maneuvers; however, due to the lack of an on-board GPS, an orbit propagator must be considered and uses most of the computational resources of the OBC. Moreover, an attitude determination system based on Kalman filter was implemented due to the attitude control requirements of AV4. Nonetheless, back-up algorithms were considered in case that the primary scheme based on Kalman filtering become unstable.

Additionally, since AV4 is a technology demonstration CubeSat mission towards a future lunar mission, the general structure of the developed AOCS software can be considered for its utilization of the lunar mission for the observation of the LHG. For example, the horizon detection and orbit maintenance strategy implemented in this AOCS can be utilized directly in that future lunar mission.

This chapter summarizes the algorithms implemented for the AOCS and their implementation in a structured way. Additionally, its inputs and outputs will be explained.

5.1 System overview

The general structure of the AV4 AOCS was explained in section 3.2. In this chapter, the inputs, AOCS subroutines and outputs will be described in a structured way (Figure 5.1), where the following items are identified:

- Inputs
- Fault detection
- Navigation
- Attitude determination
- Attitude control
- Hardware commands
- Outputs

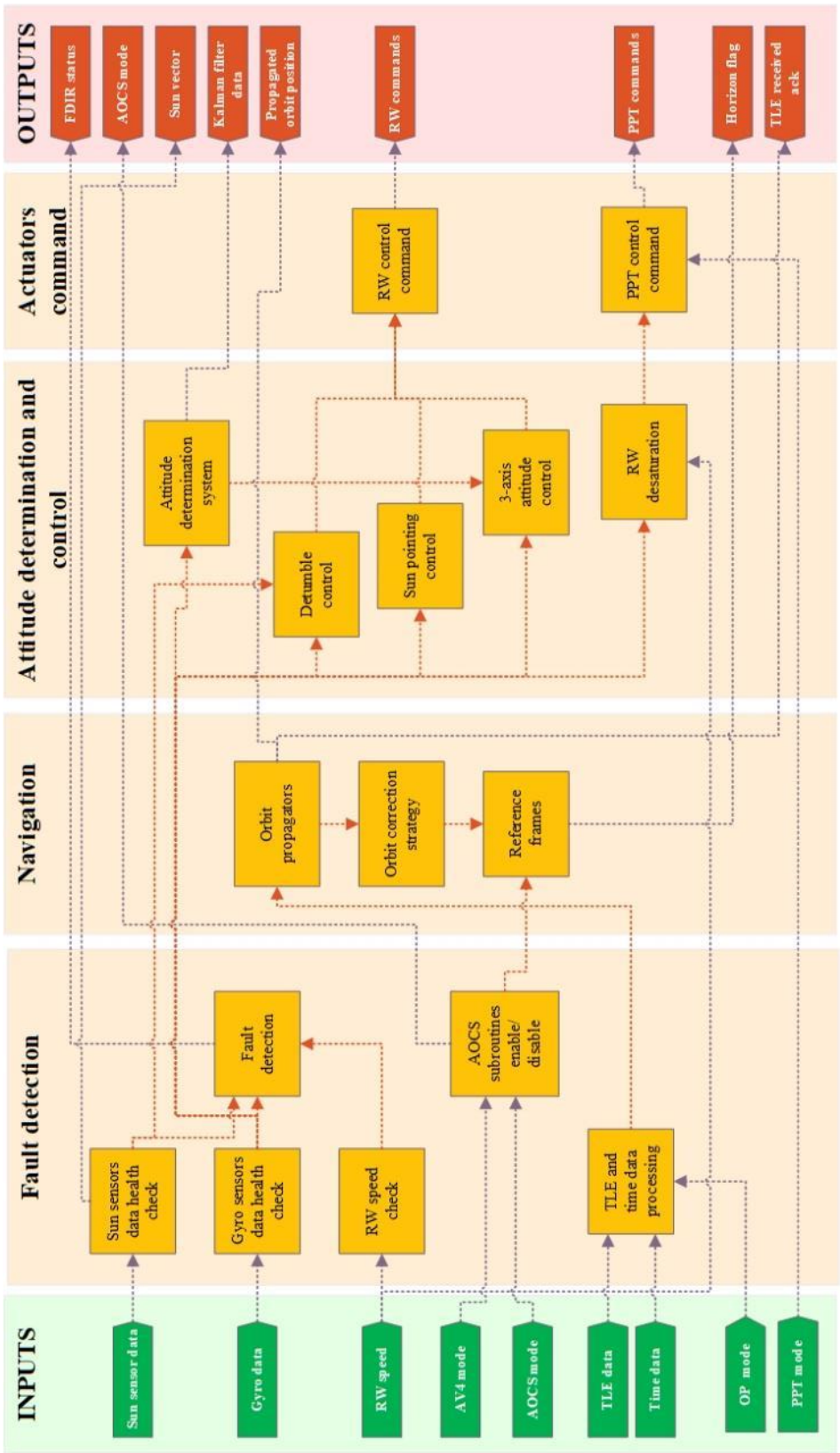

Figure 5.1 AOCS software overview

5.2 Inputs

In the next paragraphs, the following input data from OBC firmware of AV4 will be explained:

- TLE data
- TLE data sent flag
- Gyroscope data
- Sun sensors data
- CPU time
- Reaction wheels speed
- AOCS mode of operation
- AV4 mode of operation
- Orbit propagator method
- PPT ignitions frequency
- AOCS reset

5.2.1 TLE data

This input consists of 8 elements which contains the TLE information of AV4 once it is placed into orbit. By default, AV4 will receive TLE information from NORAD [37], whose elements considered for the AV4 orbit propagation are:

1. Year
2. Days of the year
3. Inclination
4. Ascending node
5. Eccentricity
6. Argument of perigee
7. Mean anomaly
8. Mean motion

Alternatively, orbit ephemeris from another ground station network can be sent to AV4, which can be formatted as NORAD standard or as follows:

1. Position (x) in ECI
2. Position (y) in ECI
3. Position (z) in ECI
4. Velocity (x) in ECI
5. Velocity (y) in ECI
6. Velocity (z) in ECI

7. Julian day starting from 2017/01/01 00:00:00
8. (Empty)

5.2.2 TLE data sent flag

Once OBC firmware send the TLE data to the AOCS software, this flag will be enabled as confirmation that TLE was received by ground station uplink command and sent to AOCS firmware. By enabling this flag, the AOCS software will update of the navigation module with the new information of the TLE data.

5.2.3 Gyroscope data

The gyroscope data (Table 3.1) contains the information of the AV4 angular rates in *x*, *y* and *z* axis. The incoming data of the gyroscope is calibrated in OBC firmware as specified in its datasheet.

5.2.4 Sun sensor data

The sun sensor data consists on a set of 14 values, which correspond to the coarse and fine sun sensors data (Table 3.1). In the following table, the order of the incoming sun sensor data is specified:

Table 5.1 Sun sensor data array

Index	**sensor**	**description**
1	CSS +*x*	CSS located at +x axis of AV4 body
2	CSS -*x*	CSS located at +x axis of AV4 body
3	CSS +*y*	CSS located at +x axis of AV4 body
4	CSS -*y*	CSS located at +x axis of AV4 body
5	CSS +*z*	CSS located at +x axis of AV4 body
6	CSS -*z*	CSS located at +x axis of AV4 body
7	FSS -*x*	Sector A of the FSS located at -x axis of AV4 body
8	FSS -*x*	Sector B of the FSS located at -x axis of AV4 body
9	FSS -*x*	Sector C of the FSS located at -x axis of AV4 body

10	FSS -*x*	Sector D of the FSS located at -x axis of AV4 body
11	FSS -*z*	Sector A of the FSS located at -z axis of AV4 body
12	FSS -*z*	Sector B of the FSS located at -z axis of AV4 body
13	FSS -*z*	Sector C of the FSS located at -z axis of AV4 body
14	FSS -*z*	Sector D of the FSS located at -z axis of AV4 body

5.2.5 CPU time

The OBC firmware will provide the UTC time information in YY-MM-DD hh:mm:ss. If required, the ground station will perform time calibration tasks, which is important to keep the accuracy of the algorithms running inside the navigation module.

5.2.6 Reaction wheel speed

The OBC firmware sends the reaction wheels' speed information (Table 3.1) in RPMs (+ for counter-clock wise spin and – for clockwise spin). The order of the data received from the OBC firmware is the reaction wheels' spin in *x*, *y* and *z* direction.

5.2.7 AOCS mode of operation

As mentioned in section 3.1.2, the AOCS software was designed to perform several attitude maneuvers in order to accomplish the AV4 mission objectives. Via ground station uplink command, the OBC firmware sets the AOCS mode of operation value to perform the following attitude maneuvers:

Table 5.2 AOCS modes of operation

Index	**Mode**	**Remarks**	**Description**
0	Detumble		Reduction of the satellite angular momentum
1	Sun tracking		Alignment of solar paddles and sun position
2	Auto detumble – sun tracking	Default	Automatic change between detumble and sun tracking
3	Sun tracking – horizon	Back-up of mode 6	During orbit sunrise and sunset event, the camera is aligned towards the sun position.

4	Sun tracking – Orbit maintenance	Back-up of mode 7	During orbit sunrise and sunset event, the z axis of the satellite is aligned towards sun, in such a way that PPT heads provide an impulsive force towards velocity vector approximately
5	Sun tracking – Initialization		The satellite initializes the attitude determination system while the solar paddles are aligned towards the sun position
6	Horizon detection		The camera is aligned towards Earth horizon for the observation of the orbit sunrise and sunset
7	Orbit maintenance		The PPT heads provide an impulsive force towards the thrust vector for orbit correction maneuvers
(any)	No control		No attitude control maneuvers are executed

The default mode of operation is set to the value 2, since AV4 satellite may run out of battery until the pass above a ground station after its deployment by the launcher.

Modes 3 and 4 serves as back-up of modes 5 and 6 respectively in case that the attitude determination system cannot be stabilized by tuning the Kalman filter parameters.

5.2.8 AV4 mode of operation

The AOCS software also receives the current AV4 mode of operation value (Figure 3.4) from OBC firmware. In the next table, the actions taken by the AOCS software based on the current AV4 mode of operation are explained:

Table 5.3 AV4 modes of operation and the actions taken by AOCS software

Index	**Mode**	**Actions taken**
0	Normal	Normal operation of AOCS software
1	Safe-hold	AOCS software change its mode of operation value to 2
2	Survival	AOCS software does not perform any attitude maneuver and all its subroutines are deactivated

5.2.9 Orbit propagation method

The orbit propagator used by AOCS software when the TLE data is received by AOCS software can be selected by setting any of the following values:

Table 5.4 Selection of the orbit propagation method

Index	Method	Remarks	Description
0	SGP4	Default	Implementation of the SGP4 orbit propagator
1	2-body	Experimental	Implementation of the two-body problem equation numerically solved by Runge-Kutta 4th order
2	n-body	Experimental	Implementation of the restricted n-body problem equation numerically solved by Runge-Kutta 4th order
(any)	none		Navigation module is deactivated

5.2.10 PPT ignitions mode

The PPT unit on-board is capable to produce ignitions from 1Hz to 4Hz. By setting a value in this input port, the ignitions frequency can be set up. As default value (0), the PPT unit will produce ignitions at 1Hz, but AOCS FDIR subroutine can determine the frequency of the PPT ignitions (Table 5.5). To enable the calculation of the PPT ignition frequency, the value 1 must be set.

Table 5.5 Determination of the PPT ignitions frequency

Index	Frequency	RW value
0	fixed, 1Hz	Any
1	1Hz	≤40% nominal speed
2	2Hz	40%<nominal speed≤60%
3	3Hz	60%<nominal speed≤80%
4	4Hz	>80% nominal speed

5.2.11 AOCS reset

By setting up the input value as 0, the AOCS software will operate normally. If it is set up as 1, the AOCS software will be deactivated and all the buffer data will be cleared.

5.3 Fault detection

The fault detection subroutine is structured by the following elements:

- Sun sensors and gyroscope data health
- Reaction wheels speed check

- TLE ant time data processing
- Fault detection decision chart
- AOCS subroutines enable/disable

The execution sequence of these elements of the fault detection subroutine is illustrated in the next figure:

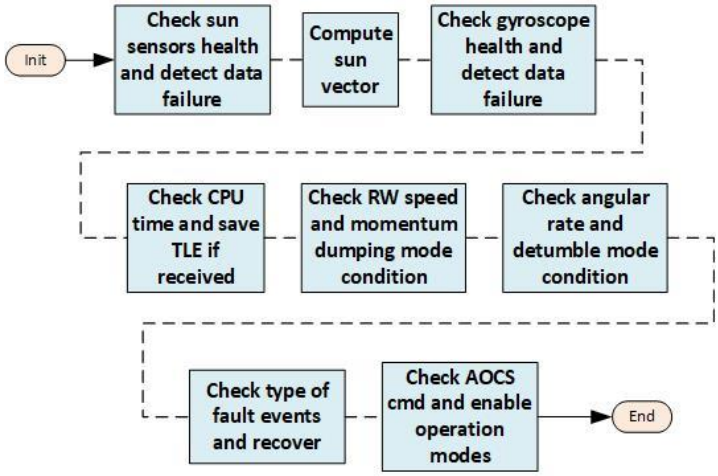

Figure 5.2 AOCS Fault detection general structure

5.3.1 Sun sensors and gyroscope data health

Both sets of sun sensors and gyroscope data are processed in a similar way to detect any outlier data; however, in the case of sun sensors data process, it is subject to sun/eclipse phase events. In the figure, the overview of the algorithm to analyse the health of the sensors data is shown.

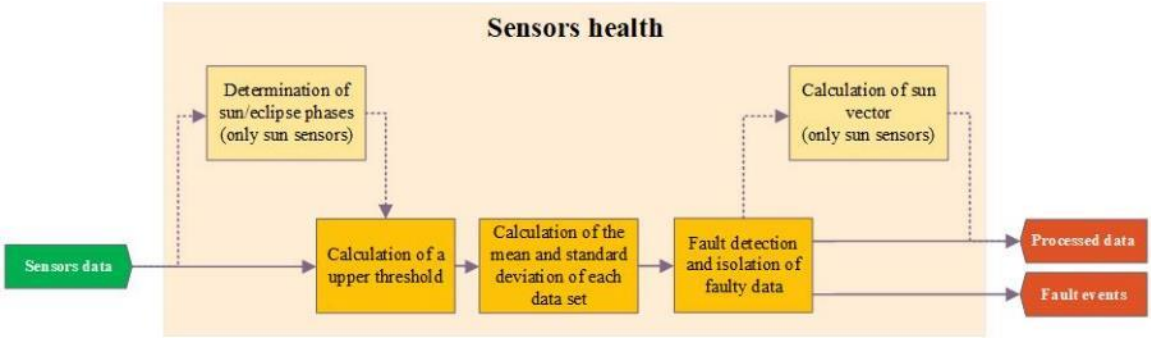

Figure 5.3 AOCS Fault detection subroutine – Sensor health analysis

The determination of Sun-eclipse phases is performed by calculating the magnitude of the coarse sun sensor vector and comparing it with a minimum threshold value. This threshold value is a tunable parameter that can be adjusted by uplink command.

The detection of outlier data is performed by calculating the mean and standard deviation of each data from the sensors *u* [38]. In this algorithm, *n* = 7 samples were considered:

$$\sigma^2 = \frac{1}{n-1}\sum_{i=0}^{n-1}(u_i - \mu)^2$$
$$\mu = \frac{1}{n}\sum_{i=0}^{n-1} u_i \tag{5.1}$$

Then, the resulting standard deviations are compared with an upper threshold value *y* multiplied by a tunable parameter β. The *y* value is previously calculated from the filtered time derivative data *x* of the magnitude of sensors *s*. The filter implemented in this algorithm is the single-pole low pass filter [38], where the parameter α is tuned according to each sensor data features:

$$\boldsymbol{y}_i = \beta[(1-\alpha)\boldsymbol{y}_{i-1} + \alpha\boldsymbol{x}_i]$$
$$\boldsymbol{x}_i = \frac{\boldsymbol{s}_i - \boldsymbol{s}_{i-1}}{\Delta t}$$
$$\boldsymbol{s}_i = \sqrt{u_1^2 + u_1^2 + \cdots + u_n^2} \tag{5.2}$$

If one value of the incoming data produces an increase in the standard deviation above the upper threshold value, an outlier data is detected and the previous data will be used for further calculations inside AOCS software. Additionally, if the standard deviation σ becomes zero (and the mean value μ is different from zero for sun sensors data) means that a data-stop or total failure event was detected. Table 3.3 explains the actions taken in case of a fault detection.

Regarding sun sensors, the sun vector calculation by using the coarse sun sensor $s_{b,CSS}$ is performed afterwards as follows:

$$\boldsymbol{s}_{b,CSS} = \frac{1}{2}\begin{bmatrix} s_1 - s_2 \\ s_3 - s_4 \\ s_5 - s_6 \end{bmatrix} \tag{5.3}$$

If fine sun sensors face towards sun direction, the sun vector $s_{b,FSS}$ is calculated as follows:

$$\begin{gathered} \boldsymbol{s}_{b,FSS} = \begin{bmatrix} \cos(\theta) \\ \sin(\theta)\cos(\phi) \\ \sin(\theta)\sin(\phi) \end{bmatrix} \\ \phi = \operatorname{atan}\frac{x_d}{y_d}, \;\; \theta = \operatorname{atan}\frac{\sqrt{x_d^2 + y_d^2}}{h} \\ \begin{bmatrix} x_d \\ y_d \end{bmatrix} = \begin{bmatrix} \cos(\delta) & \sin(\delta) \\ -\sin(\delta) & \cos(\delta) \end{bmatrix} \begin{bmatrix} \dfrac{(A+B)-(C+D)}{A+B+C+D} + x_0 \\ \dfrac{(A+D)-(B+C)}{A+B+C+D} + y_0 \end{bmatrix} \end{gathered} \tag{5.4}$$

where δ, x_0, y_0, and h are parameters provided by the manufacturer, the values *A*, *B*, *C* and *D* correspond to the s_{7-10} for the fine sun sensor located in -*x* axis and s_{11-14} for the fine sun sensor located in -*z* axis.

5.3.2 Reaction wheels speed check

The speed of the *i*-th each reaction wheel $\omega_{w,i}$ is monitored to prevent their saturation and consequently, the loss of AV4 attitude control capability. The activation or deactivation of the desaturation controller is performed by implementing a discontinuous hysteresis operator defined as follows:

$$w_{flag} = \begin{cases} 0, & \text{for } \omega_{w,i} < \omega_{min} \\ 1, & \text{for } \omega_{w,i} > \omega_{max} \\ 0 \text{ or } 1, & \text{for } \omega_{min} < \omega_{w,i} < \omega_{max} \end{cases} \tag{5.5}$$

5.3.3 TLE ant time data processing

The TLE and time information is stored into buffer variables for further calculations. In section 3.2.2, it was mentioned that ground station can send the orbital ephemeris of AV4 from either NORAD or another ground station network. Depending on the source of the orbital ephemeris, the initialization of the orbit propagator will be performed according to the following table:

Table 5.6 Initialization of the orbit propagator

Source of orbital ephemeris	**Type**	**Index**	**Type of initialization**
NORAD	TLE	0	None
Other	TLE	1	Convert TLE to initial states by Kepler equations and propagate till current time
Other	Initial states	2	Propagate till current time

Regarding the processing method of the time information YY/MM/DD hh:mm:ss, it is converted to Julian date for its use in the navigation subroutine by using the following equation [28]:

$$JD = 367(YY) - \text{int}\left\{\frac{7\left[YY + \text{int}\left(\frac{MM+9}{12}\right)\right]}{14}\right\} + \text{int}\left(\frac{275(MM)}{9}\right) + DD + 1{,}721{,}013.5 + \frac{\frac{ss}{60} + mm}{60} + \frac{hh}{24} \tag{5.6}$$

The detection of any time calibration event is performed by comparing the previous and current time information (Δt_0). If a calibration event is detected, the following action will be taken in order to avoid further miscalculations in other algorithms that perform differentiation or integration tasks:

Table 5.7 Detection of time calibration events

Δt_0 detected	**Output**

$\Delta t_0 > 1$	$\Delta t = 1$
$\Delta t_0 \leq 0$	$\Delta t = 0$
$\Delta t_0 = 1$	$\Delta t = 1$

5.3.4 Sensor health and fault detection

In Table 3.3, the type of failure and countermeasure actions was presented. According to the index output of the resulting sensor data analysis as explained in section 5.3.1, the AOCS mode of operation value can be updated for a safer satellite operation, as shown in the following table:

Table 5.8 Fault detection decision chart

Sensors	***Fault type***	***Index***	***AOCS mode of operation update***
No fault	n/a	0	Normal operation
FSS or CSS or GYRO	outlier value	1	Normal operation
FSS -x or -z	total	2	Normal operation
CSS -x or -z	total	3	Normal operation
CSS ±y and/or +x and/or +z	total	4	if AOCS mode > 4, then AOCS mode=1 (loss of sun sensor redundancy)
GYRO	total	5	if AOCS mode > 4, then AOCS mode=1 (Angular rates can be estimated from sun sensors along Sun direction)
GYRO and FSS	total	6	if AOCS mode > 4, then AOCS mode=1 (Angular rates can be estimated from sun sensors along Sun direction)
GYRO and CSS	total	7	if AOCS mode > 4, then AOCS mode=1 (Angular rates can be estimated from sun sensors along Sun direction, eclipse events frequently detected)
CSS and FSS	total	8	AOCS mode=0 (Loss of attitude information)
GYRO, CSS and FSS	total	9	AOCS mode>7 (No control)

When gyroscope data is not available anymore, the angular rates can be estimated from sun sensors along Sun direction. In this way, a safe angular rate reduction can be performed. Considering that the time derivative of a unit vector is calculated as $\dot{\boldsymbol{s}}_b \approx -\boldsymbol{w}_s \times \boldsymbol{s}_b = -S(\boldsymbol{w}_s)\boldsymbol{s}_b = S(\boldsymbol{s}_b)\boldsymbol{w}_s$, it is possible to find w_s [39]:

$$\boldsymbol{w}_s = S^{\top}(\boldsymbol{s}_{b,k})\dot{\boldsymbol{s}}_b = -\frac{S(\boldsymbol{s}_{b,k})(\boldsymbol{s}_{b,k} - \boldsymbol{s}_{b,k-1})}{\Delta t} \tag{5.7}$$

5.3.5 AOCS subroutines enable/disable

According to the AOCS mode of operation value, the fault detection subroutine enables/disables the AOCS subroutines according to the next table:

Table 5.9 AOCS modes of operation and subroutines

Index	**Mode**	**AOCS subroutines enabled**
AV4 normal mode operation		
0	Detumble	Navigation, detumble controller
1	Sun tracking	Navigation, sun tracking controller
2	Auto detumble – sun tracking	Navigation, detumble/sun tracking controller
3	Sun tracking – horizon	Navigation, sun tracking controller
4	Sun tracking – Orbit maintenance	Navigation, sun tracking controller
5	Sun tracking – Initialization	Navigation, attitude determination system, three-axis attitude control
6	Horizon detection	Navigation, attitude determination system, three-axis attitude control
7	Orbit maintenance	Navigation, attitude determination system, three-axis attitude control, PPT alternate ignitions enabled only in sun-phase
(any)	No control	None
AV4 safe-hold mode operation		
0	Detumble	detumble controller
1	Sun tracking	sun tracking controller

2	Auto detumble – sun tracking	detumble/sun tracking controller
(any)	No control	None
AV4 critical mode operation		
(any)	No control	None

5.4 Navigation

This subroutine contains the orbit propagation algorithms, the thrust vector calculation algorithm for orbit correction maneuvers and the reference frames operations. During AV4 normal mode of operation, this subroutine is enabled and will propagate its position and velocity parameters once receiving a TLE information from ground station. The execution sequence of the navigation subroutine is illustrated in the next figure:

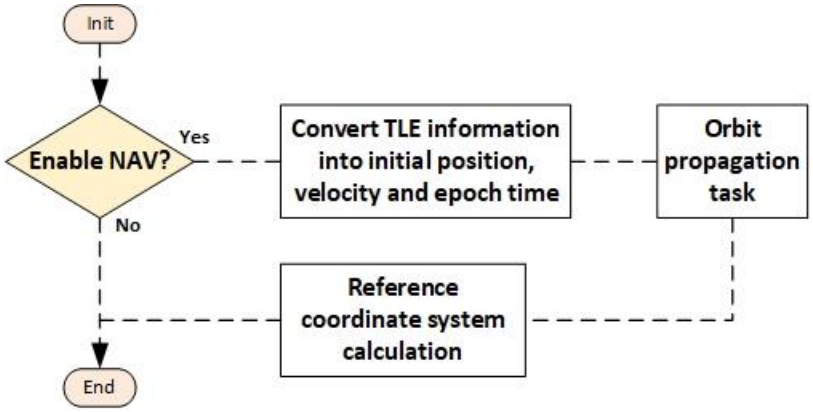

Figure 5.4 AOCS navigation subroutine general structure

5.4.1 Initialization of the orbit propagation

The initialization process of the orbit propagation is executed if the TLE information comes from another source different from NORAD or if the selected orbit propagator is different from SGP4 (Table 5.10).

Table 5.10 Initialization of the orbit propagator

Orbit propagation mode	Source of orbital ephemeris	Initialization type
0 (SGP4)	TLE NORAD	none
	TLE from another source	none
	Initial state vector another source	n/a
1 (2-body equation)	TLE NORAD	Initial state calculated by SGP4
	TLE from another source	Kepler equations and propagation (2-body) from epoch to current time
	Initial state vector another source	Propagation (2-body) from epoch to current time
2 (n-body equation)	TLE NORAD	Initial state calculated by SGP4
	TLE from another source	Kepler equations and propagation (n-body) from epoch to current time
	Initial state vector another source	Propagation (n-body) from epoch to current time

The initialization of the orbit propagator (if applicable) consists on the calculation of the initial states of the n-body orbit propagator via Kepler equation. Since this initial state is calculated at epoch time, an additional propagation step (either 2-body or n-body) is required. The calculation of the initial states based in Kepler equation is shown as follows [28] [40]:

1. Calculation of the Julian day at epoch (JD_0) from TLE epoch time YY_0 and DD_0

$$JD_0 = 367(YY_0) - \text{int}\left\{\frac{7\left[YY_0 + \text{int}\left(\frac{1+9}{12}\right)\right]}{14}\right\} + \text{int}\left(\frac{275(1)}{9}\right) + DD_0 + 1{,}721{,}013.5 - \frac{1}{2}\text{sgn}(100(YY_0) + 1 - 190{,}002.5) + \frac{1}{2} \quad (5.8)$$

2. Kepler equation from TLE orbital ephemeris (mean motion *n*, mean anomaly M_0, eccentricity *e*)

$$a = \sqrt[3]{\frac{\mu_E}{n^2}}$$
$$M = M_0 + n\Delta t, \qquad \Delta t = t_n - t_{n-1}$$

IF $-\pi < M < 0$ or $M > \pi$

let $E = M - e$

ELSE

let $E = M + e$ (5.9)

LOOP

$$E_{n+1} = E_n + \frac{M - E_n + e\sin(E_n)}{1 - e\cos(E_n)}$$

UNTIL $|E_{n+1} - E_n| <$ tolerance

3. Calculation of position $\boldsymbol{r}_o = [x, y, z]$ in orbit frame

$$x = a\cos(E) - ae$$
$$y = a\sin(E)\sqrt{1 - e^2} \quad (5.10)$$
$$z = 0$$

4. Orbit frame to ECI frame by using the TLE orbital ephemeris (inclination i, argument of perigee w, right ascension of the ascending node Ω)

$$\boldsymbol{r}_i = R_z(\Omega)R_x(i)R_z(w)\boldsymbol{r}_o$$
$$\boldsymbol{v}_i = \frac{\boldsymbol{r}_{i,n} - \boldsymbol{r}_{i,n-1}}{\Delta t} \quad (5.11)$$

After the initialization of the orbit propagator, the navigation subroutine set a flag value as 1 as an acknowledgement of the TLE received, until OBC firmware clears the buffer memory where TLE data is saved.

5.4.2 Orbit propagation algorithms

The navigation subroutine includes 3 orbit propagators:

- SGP4 [41]
- 2-body [28]
- n-body [28]

The SGP4 orbit propagator was developed by Ken Cranford in 1970 and it is the second of five mathematical models (SGP, SGP4, SDP4, SGP8 and SDP8) for prediction of the satellite position and velocity by using only the TLE orbit information from NORAD [41]. The discussion regarding the SGP4 mathematical model is beyond the scope of this research; however, more details can be found in the cited report.

The 2-body and n-body orbit propagator are implemented according to the equation (4.19), which is solved numerically via 4th order Runge-Kutta solver as shown below [42]:

$$\begin{aligned} k_0 &= h\mathrm{F}(x, y) \\ k_1 &= h\mathrm{F}\left(x + \frac{h}{2}, y + \frac{k_0}{2}\right) \\ k_2 &= h\mathrm{F}\left(x + \frac{h}{2}, y + \frac{k_1}{2}\right) \\ k_3 &= h\mathrm{F}(x + h, y + k_2) \\ y(x + h) &= y(x) + \frac{1}{6}(k_0, 2k_1, 2k_2, k_3) \end{aligned} \tag{5.12}$$

where:

$$\mathrm{F}(x, y) = \begin{bmatrix} \dot{\boldsymbol{r}}_{E,sc} \\ \ddot{\boldsymbol{r}}_{E,sc} \end{bmatrix} \tag{5.13}$$

For the n-body propagator, $\ddot{\boldsymbol{r}}_{E,sc} = \boldsymbol{a}_M + \boldsymbol{a}_E + \boldsymbol{a}_S + \boldsymbol{a}_{sp}$ as (4.19) but using 5 zonal harmonics of the Earth's gravitational field (J_2, J_3, J_4, J_5, J_6) for the calculation of $\boldsymbol{a}_E$; whereas the 2-body problem considers $\ddot{\boldsymbol{r}}_{E,sc} = \boldsymbol{a}_E$, with $\boldsymbol{a}_E = \mu_E\left(\boldsymbol{r}_{E,sc}/r_{E,sc}^3\right)$.

5.4.3 Calculation of the thrust vector

The orbit control strategy is based on the calculation of the optimal in-plane thrust vectors for each target orbital parameter suggested by Ruggiero [43] and its enhancement proposed by Falck [44] with the Directional Adaptive Guidance (DAG) Algorithm, whose performance relies on the tuning of priority weighing factors.

This strategy relies on the calculation of an unit thrust vector $\boldsymbol{f}_{op,j}^{\mathrm{RCN}}$ for a *j*-th orbital parameter (*op*,*j*) to be corrected, i.e. eccentricity (*e*) and semi-major axis (*a*), expressed in the left-handed rule reference frame RCN as shown in Figure , where $\hat{r}$ is the radial component R aligned towards Zenith direction, $\hat{n}$ is aligned with the normal vector N of the orbital plane and $\hat{c}$ is the circumferential component C that completes the left-handed triad of unit vectors. The time rates of change of the aforementioned orbital parameters due to the external perturbation $\boldsymbol{f}_{op,j}^{\mathrm{RCN}}$ is expressed in its Gauss form as [43]:

$$\begin{aligned}\frac{da}{dt} &= \frac{2a^2}{h}\left\{e\left\|\boldsymbol{f}_{op,j}^{\mathrm{RCN}}\right\|\hat{r}\sin\nu + \frac{p}{r}\left\|\boldsymbol{f}_{op,j}^{\mathrm{RCN}}\right\|\hat{c}\right\} \\ \frac{de}{dt} &= \frac{1}{h}\left\{p\left\|\boldsymbol{f}_{op,j}^{\mathrm{RCN}}\right\|\hat{r}\sin\nu + \left\|\boldsymbol{f}_{op,j}^{\mathrm{RCN}}\right\|\hat{c}[(p+r)\cos\nu + re]\right\}\end{aligned} \tag{5.14}$$

where p is the semilatus rectum, ν is the true anomaly, r is the distance of the spacecraft from the central body and h is the orbit angular momentum. This unit thrust vector $\boldsymbol{f}_{op,j}^{\mathrm{RCN}}$ can be expressed as a function of an in-plane and out-plane thrust angles $\alpha_{op,j}$ and $\beta_{op,j}$ respectively, as shown below:

$$\boldsymbol{f}_{op,j}^{\mathrm{RCN}} = \begin{bmatrix}\cos\beta_{op,j}\sin\alpha_{op,j} \\ \cos\beta_{op,j}\cos\alpha_{op,j} \\ \sin\beta_{op,j}\end{bmatrix} \tag{5.15}$$

The value of $\alpha_{op,j}$ starts from $\hat{c}$ axis along the orbital plane and the value of $\beta_{op,j}$ starts from the plane RC. Substituting equation (5.15) to equation (5.14), the relationship between the thrust angle and the instantaneous variation of the orbital parameters is obtained:

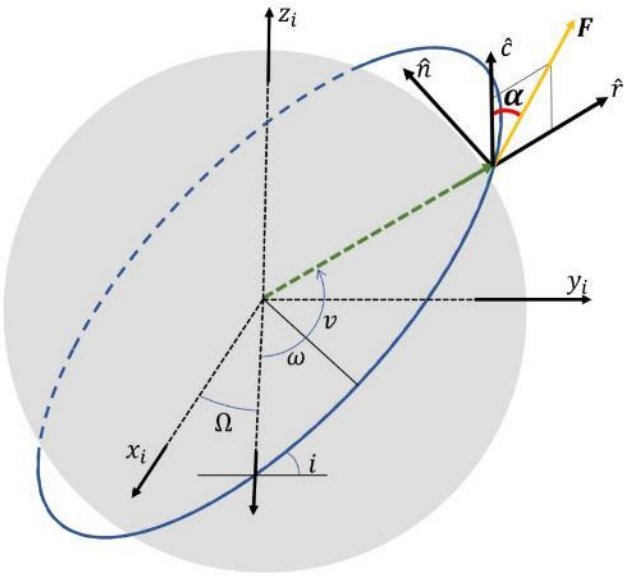

Figure 5.5 AOCS navigation subroutine general structure

$$\frac{da}{dt} = \frac{2a^2}{h}\cos\beta_{op,j}\left\{e\sin\alpha_{op,j}\sin\nu + \frac{p}{r}\cos\alpha_{op,j}\right\}$$
$$\frac{de}{dt} = \frac{1}{h}\cos\beta_{op,j}\left\{p\sin\alpha_{op,j}\sin\nu + \cos\alpha_{op,j}\left[(p+r)\cos\nu + re\right]\right\} \quad (5.16)$$

Taking the first partial derivative of equation (5.16) respect to the thrust angles, the value of the thrust angles $\alpha_{op,j}$ and $\beta_{op,j}$ can be calculated (Table 5.11), concluding that the instantaneous flight path angle in RCN frame enables the maximum j-th orbital parameter rate of change for in-plane orbital maneuvers, i.e. $\beta_{op,j}$= 0 [43].

Table 5.11 Calculation of thrust angles

Orbital parameter (op)	In-plane thrust angle	Out-plane thrust angle
Semi-major axis a	$\alpha_a = \tan^{-1}\left(\frac{e\sin\upsilon}{1+e\sin\upsilon}\right)$	$\beta_a = 0$
Eccentricity e	$\alpha_e = \tan^{-1}\left(\frac{\sin\upsilon}{\cos\upsilon+\cos E}\right)$	$\beta_e = 0$

In accordance to Ruggiero [43], it is also possible to determine the ΔV required for a quasi-circular orbit, to obtain a desired change in eccentricity, semi-major axis or inclination. Particularly on the correction of the inclination, we can derive the maximum change of inclination that a CubeSat is able to achieve, considering the implementation of the proposed orbit correction maneuvers and assuming the utilization of an EPS featuring a particular ΔV and I_{bit} capacity. In section 6.3.3, we show our simulation results related with the capacity of a CubeSat to extend its mission lifetime by either performing in-plane orbital maneuvers or fleeing from an UR to a stable orbit by correcting its orbital inclination.

Table 5.12 Equations for the calculation of the required ΔV for the change of a particular orbital parameter

	ΔV
Eccentricity *e*	$\Delta V = \frac{2}{3}\sqrt{\frac{\mu_M}{a}}\left\lvert \sin^{-1} e_1 - \sin^{-1} e_2 \right\rvert$
Semi-major axis *a*	$\Delta V = \left\lvert \sqrt{\frac{\mu_M}{a_0}} - \sqrt{\frac{\mu_M}{a_1}} \right\rvert$
Inclination *i*	$\Delta V = V\sqrt{2 - 2\cos\left(\frac{\pi}{2}\Delta i\right)}$

In order to target the simultaneous correction of several orbital elements, the *j*-th thrust vector $\boldsymbol{f}_{op,j}^{\mathrm{RCN}}$ is multiplied by an adaptive ratio $R_{f,j}$ according to Falck's DAG algorithm [44], which serves as a priority weighting factor and is computed by taking each of the instantaneous orbital parameter *op*, its target value op_r (i.e. 1000km altitude circular orbit) and initial value op_o after initializing the orbit correction maneuver:

$$R_{f,j} = \frac{op_r - op}{op_r - op_o} \tag{5.17}$$

Furthermore, an additional weight $W_{op,j}$ was used to provide an additional weighting factor based on successive iterations that we conducted through our simulation scheme. Since a PPT unit produces a fixed impulsive force, the spacecraft may keep correcting its

orbital parameters even though they are close to the nominal orbit parameter, turning into an inefficient use of the PPT unit. Following Falck's DAG algorithm [44], an stopping scheme is implemented, which serves as a mechanism for the deactivation of the orbit correction maneuvers once the spacecraft reaches a stopping tolerance, determined by an inner and upper threshold value for each target value of the orbital parameters ($t_{op,min}$ and $t_{op,max}$ respectively). Thus, $W_{op,j}$ can be rewritten as:

$$W_{op,j}(\delta_r) = \delta_r w_{op,j} \tag{5.18}$$

where $w_{op,j}$ is a weighting factor, and δ_r is a discontinuous hysteresis operator defined as:

$$\delta_r = \begin{cases} 0, & \text{for } |op - op_r| < t_{op,min} \\ 1, & \text{for } |op - op_r| > t_{op,max} \\ 0 \text{ or } 1, & \text{for } t_{op,min} < |op - op_r| < t_{op,max} \end{cases} \tag{5.19}$$

Therefore, the total thrust vector $\boldsymbol{F}_{total}^{\mathrm{RCN}}$ is calculated as the sum of the weighted thrust vectors $W_{op,j} R_{f,j} \boldsymbol{f}_{op,j}^{\mathrm{RCN}}$ for each orbital parameter to be corrected, as shown below:

$$\boldsymbol{F}_{total}^{\mathrm{RCN}} = \sum W_{op,j} R_{f,j} \boldsymbol{f}_{op,j}^{\mathrm{RCN}} w_{op,j} \tag{5.20}$$

The transformation of $\boldsymbol{F}_{total}^{\mathrm{RCN}}$ from RCN to inertial frame *I* is computed as follows:

$$\boldsymbol{F}_T^I = T_z(\Omega) T_x(i) T_z(\omega) \boldsymbol{F}_{total}^{\mathrm{RCN}} \tag{5.21}$$

where *T* is a rotation matrix along a specified coordinate axis, Ω is the RAAN, ω is the argument of periapsis and *i* is the inclination.

5.4.4 Calculation of the orbit reference frames

According to the AOCS mode of operation, a reference coordinate frame is selected and its corresponding calculation are performed based on the current orbital position and velocity (Table 5.13).

Table 5.13 AOCS modes of operation and the calculation of reference frames

Index	Mode	Calculation of a reference frame
0	Detumble	n/a
1	Sun tracking	n/a
2	Auto detumble – sun tracking	n/a
3	Sun tracking – horizon	Calculation of the lapse time during the orbit sunrise/sunset event
4	Sun tracking – Orbit maintenance	Calculation of the lapse time before/after the orbit sunrise/sunset
5	Sun tracking – Initialization	n/a
6	Horizon detection	Horizon/Sun/Orbit system
7	Orbit maintenance	Thrust/Sun/Orbit system
(any)	No control	n/a

For the AOCS mode of operation 3 and 4, either +*z* of -*z* axis of the satellite is aligned towards Sun of the satellite is located within the range γ (Figure 5.6), which depends on the current satellite velocity and sun vector.

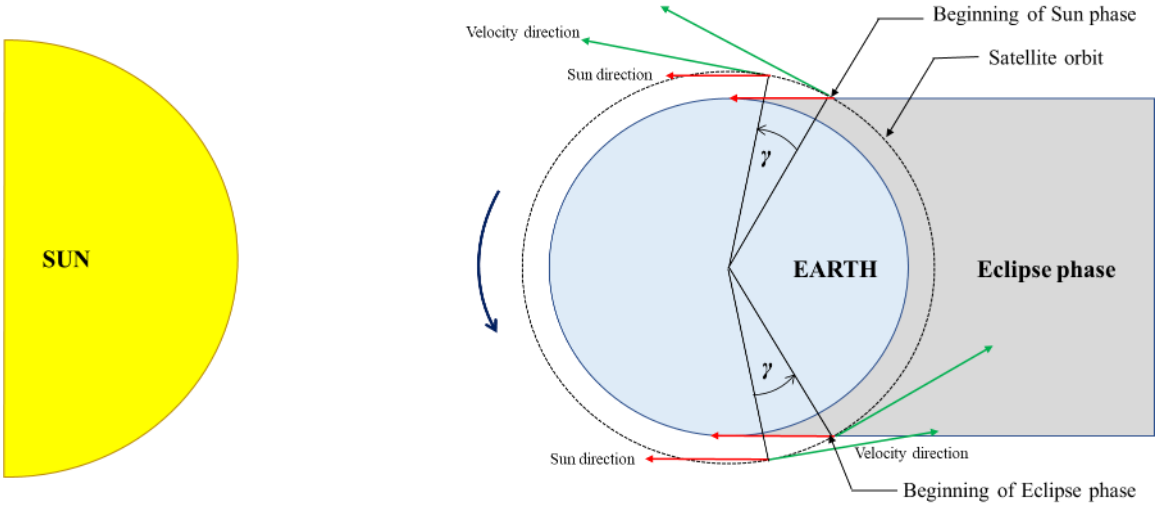

Figure 5.6 Sun tracking strategy for horizon and orbit maintenance mode of operation

First, the cosine angle between the velocity vector and sun vector in ECI is calculated, as well as its time derivative to determine the event when satellite either leave or enter into eclipse phase, as shown in the following equation:

$$\cos\beta = \frac{\boldsymbol{v}}{\|\boldsymbol{v}\|} \cdot \frac{\boldsymbol{s}}{\|\boldsymbol{s}\|}$$

$$\frac{d\cos\beta}{dt} = \frac{\cos\beta_k - \cos\beta_{k-1}}{\Delta t} \tag{5.22}$$

If $\cos\beta < \cos\beta_{MAX}$ and $d(\cos\beta)/dt < 0$, the satellite will align the camera axis with the Sun vector after leaving eclipse phase (AOCS mode of operation 3 and 4). Also, the satellite will align either the camera axis or PPT axis towards Sun before entering into eclipse phase (AOCS mode of operation 3 and 4 respectively). The size of the range γ depends on the value of β_{MAX}.

For the AOCS mode of operation 5 and 6, equations (4.7), (4.8) and (4.9) are used to calculate the reference frame.

5.5 Attitude determination

Considering the available attitude sensors, an attitude determination system was implemented based on the extended Kalman Filter. The EKF is used to estimate and propagate the attitude parameters of the satellite. Because it is well known that at least two vector measurements are required to determine the satellite three-axis attitude information in terms of a unit quaternion, the attitude determination strategy relies only on the sun vector information and the initial condition used for the attitude estimation and propagation. As shown in Figure 5.7, the EKF algorithm estimates the gyroscope bias first; then, the corrected gyroscope data is used with the calculated sun vector in body frame to estimate the 3-axis attitude for the satellite.

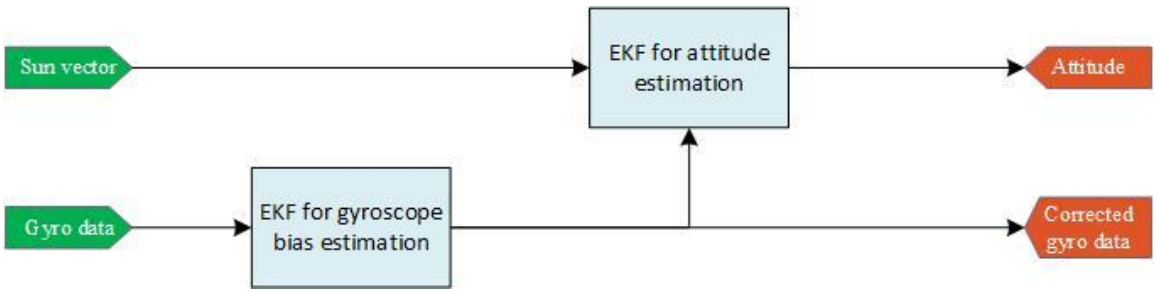

Figure 5.7 Attitude determination system general structure

The attitude estimation process consists on the attitude estimation in Sun phase and its propagation in eclipse phase, by merging two different innovation processes [45].

The design of the EKF considers a non-linear system as follows:

$$\begin{aligned} \dot{\boldsymbol{x}} &= f(\boldsymbol{x}, \boldsymbol{u}, t) + \boldsymbol{w}(t) \\ \boldsymbol{z} &= h(\boldsymbol{x}, t) + \boldsymbol{v}(t) \end{aligned} \tag{5.23}$$

The measurement and processes covariance matrix Q_k and R_k respectively is given by:

$$\begin{aligned} E\left[w_j w_i^{\top}\right] &= \begin{cases} Q, & i = j \\ 0, & i \neq j \end{cases} \\ E\left[v_j v_i^{\top}\right] &= \begin{cases} R, & i = j \\ 0, & i \neq j \end{cases} \\ E\left[w_j v_i^{\top}\right] &= 0, \text{for all } i \text{ and } j \end{aligned} \tag{5.24}$$

The EKF requires the computation of the matrix F_k and H_k, which are linearized functions from $f(\boldsymbol{x}, \boldsymbol{u}, t)$ and $h(\boldsymbol{x}, t)$ along the trajectory of the estimated variables $\hat{x}$:

$$F_k = \left.\frac{\partial f(\boldsymbol{x}, \boldsymbol{u}, t)}{\partial \boldsymbol{x}}\right|_{\boldsymbol{x}=\hat{\boldsymbol{x}}_k} \quad H_k = \left.\frac{\partial h(\boldsymbol{x}, t)}{\partial \boldsymbol{x}}\right|_{\boldsymbol{x}=\hat{\boldsymbol{x}}_k} \tag{5.25}$$

The EKF algorithm implemented in this subroutine consists on the following steps [46] [47]:

Step 1, Kalman gain calculation:

$$K_k = P_k^- H_k^{\top}(\hat{\boldsymbol{x}}_k^-)[R + H_k(\hat{\boldsymbol{x}}_k^-) P_k^- H_k^{\top}(\hat{\boldsymbol{x}}_k^-)]^{-1} \tag{5.26}$$

Step 2, Innovation process

$$\begin{aligned} \hat{\boldsymbol{x}}_k &= \hat{\boldsymbol{x}}_k^- + K_k \boldsymbol{\nu}_k \\ \boldsymbol{\nu}_k &= \boldsymbol{z}_k - H_k(\hat{\boldsymbol{x}}_k^-)\hat{\boldsymbol{x}}_k^- \end{aligned} \tag{5.27}$$

Step 3, Error covariance matrix update

$$P_k = P_k^- - K_k H_k(\hat{\boldsymbol{x}}_k) P_k^- \tag{5.28}$$

Step 4, Propagation of attitude states:

$$\begin{gathered} \hat{\boldsymbol{x}}_{k+1}^- = \hat{\boldsymbol{x}}_k + \int_k^{k+1} f(\hat{\boldsymbol{x}}_k, \boldsymbol{u}, t) dt \\ P_{k+1}^- = \phi_k P_k \phi_k^\top + Q \\ \phi_k = \exp(F_k \Delta t) \end{gathered} \tag{5.29}$$

In the following table, the functions implemented on each EKF algorithms are summarized [48] [49] [50]:

Table 5.14 EKF functions implemented into the AOCS software

Function	**EKF for bias estimation**	**EKF for attitude estimation**
$\boldsymbol{x}$	$\begin{bmatrix} \boldsymbol{\omega}_b^i \\ \boldsymbol{b} \end{bmatrix}$	$\boldsymbol{q}_b^i$
$f(\boldsymbol{x}, \boldsymbol{u}, t)$	$\begin{bmatrix} \boldsymbol{\omega}_b^i \times \left(J\boldsymbol{\omega}_b^i + AJ_w\boldsymbol{\omega}_w^b\right) - AJ_w\dot{\boldsymbol{\omega}}_w^b + w_\omega(t) \\ w_b(t) \end{bmatrix}$	$\begin{bmatrix} q_{b,4}^i \cdot \boldsymbol{\omega}_b^i - \boldsymbol{\omega}_b^i \times \boldsymbol{q}_b^i \\ -\boldsymbol{q}_b^{i\,\top} \boldsymbol{\omega}_b^i \end{bmatrix}$
$h(x,t)$	$\boldsymbol{\omega}_b^i + \boldsymbol{b} + \boldsymbol{v}(t)$	$R(\mathbf{q}_b^i)\boldsymbol{s}_i + \boldsymbol{v}(t)$
Q	$\begin{bmatrix} \sigma_{\boldsymbol{\omega}}^2 I^{3\times3} & 0^{3\times3} \\ 0^{3\times3} & \sigma_{\boldsymbol{b}}^2 I^{3\times3} \end{bmatrix}$	$\sigma_{\boldsymbol{q}}^2 I^{4\times4}$
R	$\sigma_{Gyro}^2 I^{3\times3}$	$\sigma_{SS}^2 I^{3\times3}$
F_k	$\begin{bmatrix} 0^{3\times3} & 0^{3\times3} \\ 0^{3\times3} & \left.\dfrac{\partial f(\boldsymbol{x}, \boldsymbol{u}, t)}{\partial \boldsymbol{\omega}_b^i}\right\|_{\boldsymbol{\omega}_b^i = \hat{\boldsymbol{\omega}}_k} \end{bmatrix}$	$\left[\left.\dfrac{\partial f(\boldsymbol{x}, \boldsymbol{u}, t)}{\partial \mathbf{q}_b^i}\right\|_{\mathbf{q}_b^i = \hat{\mathbf{q}}_k}\right]$
H_k	$[I^{3\times3} \quad I^{3\times3}]$	$\left[\dfrac{\partial R(\mathbf{q}_b^i)\boldsymbol{s}_i}{\partial \mathbf{q}_b^i}\right]$
$\boldsymbol{v}_k$	$(\boldsymbol{\omega}_{gyro} - \boldsymbol{b}) - \hat{\boldsymbol{\omega}}_{k-1}$	$\boldsymbol{s}_{SS} - R(\hat{\mathbf{q}}_{k-1})\boldsymbol{s}_i$
$\hat{\boldsymbol{x}}_k$	$\begin{bmatrix} \hat{\boldsymbol{\omega}}_{k-1} \\ \hat{\boldsymbol{b}}_{k-1} \end{bmatrix} + K_k \boldsymbol{v}_k$	$[\hat{\mathbf{q}}_{k-1} \otimes \Delta\mathbf{q}]$, $\Delta\mathbf{q}_{upd} = \begin{bmatrix} K_k \boldsymbol{v}_k \\ \sqrt{\mathbf{1} - (K_k \boldsymbol{v}_k)(K_k \boldsymbol{v}_k)^\top} \end{bmatrix}$

5.6 Attitude Control

The attitude control strategy is selected according to the AOCS mode of operation value (Table 5.2). The attitude control subroutine consists of 4 control laws which are enabled according the AOCS mode of operation:

- Detumble control
- Sun pointing control
- 3-axis control
- PPT command calculation for either desaturation of reaction wheels or orbit correction

In the following flowchart, the selection of the attitude controller is illustrated.

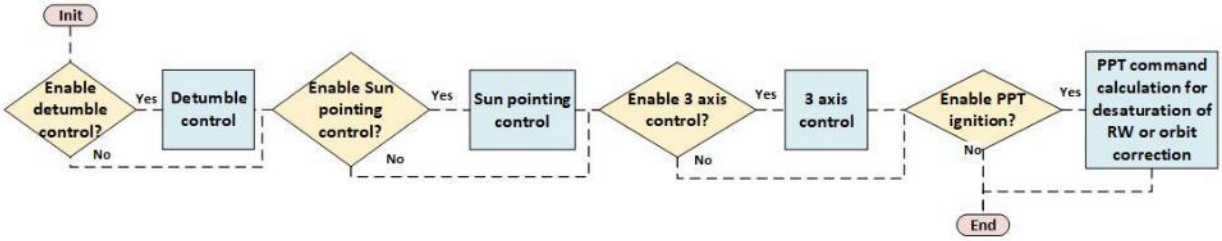

Figure 5.8 Attitude control subroutine flowchart

5.6.1 Detumble control (AOCS mode 0 or 2)

This control law is used when the satellite reaches a maximum allowed angular rate measured by the gyroscope. The following control law was implemented to reduce the satellite's angular rate by using reaction wheels:

$$\boldsymbol{\tau} = -k_{det}\boldsymbol{\omega}_b^i \tag{5.30}$$

5.6.2 Sun pointing control (AOCS mode 1, 2, 3 or 4)

By using the calculated sun vector from sun sensors and the measured angular rate from the gyroscope, the control torque is calculated by implementing the following control law:

$$\boldsymbol{\tau} = -k_s(\boldsymbol{s}_b \times \boldsymbol{s}_{ref}) - k_g \boldsymbol{\omega}_b^i \tag{5.31}$$

where the reference vector $\boldsymbol{s}_{ref}$ is determined according to the mode of operation. The nominal reference vector value is [-1, 0, 0] (solar paddles axis). For AOCS mode 3, the reference vector $\boldsymbol{s}_{ref}$ is set to [0, 0, 1] (camera axis) when the sunrise/sunset event is detected. For AOCS mode 4, the reference vector $\boldsymbol{s}_{ref}$ is set to either [0, 0, 1] (camera axis) or [0, 0, -1] (PPT axis) according to the algorithm described in section 5.4.4.

5.6.3 3-axis control (AOCS mode 5, 6 or 7)

This controller was designed by considering the *m*-layer cascade saturation controller [51] and it is implemented to perform attitude maneuvers for the accomplishment of the AV4 science mission. The calculation of the control torque is performed based on the following control law:

$$\boldsymbol{\tau} = -K\,\mathrm{sat}(\boldsymbol{P}_q) - C\,\boldsymbol{\omega}_b^i \tag{5.32}$$

where,

$$\begin{gathered} K = \mathrm{diag}(k_1, k_2, k_3)J \\ \boldsymbol{k} = [k_1 \quad k_2 \quad k_3]^\top = k_c \omega_{max}\,\mathrm{abs}(\Delta \boldsymbol{q}_{init}) \\ \Delta \mathbf{q}_{init} = \begin{bmatrix} \Delta \boldsymbol{q}_{init} \\ \Delta q_{init,4} \end{bmatrix} \\ C = k_w J \end{gathered} \tag{5.33}$$

The initial value of the attitude error $\Delta \mathbf{q}_{init}$ between the current attitude and its reference error is determined after initializing this control algorithm and is calculated by performing a quaternion product, as shown in equation (4.12). The value of each element of $\Delta \mathbf{q}_{init}$ is also limited by a threshold value k_{min}. ω_{max} is the maximum angular rate and J is the satellite inertia matrix. The value of $\mathrm{sat}(\boldsymbol{P}_q)$ is determined as follows:

$$\text{sat}(\boldsymbol{P}_q) = \begin{cases} k_{sat}, \text{when } |P_{q,i}| \geq k_{sat} \\ P_{q,i}, \text{when } |P_{q,i}| < k_{sat} \end{cases}$$
$$\boldsymbol{P}_q = K_p \Delta \mathbf{q} \tag{5.34}$$

5.6.4 PPT command calculation

When the command related with the desaturation of reaction wheels is disabled, the output of this algorithm is fixed in such a way that the ignitions produced by the PPT unit will be either deactivated or enabled for orbit maintenance maneuvers.

The control algorithm that allows the desaturation of the reaction wheels via PPT ignitions is implemented by considering the current momentum of the satellite and the speed of the reaction wheels. In this way, both the satellite momentum and reaction wheels' momentum are reduced through PPT ignitions.:

$$\boldsymbol{\tau} = -k_{des} \boldsymbol{h}_b^i$$
$$\boldsymbol{h}_b^i = J \boldsymbol{\omega}_b^i + A J_w \boldsymbol{\omega}_w^b \tag{5.35}$$

5.7 Hardware commands

In this module, the calculated control torques are converted into commands to operate the RW and PPT unit. In the following sections, the distribution of the control torques is described.

5.7.1 Reaction wheels control command

As shown in equation (4.23), the torque due to the spinning of the reaction wheels is obtained:

$$\boldsymbol{\tau}_{rw} = -A J_w \dot{\boldsymbol{\omega}}_w^b \tag{5.36}$$

In this case, $A = I^{3\times3}$ since the reaction wheels are aligned with the satellite axis. The control command is then computed by implementing the trapezoidal rule [42] as follows:

$$\boldsymbol{\omega}_{w,k}^{b} = \int_{k-1}^{k} \dot{\boldsymbol{\omega}}_{w}^{b} dt \cong \frac{\dot{\boldsymbol{\omega}}_{w,k}^{b} + \dot{\boldsymbol{\omega}}_{w,k-1}^{b}}{2} \Delta t + \boldsymbol{\omega}_{w,k-1}^{b}$$
$$\dot{\boldsymbol{\omega}}_{w,k}^{b} = -J_{w}^{-1}\boldsymbol{\tau}_{rw} \tag{5.37}$$

5.7.2 PPT control command

Considering the position of each head of the PPT unit, the ignitions induces a torque to the satellite body (Figure 5.9); therefore, the distribution of the control torque, as defined in equation (5.35), is done by taking the sign of each element of the vector $\boldsymbol{\tau}$ and the corresponding PPT head will be enabled to produce controlled ignitions. This strategy is illustrated in the next table.

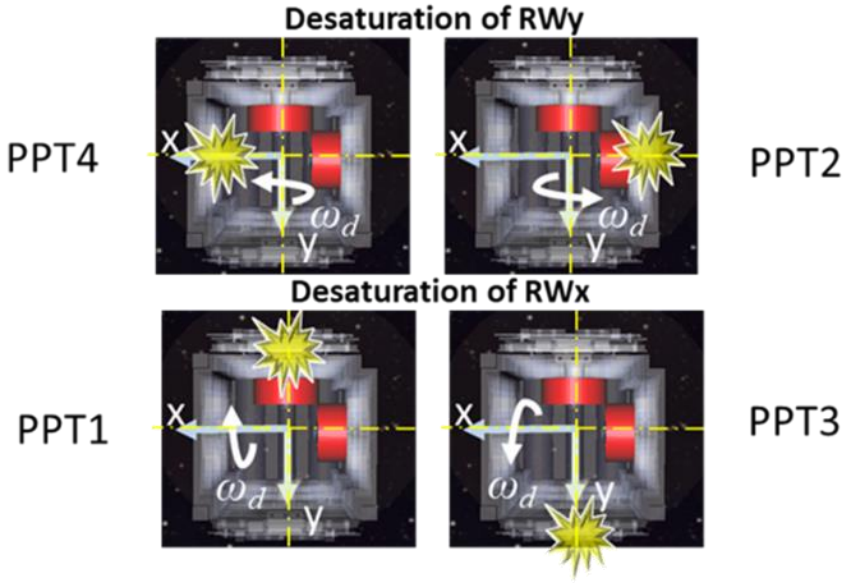

Figure 5.9 Strategy implemented for the desaturation of the reaction wheels

Table 5.15 Activation of PPT ignitions according to the sign of the control torque

τ Index	sign	PPT head index
x	+	1
	-	3
y	+	4
	-	2

5.8 Outputs

The closure of this chapter is done by listing the output data from AOCS software:

- Reaction wheels command (speed and direction, section 5.7.1)
- PPT command (Ignitions strategy, section 5.7.2 and frequency, section 5.2.10)
- Horizon flag (section 5.4.4)
- TLE received acknowledgement flag (section 5.4.1)
- FDIR status (section 5.3.4)
- AOCS current mode of operation (section 5.3.4)
- Calculated sun vector (section 5.3.1)
- EKF parameters (estimated attitude, corrected angular rates and error between real and estimated sun vector, section 5.5)
- Satellite position in ECI frame (section 5.4.2)

CHAPTER 6. LUNAR ORBIT LIFETIME ANALYSIS

This chapter is dedicated to the mission lifetime analysis of a spacecraft orbiting the Moon that was performed as part of the mission analysis of the lunar orbit precursor mission, AV4.

6.1 Introduction

The future lunar mission, referred as AV5, which is a concept CubeSat mission, is conceived to orbit the Moon at 100km altitude in a circular orbit. However, the Moon possesses an irregular gravity field that can shorten the mission lifetime of any spacecraft orbiting the Moon, particularly those which orbit the Moon in low altitudes. To illustrate this, the next figure shows the lunar gravity field model from the Gravity Recovery and Interior Laboratory (GRAIL) mission, where high concentrations of mass (mascons) can be noticed [52]:

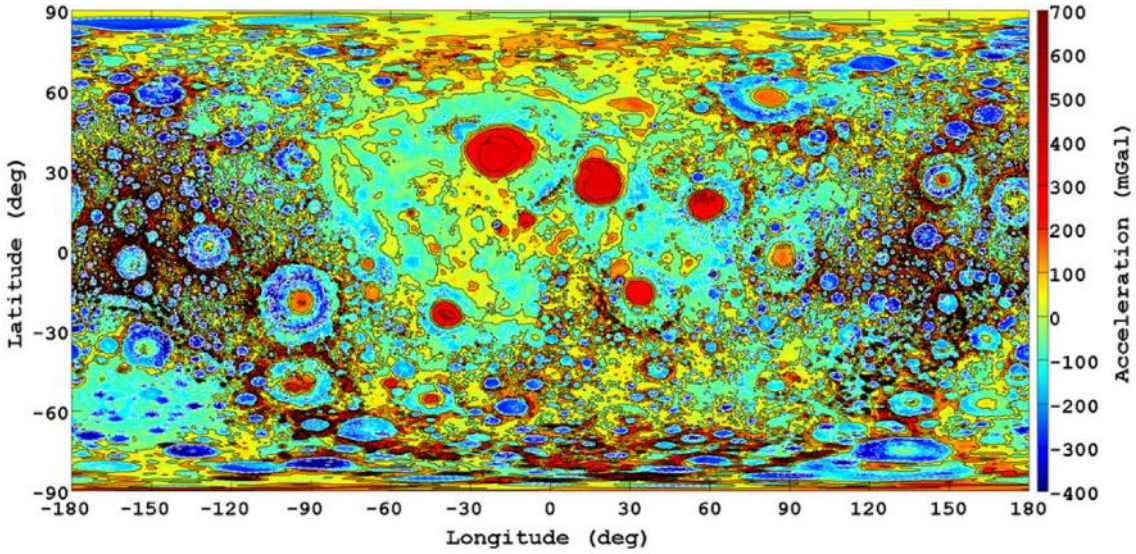

Figure 6.1 The JPL lunar gravity field. Image from Alex S. Konopliv et.al. 2013

The lunar mission lifetime is restricted by the initial orbital ephemeris, particularly the inclination, right ascension of the ascending node (RAAN), periapsis and altitude, where zonal and tesseral harmonics of Earth gravity field plays an important role [32]. Nowadays, better spherical harmonic resolutions of the lunar gravity potential model are available after the measurements obtained by Clementine, Lunar Prospector Discovery,

SELENE and GRAIL missions to perform mission analysis in lunar orbit [52]. Nonetheless, frozen orbits, defined as non-impact orbits, featuring a quasi-periodic behavior in the three-dimensional space [53] and where one or more orbital parameters are held constant, are the best option for a long-term mission, which are restricted to the distribution of lunar mascons and Earth-Moon geometry perturbations [54].

Since CubeSats are usually deployed via piggyback on larger missions, their insertion into a frozen orbit is not guaranteed and thus the utilization of propulsion systems becomes mandatory. Furthermore, their usage in the attitude control system with the reaction wheels is convenient for momentum dumping maneuvers [55]. Due to their high specific impulse (> 500s), relative low power consumption (< 10W), dimensions (< 0.5U) and less regulations on hazardous materials, a PPT unit is considered in this analysis.

6.2 Orbital lifetime analysis

The natural orbit lifetime of a spacecraft (Figure 6.2) was obtained by solving the equation (4.21) in MATLAB-Simulink via variable-step (60 seconds minimum step), fourth-order Runge-Kutta solver. In addition, the epoch time was considered as 2018-1-1 00:00:00 in our simulations. To show the influence of the initial RAAN, the natural orbit lifetime for values of zero, 90, 180 and 270 degrees was plotted. And 100km initial altitude orbit with zero as argument of perigee and eccentricity zero was set as initial orbital parameters for all the iterations. Regarding the spacecraft parameters, a spacecraft with a mass of 2.8kg (2U CubeSat), 4.57x10-6 N/m^2 as solar radiation pressure, c_r=1 as reflectivity (black body) and 0.02m^2 as area exposed to the Sun was considered.

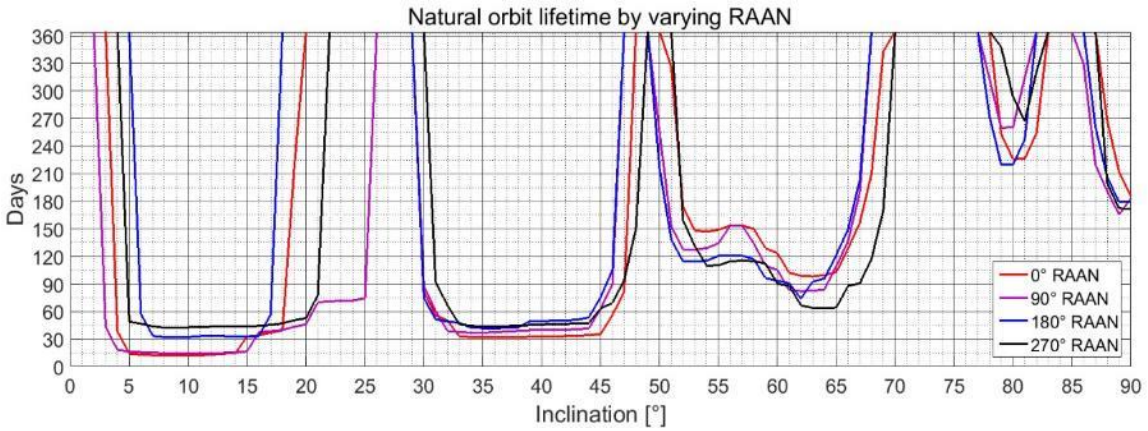

Figure 6.2 The natural orbit lifetime of a spacecraft orbiting the Moon at 100km altitude circular orbit

It can be noticed that there are several ranges of initial inclinations where the orbit lifetime can be very short and others where long-term mission can be achieved; moreover, the initial value of RAAN plays an important role in orbit lifetime. In Table 6.1, the unstable regions (UR) are classified according to the range of initial inclination values. In previous research performed by Gupta [32], Dono [56] and Zeile [57], similar UR profiles in lunar orbit lifetime are presented.

Table 6.1 Classification of lunar orbit unstable regions by ranges of initial inclination and values of RAAN of a 100km altitude circular orbit

	0° RAAN	**90° RAAN**	**180° RAAN**	**270° RAAN**
UR1	$3° < i < 20°$	$2° < i < 26°$	$5° < i < 18°$	$4° < i < 22°$
UR2	$29° < i < 48°$	$29° < i < 47°$	$29° < i < 47°$	$30° < i < 49°$
UR3	$50° < i < 70°$	$49° < i < 68°$	$49° < i < 68°$	$51° < i < 70°$
UR4	$78° < i < 83°$	$77° < i < 82°$	$77° < i < 82°$	$78° < i < 83°$
UR5	$i > 87°$	$i > 85°$	$i > 86°$	$i > 87°$

6.3 Orbit correction strategy and resulting orbit lifetime

Regarding the orbit control strategy, we have considered the calculation of optimal in-plane thrust vectors for each target orbital parameter, whose performance relies on the tuning of priority weighing factors, which are assigned to each orbital parameter to be corrected (the control algorithms are described in section 5.4.3). It is also assumed that full knowledge of a spacecraft's orbit ephemeris is required prior to the calculation of the thrust vectors by a

ground station network. Previous lunar missions such as the Small Missions for Advanced Research in Technology −1 (SMART-1) launched by the European Space Agency (ESA), the Kaguya mission by the Japan Aerospace Exploration Agency (JAXA), the Chandrayaan-1 mission by the Indian Space Research Organization (ISRO), and the Chang'E missions by the China National Space Administration (CNSA) performed orbit determination routines supported by a regional ground station network and a foreign network, such as the Deep Space Network (DSN) from the National Aeronautics and Space Administration (NASA) in the United States and the ESA tracking station (ESTRACK) at the European Space Operations Center (ESOC) [58]. Recently, Kim [59] analyzed the orbit determination precision and accuracy of lunar orbiters by examining the influence of several lunar gravity models selected for this purpose, considering the Korea Pathfinder Lunar Orbiter (KPLO) mission as a study case, which was launched in 2016, orbiting at a 100-km altitude in a lunar polar orbit and supported by three DSN antennas and one Korea Deep Space Antenna, concluding that GRAIL-based models (GRAIL420A and GRAIL660B) demonstrate the best orbit accuracy.

6.3.1 Reference coordinate system

In Figure 6.3, the proposed reference coordinate system allows the alignment of the spacecraft with the thrust vector, while the spacecraft' solar paddles normal vector is aligned with the Sun path. In this way, solar paddles collect the solar energy optimally. In section 4.2.3, the calculation of this reference frame is mentioned.

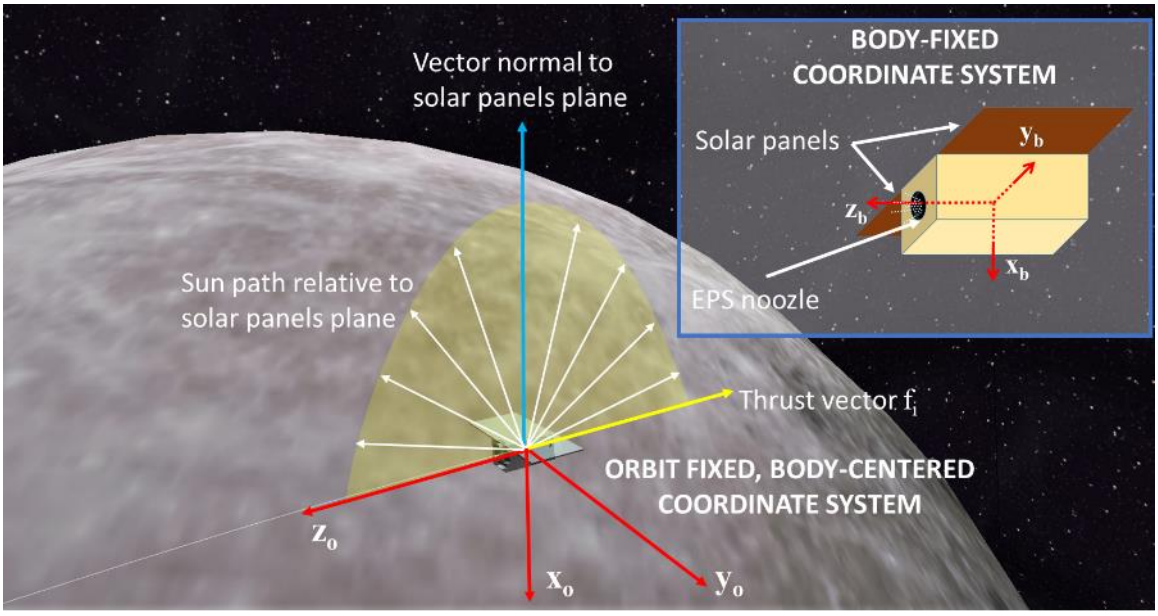

Figure 6.3 Proposed coordinate system for the execution of orbit correction maneuvers

6.3.2 Power subsystem requirements

As suggested in Figure 6.3, CubeSats should possess deployable solar panels to support the orbit correction maneuvers through EPS ignitions. Based on the research performed by Lemmer [1] and Aoba-VELOX IV CubeSat as a study case [55], the utilization of an PPT unit on a 2U CubeSat as EPS is envisaged, which possesses a 0.5U as dimensions, 2.25W as its average power and a range of 10-60μNs as I_{bit} for this analysis. By assuming the usage of solar cells with 29.5% efficiency [60], an 80% boost conversion efficiency, and 80% tracking efficiency, the area that the solar paddles should possess in order to gather solar energy while performing orbit correction maneuvers in the Sun phase was sized.

Through numerical simulations, considering a 100km altitude circular orbit, with 65 degrees as inclination, zero degrees as argument of periapsis and a set of different values of local time of descending node (LTDN) as shown in Table 6.2, it is concluded that two pairs of deployable panels are required as minimum surface (4x20x10cm) to allocate solar cells, in order to keep more than 70% state of charge (SoC) per orbit for other CubeSat subsystems. In this way, a total of 20 solar cells can be installed on one side of the CubeSat: four solar cells on each panel and four solar cells on one face of the

CubeSat body, where deployable solar paddles will be fixed. The usage of a PPT with a power consumption above 2.25 W leads to an increment of deployable solar paddles or the enlargement of the CubeSat size from 2U to 3U.

Table 6.2 also shows that the average energy collection from solar paddles increases as the LTDN value decreases below 12:00 hrs, because the Sun phase duration becomes longer and the PPT orbit correction period is extended. Therefore, according to the resulting PPT load per orbit and the percentage of the remaining energy per orbit, longer periods of orbit correction maneuvers represent an increase of power consumption along with an increase in energy collection.

Table 6.2 Power consumption analysis for a <2.25W EPS

LTDN [hrs]	Energy collected from solar paddles [Wh/orbit]	Energy stored to batteries [Wh/orbit]	PPT load [Wh/orbit]	% SoC per orbit [%]
12:00	14.02	8.97	2.68	70
11:00	15.38	9.84	2.69	73
10:00	17.87	11.43	2.72	76
9:00	21.01	13.44	2.82	79

6.3.3 Resulting extension of orbital lifetime

This section is dedicated to the analysis of the resulting extension of orbital lifetime of a lunar CubeSat mission while performing orbit correction maneuvers. The orbit control strategy is described in section 5.4.3.

An initial 100-km altitude circular lunar orbit with different inclination values, ΔV, and I_{bit} was considered. In order to show the dependence of the RAAN on the performance of the orbit correction strategy, we consider the case of 0º and 90º as initial RAAN, which is close to 23:00 hrs and 5:00 hrs LTDN, respectively, at the initial date 2018/01/01 00:00 hrs. The orbit control parameters that we fixed for all iterations are shown in Table 6.3. When the spacecraft reaches the surface-collision condition (zero altitude), the simulation stops.

Table 6.3 Orbit control parameters for the orbit control strategy

orbit control parameter	Value
Eccentricity	
op_r	0
$t_{op,min}$	0.016
$t_{op,max}$	0.022
w_{op}	1
Semimajor axis	
op_r	1738.1+110 km
$t_{op,min}$	15 km
$t_{op,max}$	20 km
w_{op}	0.2

Figure 6.4 and Figure 6.5 show the performance of the orbit correction strategy on the enhancement of the mission lifetime for a set of ΔV values, which have a close relationship with the available propellant of the EPS. As we discussed in section 6.3.2, we consider a PPT unit as the EPS by fixing its I_{bit} value at an average value of 25 μNs.

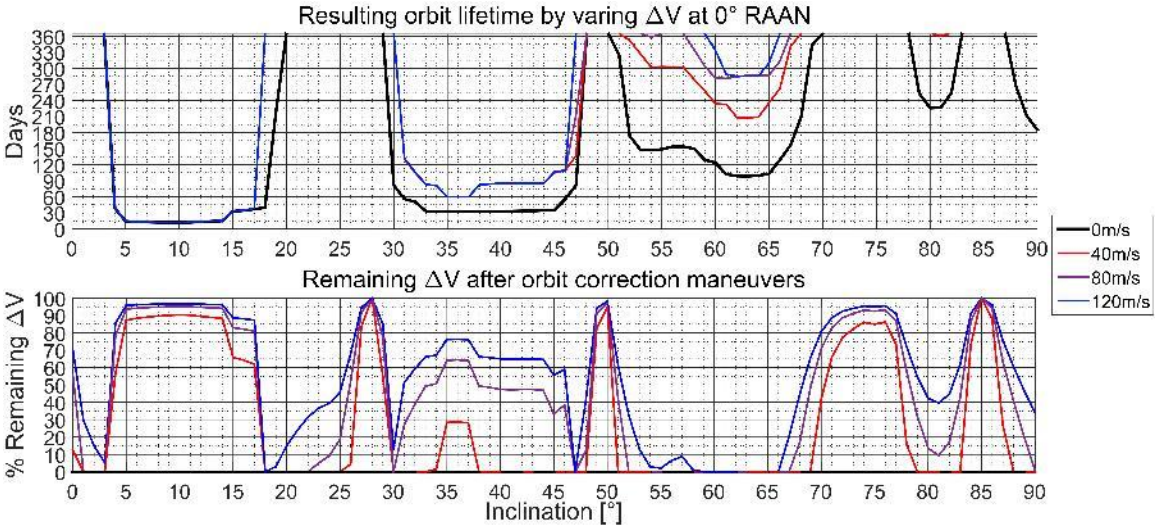

Figure 6.4 Extension of the lunar orbit lifetime by varying the ΔV of the propulsion system at initial 0º RAAN

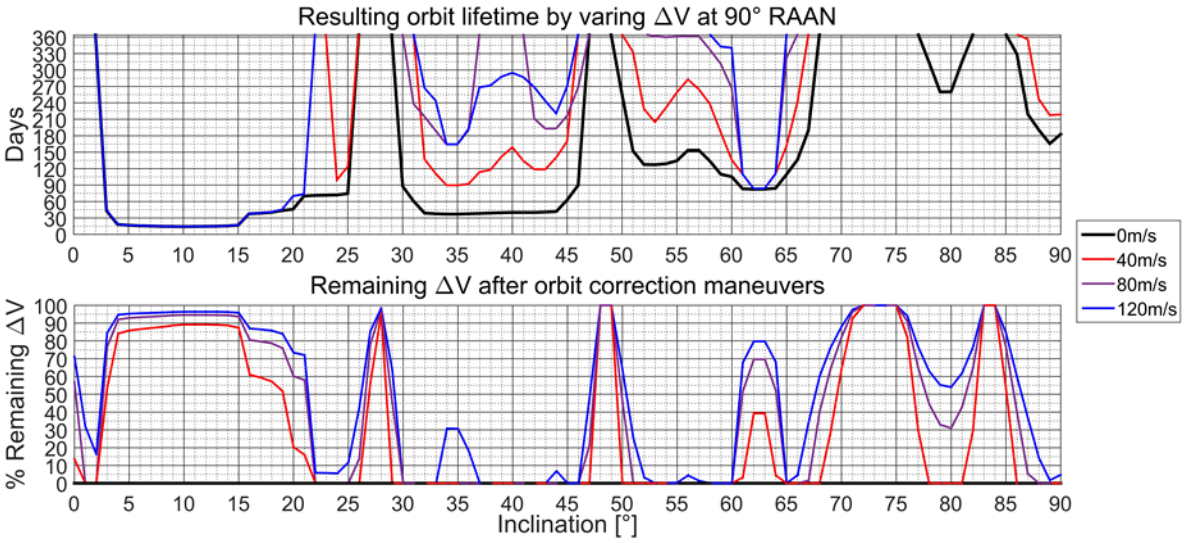

Figure 6.5 Extension of the lunar orbit lifetime by varying the ΔV of the propulsion system at initial 90º RAAN

According to each unstable region (UR), as defined in Table 6.1, we analyze the results reported in Figure 6.4 and Figure 6.5, as follows:

UR1: A very small improvement on the mission lifetime could be achieved. In both Figure 6.4 and Figure 6.5, our orbit correction strategy enhances the mission lifetime for initial inclination values above 17º, where unstable regions are reduced by up to 2º (Figure 6.4) and 4º (Figure 6.5).

UR2: In Figure 6.5, the implementation of our orbit control strategy resulted in a greater increase in mission lifetime for a ΔV greater than 40 m/s. Better performance in the enhancement of the mission lifetime for shorter ΔV values at specific initial inclination values is noticeable. Figure 6.6 shows an example of this atypical case, where inclination and RAAN are 39º and 90º respectively. At day 160 after epoch, the ΔV value of 80m/s is reached and the spacecraft altitude varies from 50 to 225 km. From day 160 to 230, the remaining ΔV is used to mitigate the increase of the eccentricity and reduce the semimajor axis; however, this orbital maneuver resulted unfavorable and as a consequence, the inherent orbital perturbations induced an increase of the eccentricity, causing a reduction on the orbit lifetime. By either setting up a higher semimajor axis thresholds and reference values or deactivating the orbital maneuvers after reaching 80m/s, a one year-term mission can be achieved.

UR3: Successful orbit lifetime enhancement was achieved, except for a small range of initial inclination (62–63º), as shown in Figure 6.5, where orbit correction maneuvers induced an inappreciable improvement in the mission lifetime.

UR4: The orbit correction maneuvers increased the mission lifetime to greater than one year in both cases.

UR5: Notwithstanding the reduced performance of the mission lifetime by considering 40 m/s as the ΔV (Figure 6.5), the orbit correction maneuvers successfully extend the mission lifetime to greater than one year in both cases.

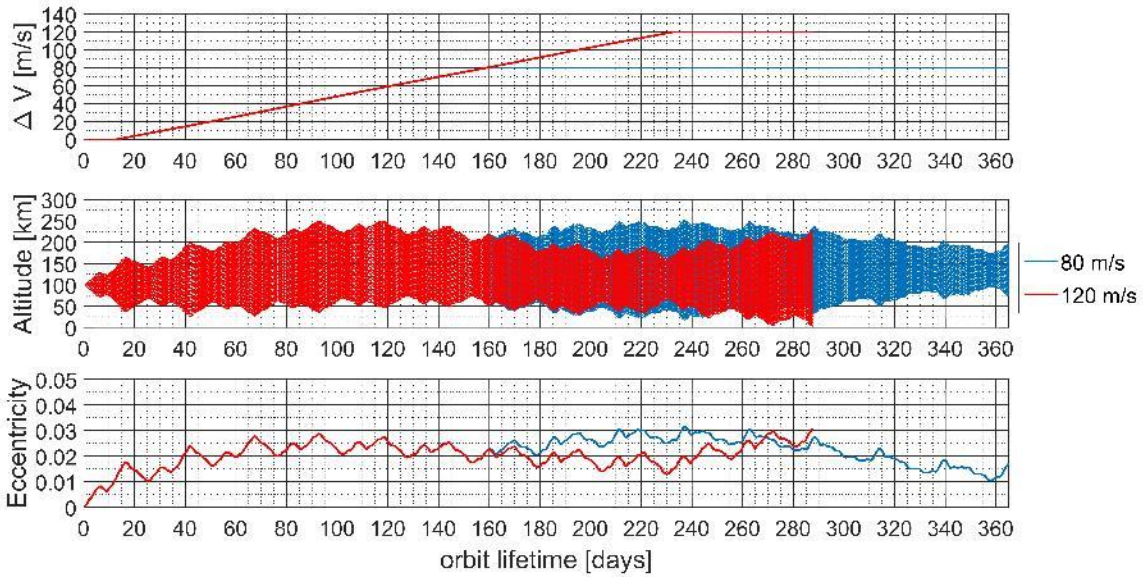

Figure 6.6. Example of an atypical simulation results at 39º inclination and 90º RAAN, considering 30 μNs Ibit constant value

Figure 6.7 and Figure 6.8 show the simulation results assuming 80 m/s as the fixed ΔV value and a varying I_{bit} value. For each unstable region (UR) in accordance with Table 6.1 below.

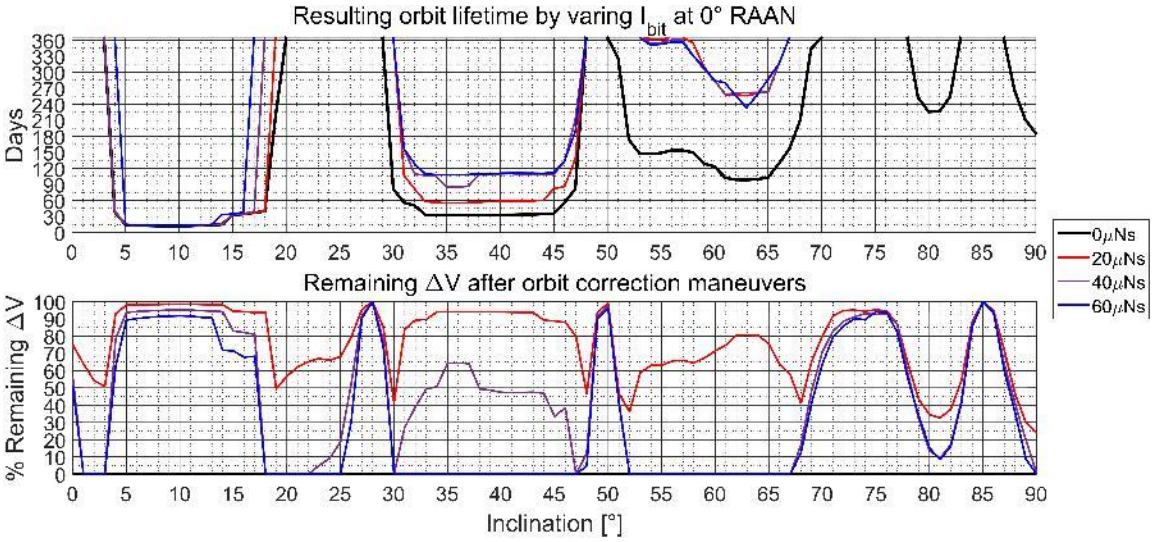

Figure 6.7 Extension of the lunar orbit lifetime by varying the I_{bit} of the propulsion system at initial 0º RAAN

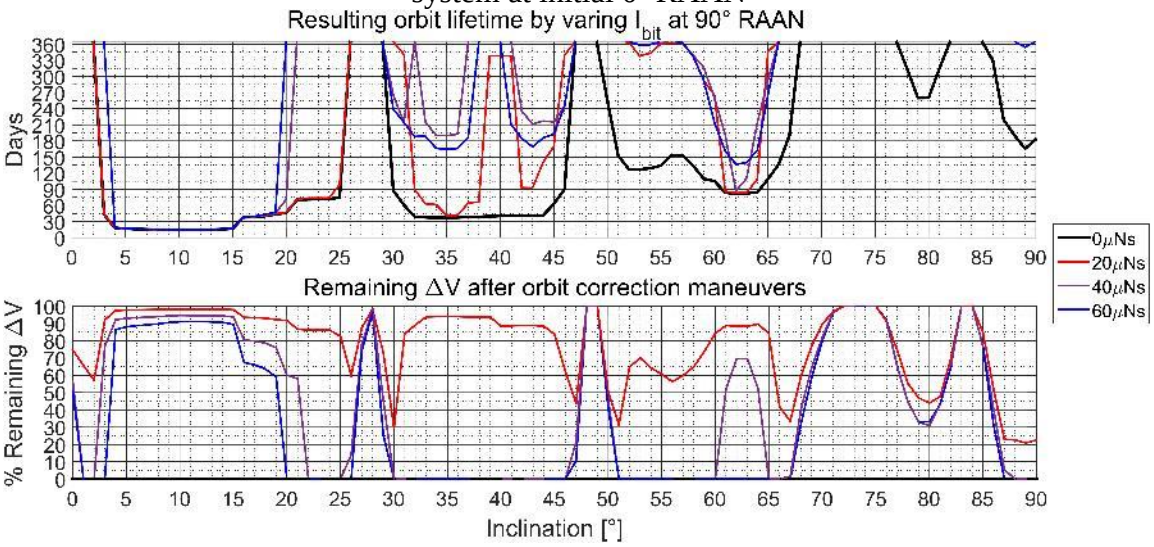

Figure 6.8 Extension of the lunar orbit lifetime analysis by varying the I_{bit} of the propulsion system at initial 90º RAAN

UR1: For a greater value of I_{bit}, the unstable regions can be reduced to a greater extent (up to -2º and -6º, as shown in Figure 6.7 and Figure 6.8, respectively); however, a slight improvement in the mission lifetime could be achieved for initial inclination values below 17º and 20º, as shown in Figure 6.7 and Figure 6.8, respectively.

UR2: Both cases show an increase in the mission lifetime; however, in Figure 6.8, diverse mission lifetime enhancement results for each I_{bit} value are also noticeable. Further improvements on those results can be obtained by fine tuning the orbit control parameters for each initial inclination value.

UR3: Successful orbit lifetime enhancement was achieved. There is also a small range of initial inclination values (62–63º) where orbit correction maneuvers provide a humble improvement in the mission lifetime, as shown in Figure 6.8. As with the UR2 results, we found minor inconsistencies in the enhancement of the mission lifetime for larger I_{bit} values; nonetheless, this anomaly can be minimized by fine tuning the orbit control parameters for each case.

UR4: The orbit correction maneuvers increased the mission lifetime to more than one year in both cases.

UR5: The orbit correction maneuvers increased the mission lifetime to more than one year in both cases.

For certain ranges of the initial inclination values within the unstable regions, the orbit correction strategy successfully increased the mission lifetime from several days to more than a year; however, most of the initial inclination values within UR1, the thrust generated by the EPS considered in this analysis was insufficient to overcome the orbital disturbances due to the irregular gravity field of the Moon. Despite this condition, the proposed orbit correction strategy enhances the orbital lifetime from days to more than one year by considering a set of ΔV and I_{bit} values for an EPS. In the following sections, the optimal values for those parameters are investigated by considering the duration of the orbit correction maneuvers throughout the mission lifetime of the spacecraft and the expected orbital altitude achieved after the resulting orbit correction maneuvers.

6.3.4 Controlling the orbital inclination

Whereas section 6.3.3 is dedicated in the analysis of the extension of the mission lifetime capabilities of a CubeSat performing in-plane orbital maneuvers to keep a 100km altitude circular orbit, this section shows the capability of a CubeSat to correct its orbital inclination. From Table 5.12, we calculated the maximum change of inclination Δi performed by a CubeSat through orbit correction maneuvers (Table 6.4), assuming specific ΔV values (e.g. from 40 to 120m/s as we considered in our simulations) at a 100km altitude lunar circular orbit, whose average orbital velocity is $V = \left\| \boldsymbol{v}_{\mathrm{M,sc}} \right\| \approx 1633\mathrm{m/s}$.

Table 6.4: Maximum Δ*i* values in 100km altitude lunar circular orbit, for a particular EPS's ΔV parameter

ΔV [m/s]	Δi [°]
40	0.89
80	1.79
120	2.68

Moreover, if we also assume a particular EPS's I_{bit} value (e.g. from 20 to 60 μNs), we can roughly estimate the depletion time of the EPS's ΔV capacity. If the weight of our CubeSat is 3kg, we can calculate the change of its orbital acceleration during one second assuming that $F = m \cdot a$, where F is the thrust force produced by the EPS, m is the spacecraft mass and a is the instantaneous acceleration of the spacecraft. From the acceleration value a, which depends on the EPS's I_{bit} value, we can estimate depletion time of the EPS's ΔV capacity $a = \Delta V/t$ (Table 6.5), assuming a continuous correction of the inclination.

Table 6.5: Estimated depletion time of the EPS's ΔV (in days) for a specific value of I_{bit}

	EPS's Δ*V* [m/s] and maximum Δ*i* value [°]		
***I*$_{bit}$ [μNs]**	**40m/s Δ*V* (Δ*i*= 0.89°)**	**80m/s Δ*V* (Δ*i*= 1.79°)**	**120m/s Δ*V* (Δ*i* = 2.68°)**
20	69 days	139 days	208 days
30	46 days	93 days	139 days
40	35 days	69 days	104 days
60	23 days	46 days	69 days

We ran several simulations to verify the rough calculations from Table 6.5, considering the initial conditions that were mentioned at the beginning of Section 4, varying the ΔV values from 40 to 120 m/s and 30 μNs as EPS's I_{bit} value. The orbit control

parameters $t_{OP,min}$ and $t_{OP,max}$ are set as 0.5° and 2° respectively. The inclination reference value was set based on the initial inclination value and its location within the URs, as shown in Figure 6.9, where the main objective is the correction of the inclination towards the closest inclination value of a stable orbit.

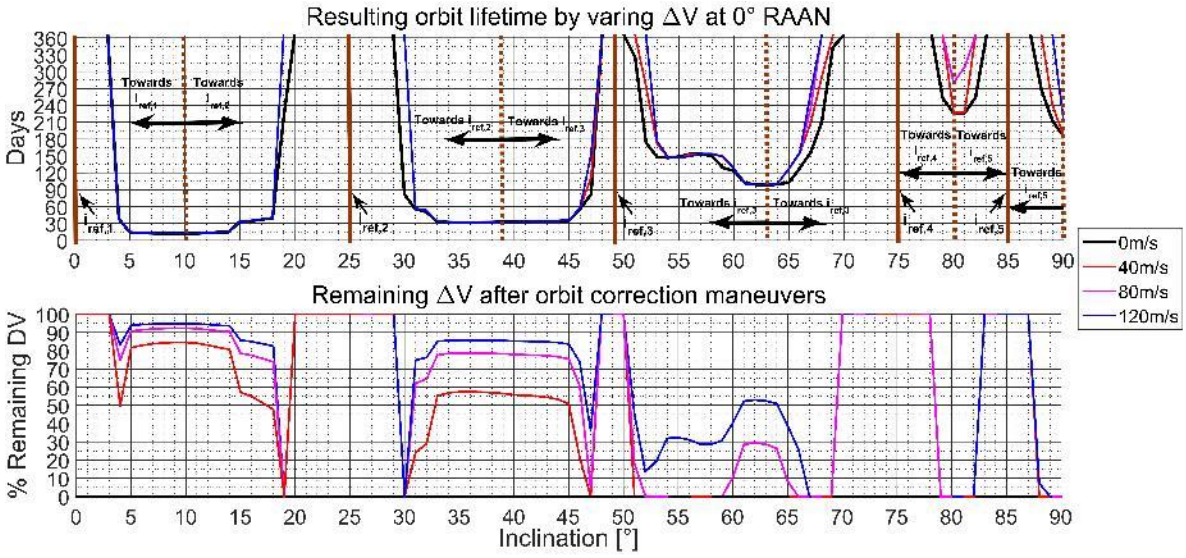

Figure 6.9: Extension of the lunar orbit lifetime by varying the Δ*V* of the propulsion system at initial 0º RAAN

From these results, we conclude that:

- The orbit lifetime inside the unstable regions UR1, UR2 and UR3 (Table 6.1) is shorter than the depletion time of the EPS's Δ*V* for the required inclination correction maneuvers; therefore, the spacecraft will not be able to complete the orbit correction maneuvers in order to leave those URs.
- The inclination correction maneuvers are limited to the inner boundaries of the unstable regions (Table 6.1), since the maximum correction of the orbital inclination is restricted to a maximum Δ*i* of 2.68°.

6.3.5 Duration of orbit maintenance maneuvers

The orbit maintenance maneuvers are executed continuously until the collision condition occurs, Δ*V* reaches its maximum value, or the set-point values of both orbital parameters are reached; however, that may lead to long-lasting maneuvers during the

mission lifetime of the CubeSats in lunar orbit, leaving time for the execution of scientific mission tasks mainly in the eclipse phase. In Figure 6.10 - Figure 6.13, we show the percentage of time utilized for orbit correction maneuvers during the Sun phase until the collision condition or a one-year orbit lifetime is achieved, where long-lasting orbit correction maneuvers take place in UR2. Additionally, the duration of the orbit correction maneuvers in UR1 is irrelevant due to the shortness of the orbit lifetime.

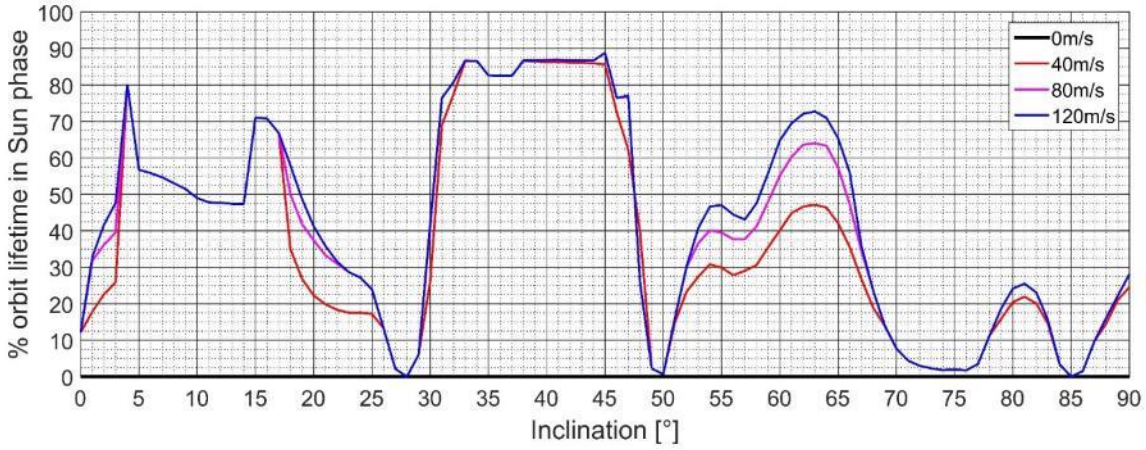

Figure 6.10 Percentage of orbit lifetime utilized for orbit correction maneuvers during Sun phase by varying ΔV at 0º RAAN

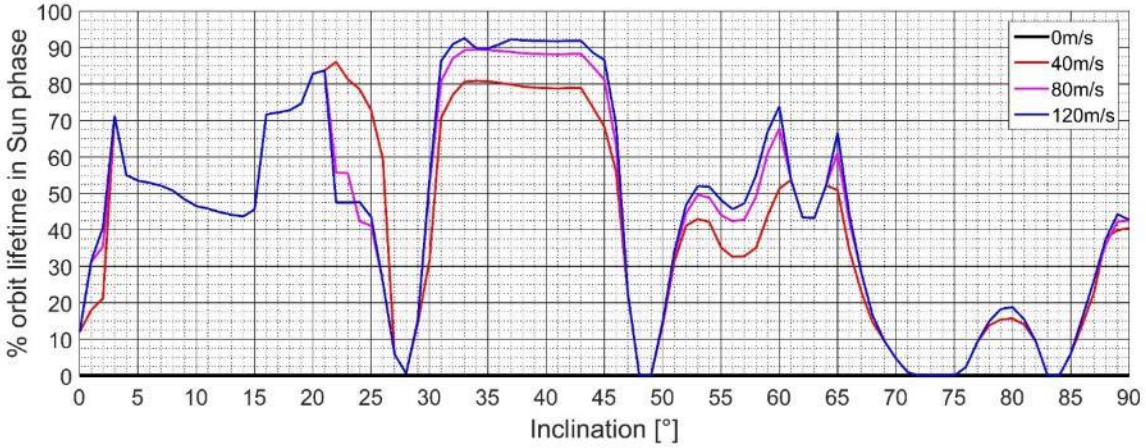

Figure 6.11 Percentage of orbit lifetime utilized for orbit correction maneuvers during Sun phase by varying the ΔV at 90º RAAN

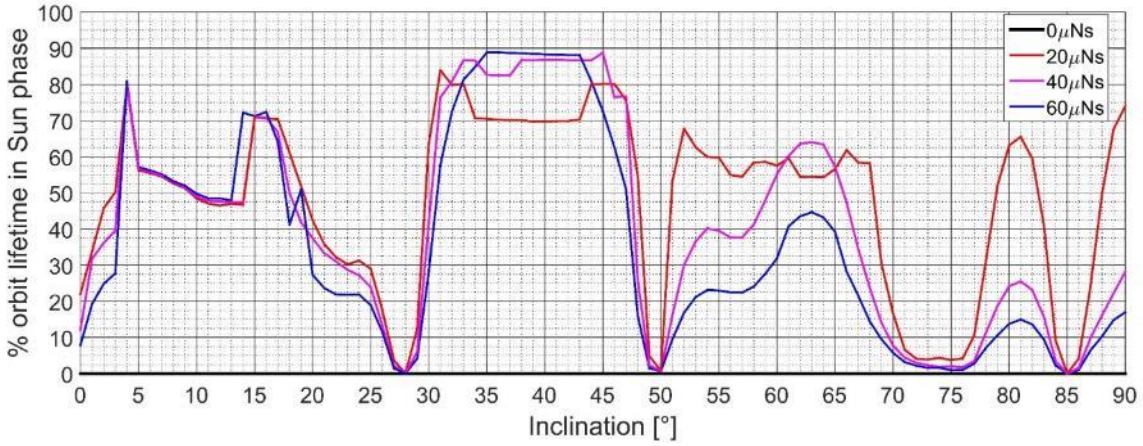

Figure 6.12 Percentage of orbit lifetime utilized for orbit correction maneuvers during Sun phase by varying I_{bit} at 0º RAAN

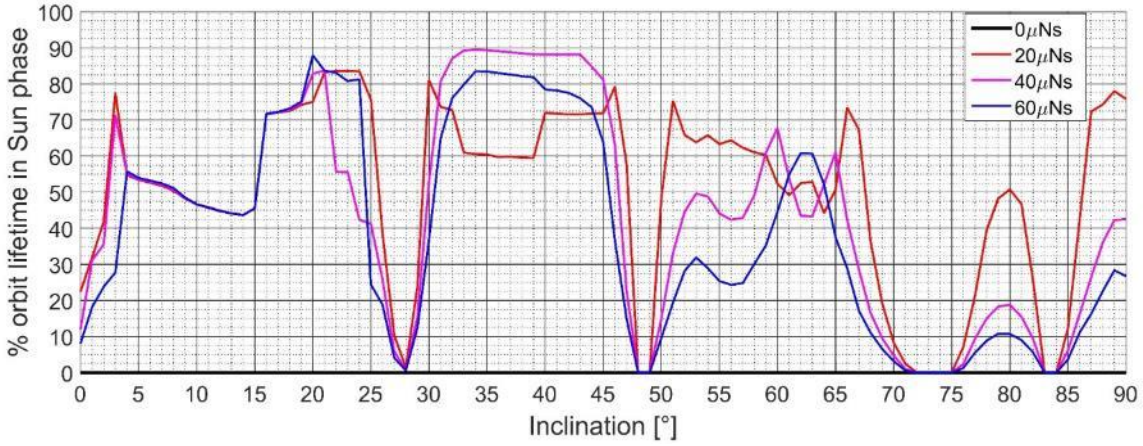

Figure 6.13 Percentage of orbit lifetime utilized for orbit correction maneuvers during Sun phase by varying I_{bit} at 90º RAAN

Regarding the orbit correction maneuvers executed in UR3, UR4 and UR5, the utilization of the mission lifetime for these maneuvers increases for larger ΔV values (Figure 6.10 and Figure 6.11). These results suggest that a longer mission lifetime is achieved at the cost of longer orbital maneuvers, particularly in UR3; however, the resulting orbit lifetime is significantly enhanced for larger ΔV values.

By comparing the results obtained in section 6.3.3, it is concluded that a noticeable enhancement of the orbit lifetime is obtained by envisaging an EPS with ΔV values above 80 m/s; however, the duration of orbit correction maneuvers in UR3, UR4 and UR5 tends to decrease as I_{bit} increases (Figure 6.12 and Figure 6.13). This suggests that the EPS ΔV parameter promptly reaches its maximum value, for a resulting orbital lifetime shorter than

one year; furthermore, the instantaneous orbital parameters quickly reach their set-point values, for a resulting orbital lifetime longer than one year. Based on those results, in terms of duration of orbit correction maneuvers, it is concluded that the optimal enhancement of the orbit lifetime can be achieved for I_{bit} values larger than 40 μNs.

6.3.6 Resulting altitude after the orbit correction maneuvers

Once reaching the EPS end-of-life by orbit correction maneuvering and successfully extending the orbit lifetime, the resulting eccentricity may be inappropriate for some scientific missions where the altitude of the spacecraft in lunar orbit is critical for the success of the mission. In Figure 6.14-Figure 6.17, we show the minimum altitude that the CubeSat reaches within one year, where it is possible to observe the natural and extended stable regions for a set of initial inclination values. In addition, our orbit control strategy improves the achieved minimum altitude by increasing the ΔV and I_{bit} values.

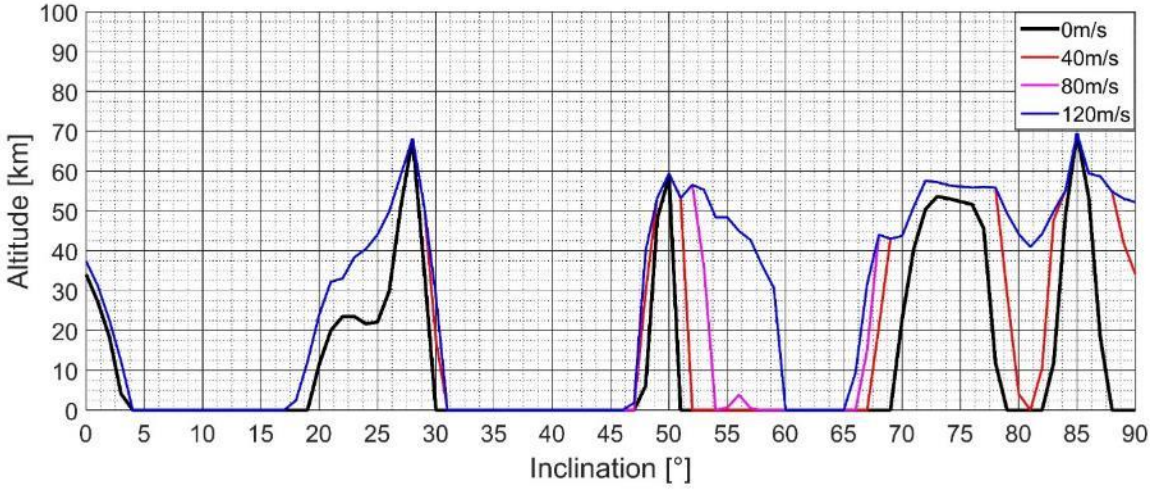

Figure 6.14 Minimum altitude achieved after one year by varying the ΔV parameter at 0º RAAN

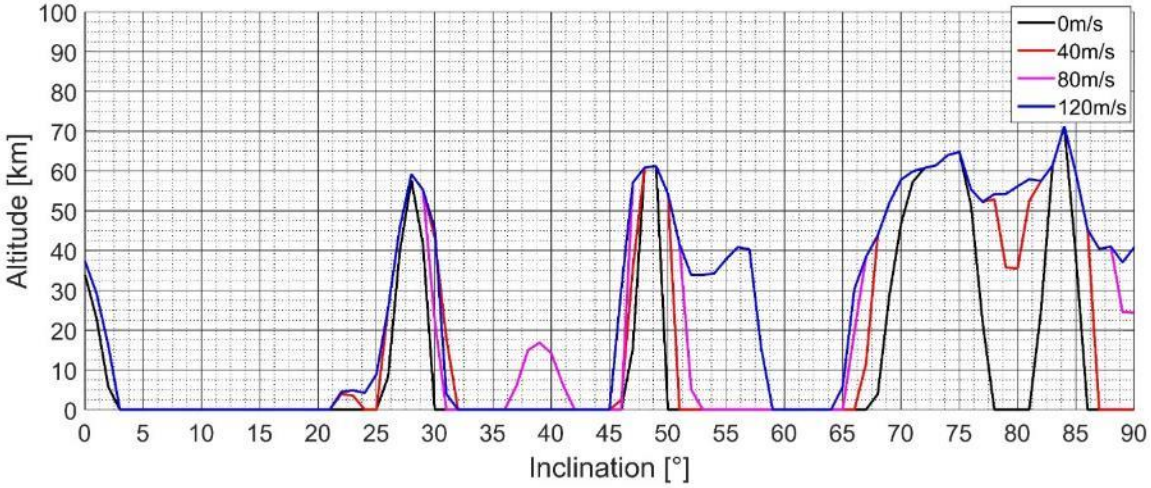

Figure 6.15 Minimum altitude achieved after one year by varying the ΔV parameter at 90º RAAN

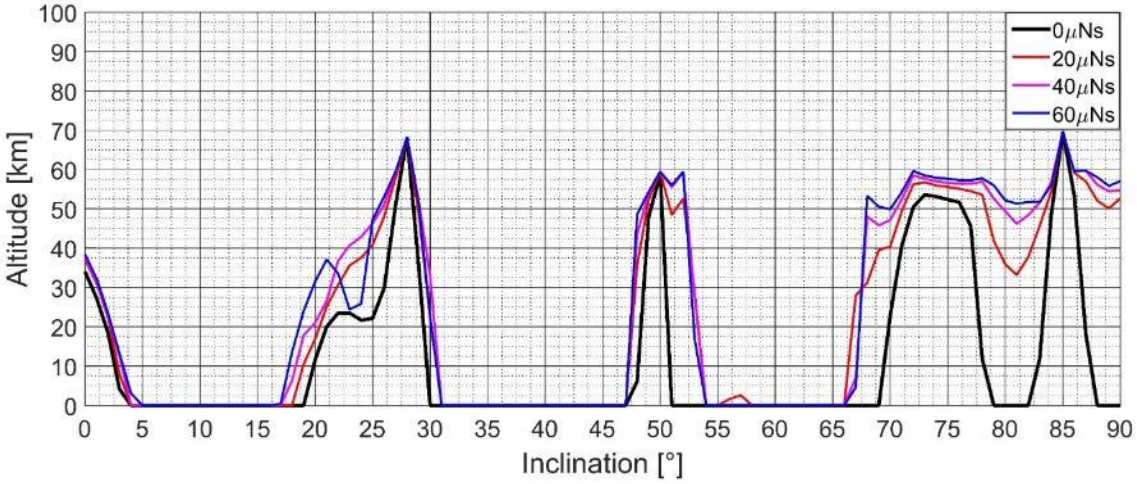

Figure 6.16 Minimum altitude achieved after one year by varying the I_{bit} parameter at 0º RAAN

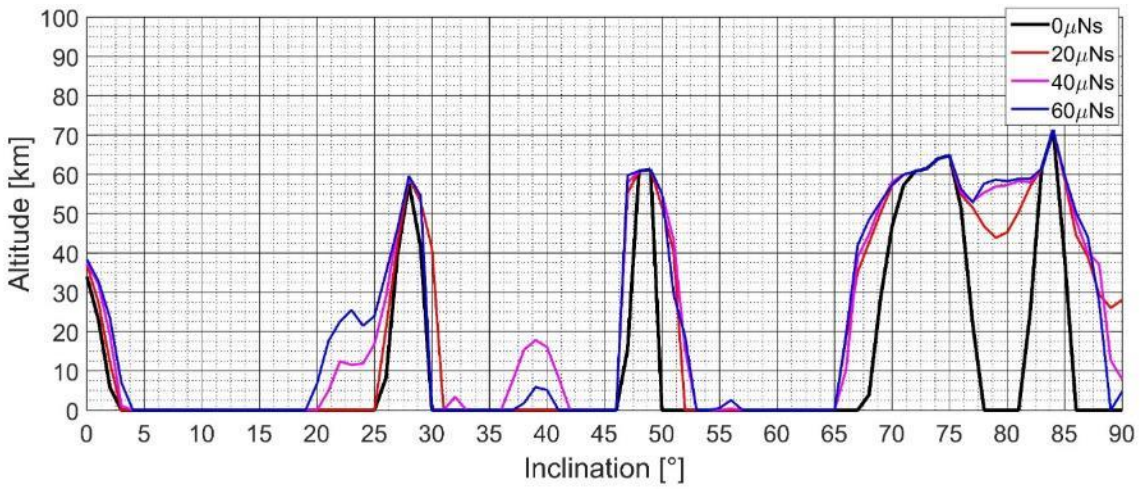

Figure 6.17 Minimum altitude achieved after one year by varying the I_{bit} parameter at 0º RAAN

CHAPTER 7. AOCS TESTING PLATFORMS

This chapter is dedicated to provide details on the development of testing platforms for the validation and verification of the AV4 AOCS software described in CHAPTER 5, as well as the results obtained through the tests campaigns. The development of the AOCS software was performed by following the system engineering V model [61] [62], where the main specifications of the system are met first and a preliminary design is developed (MATLAB model). Through rapid-prototyping (C-code generation process), the AOCS software is embedded into the microcontroller to check the functionality of the generated code. It is also possible to use real sensor and/or actuator to increase the reliability of the AOCS software within a hardware-in-the-loop based testing campaigns. The final step is the evaluation of the AOCS software embedded into the OBC firmware.

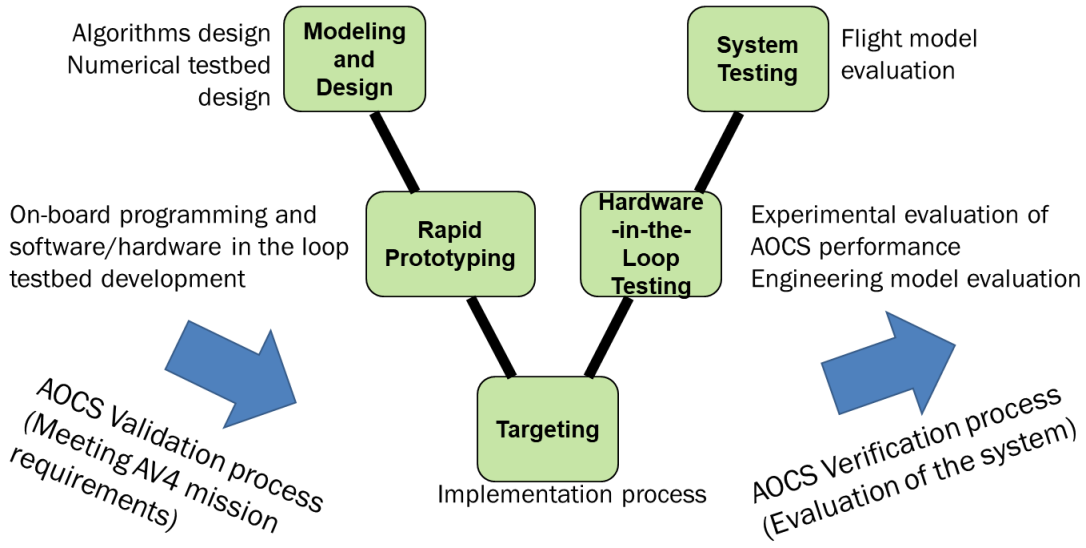

Figure 7.1 System engineering V-diagram

The content of this chapter is structured as follows:

- Software in-the-Loop (SIL) testbed
- Processor-in-the-Loop (PIL) testbed
- Hardware-in-the-Loop (HIL) testbed

7.1 Software in-the-Loop (SIL) testbed

SIL is used during the development and validation tasks of AOCS algorithms. A MATLAB-based simulation environment is used to emulate the AV4 sensor information and control torques and forces from either AV4 actuators and the space environment. In Figure 7.2, an illustration of this testbed is shown, where it can be identified four modules:

- Actuators
- Dynamics
- Sensors
- AOCS (CHAPTER 5)

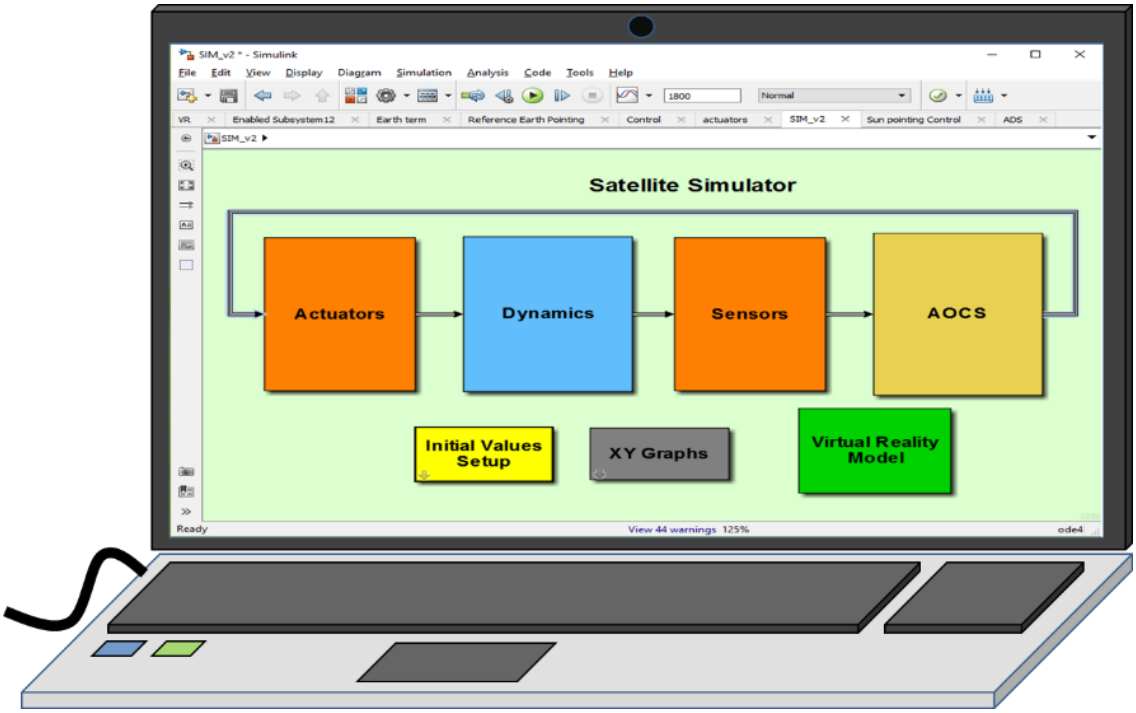

Figure 7.2 Software-in-the-loop testbed

7.1.1 Actuators module

The actuators' module contains the models of the reaction wheels and PPT. Its inputs come from the AOCS control commands (section 5.8) and its outputs are the control torques and acceleration forces from PPT.

The reaction wheels utilized on the AV4 satellite consist on a flywheel mounted on a DC motor (section 3.1.1). The mechanical and electrical model of the reaction wheel is shown as follows [63]:

$$\begin{aligned} v_{rw} &= R_m i_m + K_s \omega_{rw} \\ \tau_{rw} &= J_{rw} \dot{\omega}_{rw} = K_t i_m \end{aligned} \tag{7.1}$$

where v_{rw}, i_m and R_m are the armature voltage, current or the motor and resistance of the coils respectively and K_s and K_t are the speed and torque constants. The speed of the reaction wheels is controlled by PID control scheme, where its gain values were tuned in order to obtain stability of the model for different speed commands.

Regarding the PPT model, the torque and acceleration produced by each ignition is modeled considering the position of each head from the center of mass, as well as its featuring I_{bit}. According to the placement of each PPT igniter into AV4 satellite, it is possible to identify the translational and rotational components (Figure 7.3) [64].

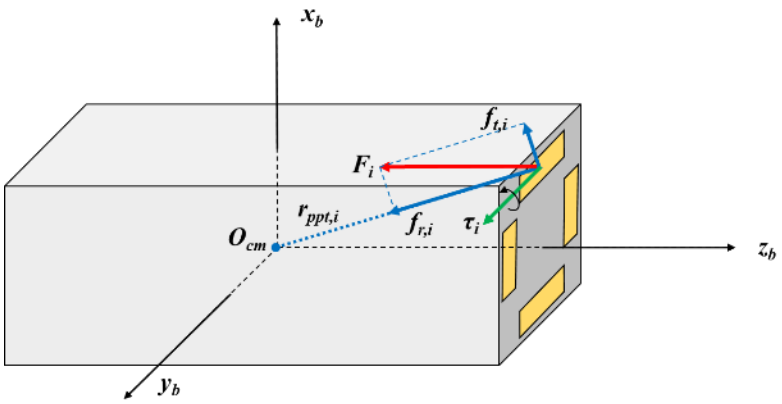

Figure 7.3 Reaction forces per PPT ignition

The calculation of each force induced to the satellite due to PPT ignitions within a period of t_{bit} is shown below:

$$\boldsymbol{f} = \frac{I_{bit}}{t_{bit}} \sum_{i=1}^{4} \frac{(\boldsymbol{r}_{ppt,i} \cdot \boldsymbol{F}_i)\boldsymbol{r}_{ppt,i}}{\left(\|\boldsymbol{r}_{ppt,i}\|\right)^2} = \frac{I_{bit}}{t_{bit}} \sum_{i=1}^{4} \boldsymbol{f}_{r,\,i}$$
$$\boldsymbol{\tau} = \frac{I_{bit}}{t_{bit}} \sum_{i=1}^{4} \boldsymbol{r}_{ppt,i} \times \boldsymbol{f}_{t,\,i} \tag{7.2}$$

7.1.2 Dynamics module

This module contains the differential equations related with the time (section 4.1) orbital mechanics (section 4.4), space disturbances (section 4.7) and attitude dynamics (section 4.5 and 4.6). Its inputs are the control torques and acceleration from the actuators module. Its outputs are the satellite attitude, angular rates, position and velocity; as well as the time and sun position.

7.1.3 Sensor module

This module contains the sensor models (Gyroscope and sun sensors) and the algorithms for the calculation of the simulated TLE.

The simulated gyroscope data is calculated as follows [35]:

$$\boldsymbol{\omega}_{gyro} = \boldsymbol{\omega}_b^i + \boldsymbol{b} + \boldsymbol{v}(t) \tag{7.3}$$

where $\boldsymbol{b} = [b_x \quad b_y \quad b_z]^\top$ is the bias of each axis of the gyroscope and $\boldsymbol{v}(t)$ is a random process whose magnitude is related to the sensitivity of the gyroscope.

The sun sensors data is simulated by taking the sun vector in inertial frame and the attitude of the satellite, as well as its maximum current i_{max}. Since AV4 satellite possess 6 coarse sun sensors allocated on each of its faces, a matrix A which contains the position of each sensor is included, as shown below [35]:

$$\boldsymbol{s_{ss}} = i_{max} A\left[R(\mathbf{q}_b^i)\right]^{\top} \boldsymbol{s}_i + \boldsymbol{v}(t)$$
$$A = \begin{bmatrix} 1 & 0 & 0 \\ -1 & 0 & 0 \\ 0 & 1 & 0 \\ 0 & -1 & 0 \\ 0 & 0 & 1 \\ 0 & 0 & -1 \end{bmatrix} \tag{7.4}$$

The simulated TLE data is calculated when the satellite position r_{sc} is in the line of sight of a ground station r_{ob}. This event can be determined by considering a fixed value of an elevation (e.g. above 10°) relative to this ground station located on any point of the Earth surface in terms of latitude φ_{lat} and longitude θ_{lon}. The elevation $elev$ can be calculated as follows [28]:

$$elev = \text{asin}(r_{th,z})$$
$$\boldsymbol{r}_{th} = [r_{th,x} \quad r_{th,y} \quad r_{th,z}]^{\top} = R_{ECEF}^{TH}(\boldsymbol{r}_{sc} - \boldsymbol{r}_{ob})$$
$$R_{ECEF}^{TH} = \begin{bmatrix} -\sin\theta_{lon} & \cos\theta_{lon} & 0 \\ -\sin\varphi_{lat}\cos\theta_{lon} & -\sin\varphi_{lat}\sin\theta_{lon} & \cos\varphi_{lat} \\ \cos\varphi_{lat}\cos\theta_{lon} & \cos\varphi_{lat}\sin\theta_{lon} & \sin\varphi_{lat} \end{bmatrix} \tag{7.5}$$

The calculation process of the satellite's orbital ephemeris utilized to build up the simulated TLE data $[RAAN, i, \omega, e, M, n]$ is summarized below [28]:

Table 7.1 Calculation process of the satellite's orbital parameters from its position and velocity

Parameter	**Algorithm**
n	$n = \frac{86400}{2\pi}\sqrt{\frac{\mu_E}{a^3}}$
	$a = \frac{\mu_E}{2\left(\frac{\mu_E}{\|\boldsymbol{r}_{sc}\|} - \frac{\|\boldsymbol{v}_{sc}\|^2}{2}\right)}$
i	$i = \cos\frac{h_z}{\|\boldsymbol{h}\|}$
	$\boldsymbol{h} = \boldsymbol{r}_{sc} \times \boldsymbol{v}_{sc}$
$RAAN$	$RAAN = \text{atan2}\left(-\frac{h_x}{h_y}\right)$

e

$$e = \sqrt{1 - \frac{\|\boldsymbol{h}\|^2}{a\mu_E}}$$

M

$$M = (\Phi - e \sin \Phi)$$

$$\sin \Phi = \frac{\boldsymbol{r}_{sc} \cdot \boldsymbol{v}_{sc}}{e\sqrt{a\mu_E}}$$

$$\cos \Phi = \frac{a - \|\boldsymbol{r}_{sc}\|}{ae}$$

ω

$$\omega = \operatorname{atan2}\left(\frac{\frac{\boldsymbol{r}_{sc,z}}{\sin i}}{\boldsymbol{r}_{sc,x} \cos RAAN + \boldsymbol{r}_{sc,y} \sin RAAN} \right) - v$$

$$v = 2 \operatorname{atan}\left(\tan \frac{\Phi}{2} \sqrt{\frac{1+e}{1-e}} \right)$$

7.1.4 Operation of the SIL testing platform

Once the flight simulator is set up, the AOCS module developed for AV4 satellite is programmed and tested by using simulated sensor signals and user commands, as if a ground station was sending commands to the satellite. In Figure 7.4. User interface to send commands to AOCS moduleFigure 7.4, the appearance of that user inter interface is shown. The control switches serve to update the AOCS inputs (as described in section 5.2) during the execution of the simulator.

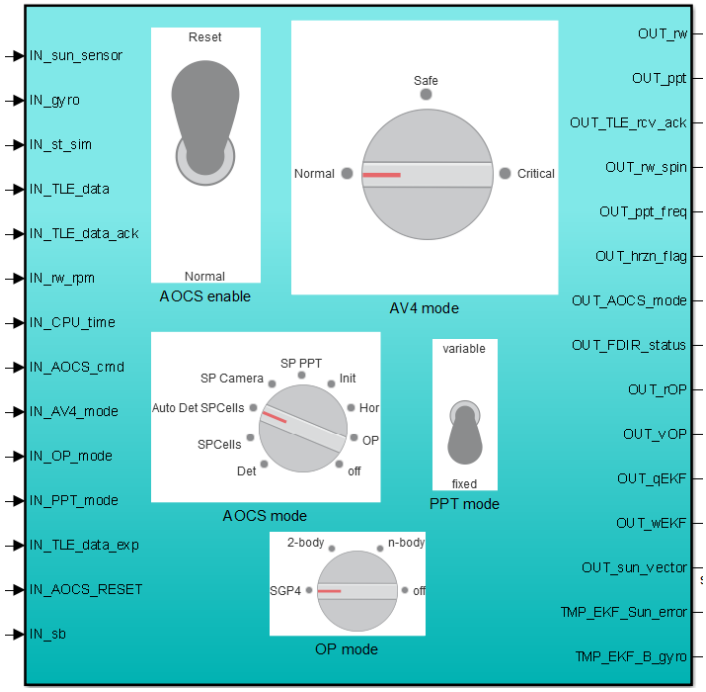

Figure 7.4. User interface to send commands to AOCS module

The outcoming data from AOCS module can be supervised during each run through 2D graphs. It is also possible to save the simulation data, including inputs, for further analysis.

In this way, it is possible to validate the elements of AOCS module dedicated for AV4 in order to meet its mission requirements.

The Figure 7.5 shows an example of the data that was gathered during one simulation run, including, angular rates, the calculated sun vector, PPT ignitions counter, reaction wheel speed, orbit propagator error, and satellite error angle. In this example, we validated one feature of the FDIR element, which is the change among modes of operations. In this graph, it is possible to observe the variation of the Sun vector when the AOCS mode was change from Initialization mode (Sun tracking), to Horizon and Orbit maintenance mode. The targeted attitude for this simulation case was aligning the +x axis towards the Sun ([0,0,1]). Also, it is possible to notice that the magnitude of the angular rate of satellite remained close to zero. However, Since this simulation run was executed in early stages of the project, it is possible to notice that improvements in orbit propagator and attitude determination routines required improvement (orbit propagator error reached 50km error and attitude error angle was large during horizon and orbit maintenance mode).

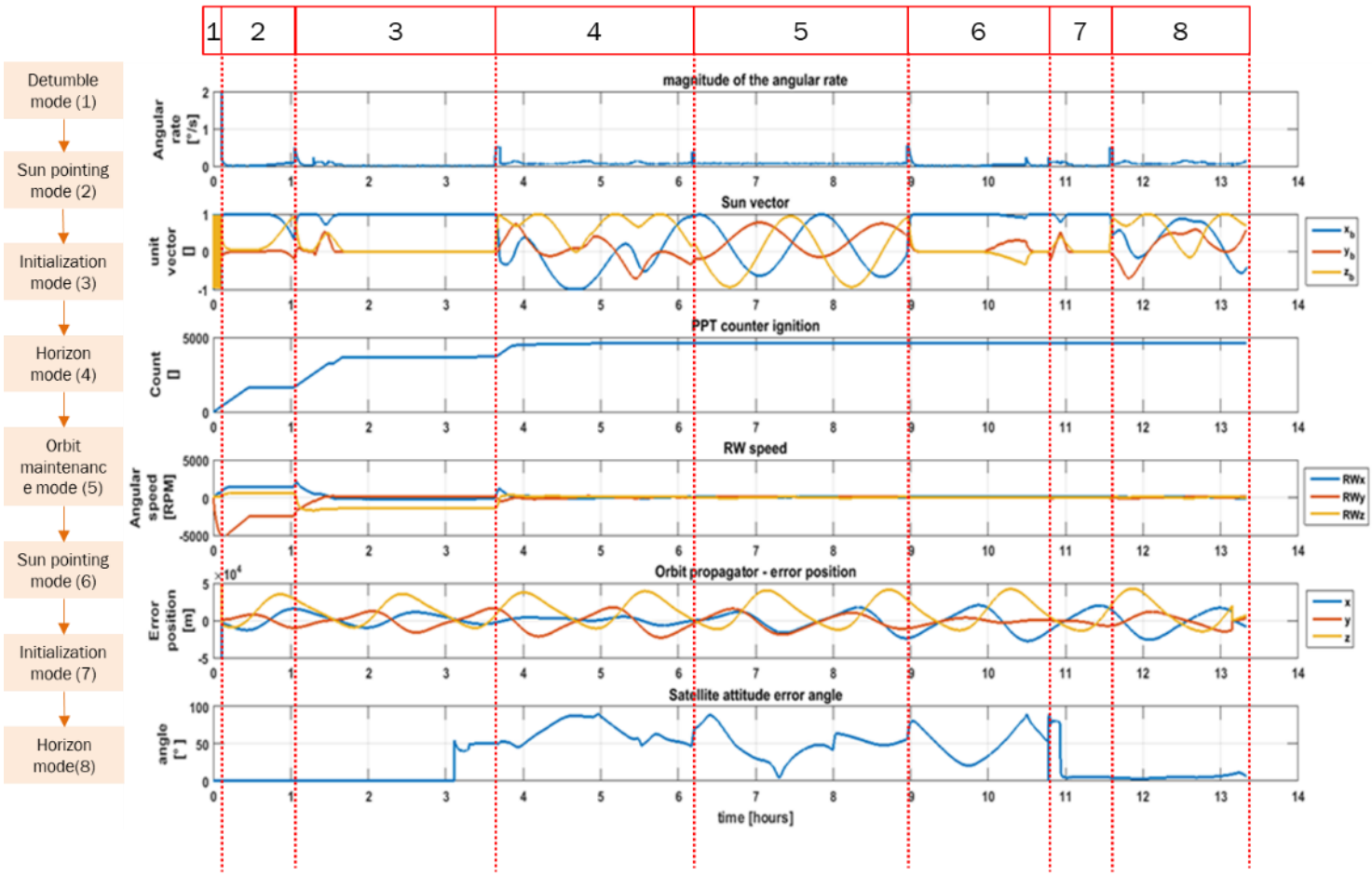

Figure 7.5. Example of data analysis after a simulation run.

Nonetheless, SIL test platform served to identify the elements of AOCS that require improvement and follow-up in the next phases of the validation and verification processes. For example, Figure 7.6 shows a simulation run where the 3D visualization tool was used in order to verify the performance of the AOCS during the horizon detection and orbit maintenance modes. In the early stages of the project, this simulation results served as a reference to develop, test and improve the attitude determination system based on EKF (section 3.2.3) and utilizing sun sensors and gyroscope data.

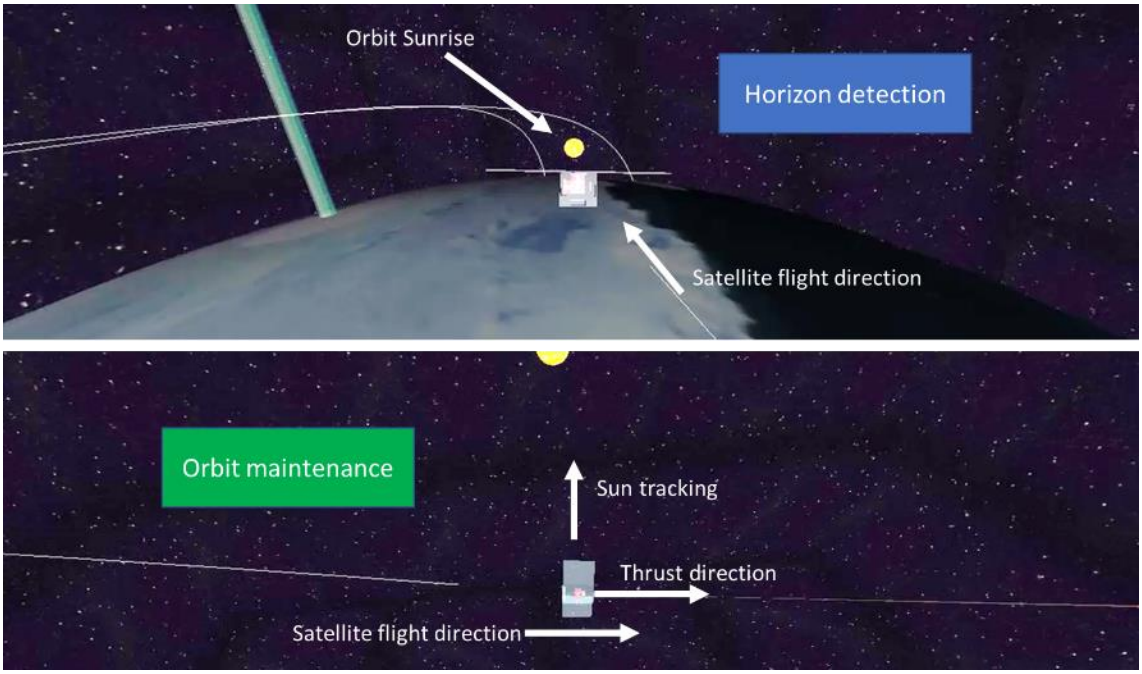

Figure 7.6. 3D visualization of a simulation run, where AOCS was tested in terms of attitude determination and control functionality and accuracy.

7.2 Processor-in-the-Loop (PIL) testbed

PIL consists on either open-loop or close-loop simulation techniques where the AOCS code embedded into the OBC firmware is used (Figure 3.6). It is used to test and verify the performance of the software under test in terms of functionality, execution time, and, in a final stage of the test campaign, the interface with the OBC firmware. The satellite OBC or a development board which contains the same processor as OBC is used. In order to produce the input data, and receive the calculated commands from AOCS code afterwards, a PC is used which can be used either a data acquisition system or a flight simulator.

In Figure 7.7, two main components of this testing platform can be noticed, a PC laptop where the flight simulator developed in MATLAB is installed (section 7.1) and an OBC platform whose processing unit is based on a microcontroller used by the AV4 satellite (section 3.1.1). Through serial communications (wired or wireless), the OBC block sends the calculated control commands from AOCS software to the flight simulator.

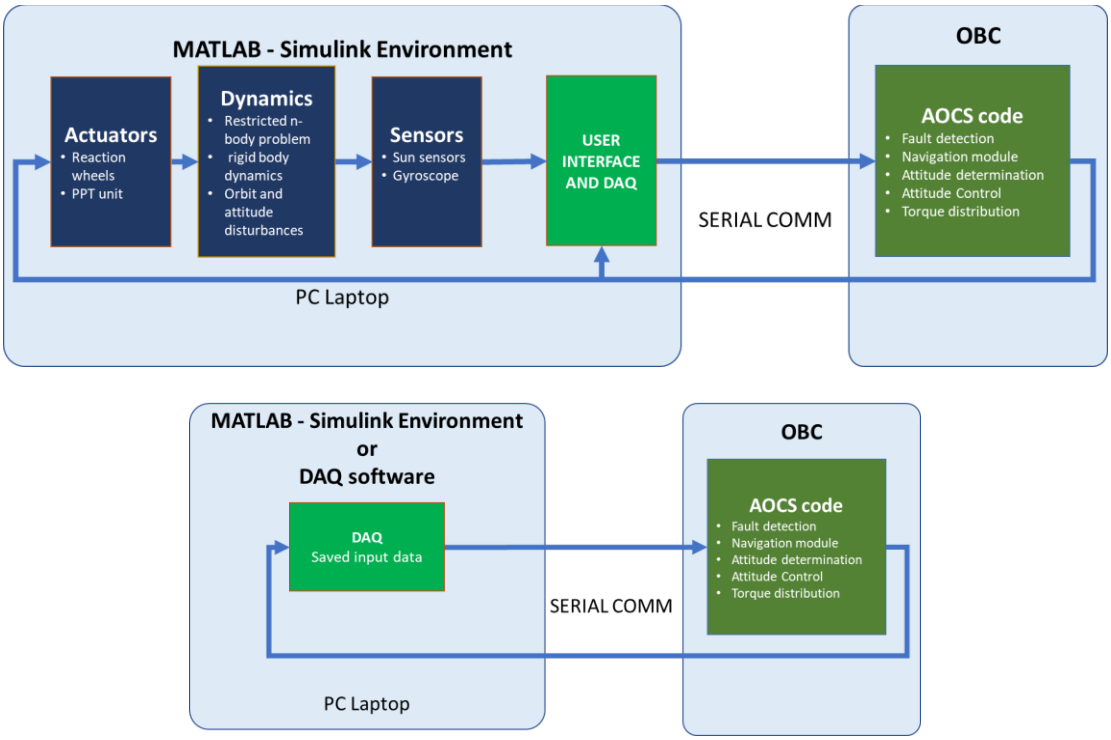

Figure 7.7 (Up) Close-loop configuration of the PIL testbed. (Down) Open-loop configuration of the PIL testbed

In the following tables, the input and output variables of the AOCS software embedded into the OBC (or development board) are shown. The AOCS software receives the simulated sensor inputs from the flight simulator in the specified order and data type. Similarly, the flight simulator receives the resulting commands from AOCS outputs in the specified order. At the beginning and end of each data string, a header and terminator must be specified.

Table 7.2 Inputs of AOCS software

AOCS External inputs variables			
Variable	**Type**	**Size (in bytes)**	**Description**
HEADER [4]	int16	8	value=0xFAFA
IN_TLE_data [8]	float32	32	Contains the following TLE information parameters 9. Year 10. Days 11. Inclination 12. Ascending node 13. Eccentricity 14. Argument of perigee 15. Mean anomaly 16. Mean motion
IN_TLE_data_exp [8]	float32	32	It can contain pre-computed TLE values (same as IN_TLE_data input variable) or state vectors values

			(Position vector, velocity vector, JD time stating from 2017/01/01 00:00:00, 0.0 value) from GS (for research purposes).
IN_gyro[3]	float32	12	Contains the gyroscope information (x, y, z sensor axis)
IN_sun_sensor[14]	Uint16	28	Contains the information of the sun sensor information: IN_sun_sensor [1-6]: The +x, -x, +y, -y, +z, -z coarse sun sensor information will be saved in the specified order. IN_sun_sensor [7-10]: The A, B, C, D section of the -x fine sun sensor will be saved in the specified order. IN_sun_sensor [11-14]: The A, B, C, D section of the -z fine sun sensor will be saved in the specified order.
IN_CPU_time[6]	Uint16	12	The OBC firmware will provide the UTC time information in YY-MM-DD-hh-mm-ss. Any time calibration can be performed.
IN_w_rw[3]	int16	6	Contains the RW speed information (x, y, z body axis)
IN_TLE_data_ack	int16	2	The OBC will indicate to AOCS software that the TLE information was received.
IN_AOCS_cmd	int16	2	Contains the command related with the mode of operation that the satellite will perform: • 0 for detumble (default) • 1 for sun pointing towards solar panel axis • 2 detumble – sun pointing towards solar panel axis automatic change • 3 for sun pointing towards camera axis (Horizon) • 4 for sun pointing towards PPT axis • 5 for initialization mode with sun pointing towards solar panel axis (Attitude determination system initialization) • 6 for horizon pointing strategy • 7 for orbit maintenance maneuvers • Any other value means no control
IN_AV4_mode	int16	2	Indicates the current mode of AV4 • 0 Normal mode • 1 Safe-hold mode • 2 Critical mode
IN_OP_mode	int16	2	Defines the orbit propagator to be used: • 0 for SGP4 propagator • 1 for 2-body orbit propagator • 2 for n-body orbit propagator (for research purposes) • Any other value means OP deactivated
IN_ppt_mode	int16	2	Defines the frequency of PPT ignitions • 0 as fixed (1 Hz as default), • 1 as variable (1 – 4 Hz)
IN_AOCS_reset	int16	2	Clear all buffer variables to default values and set the AOCS mode as default. • 0 normal operation • 1 RESET
TERMINATOR [4]	int16	8	value=0xFFFF
SUBTOTAL		***134***	***Bytes***
FOR DEBUGGING/TESTING PURPOSES (Not available in AV4 OBC)			

IN_st_sim [4]	float32	16	Satellite attitude expressed in quaternions
IN_sB_sim[3]	float32	12	Sun vector in satellite frame
IN_const_sim	int16	2	Constant used during Processor-in-the-loop test

Table 7.3 Outputs of AOCS software

AOCS External outputs variables			
Variable	**Type**	**Size (in bytes)**	**Description**
HEADER [4]	int16	8	value=0xFAFA
OUT_rw[3]	Uint16	6	Contains the RW speed command in x, y and z axis(RPMs).
OUT_rw_spin[3]	int16	6	Indicates the spin direction • 0, counter clockwise spin • 1, clockwise spin
OUT_ppt_ign[4]	int16	8	Contains the PPT vector commands (0 is off as default, 1 for ignition for each head).
OUT_ppt_freq	int16	2	Contains information of PPT ignition frequency in Hz
OUT_TLE_rcv_ack	int16	2	Send acknowledge once the AOCS software receives the TLE information from OBC.
OUT_hrzn_flag	int16	2	Indicates the moment when orbit sunrise or sunset occurs. During horizon mode, it can be used to take picture at this moment. • 0, default • 1, orbit sunrise (eclipse to Sun phase) • 2, orbit sunset (Sun phase to eclipse)
SUBTOTAL		***30***	***Bytes***
OUTPUT VARIABLES FOR ANALYSIS PURPOSES VIA DOWNLINK			
OUT_AOCS_mode	int16	2	Indicates the current AOCS mode of operation
OUT_FDIR_status	int16	2	Indicates when FDIR module detects a sensor fault
OUT_sun_vector[3]	int16	6	Calculated sun vector by using FDIR
OUT_qEKF[4]	int16	8	Calculated attitude of the satellite by using ADS
OUT_wEKF[3]	int16	6	Corrected gyroscope data by using ADS
OUT_s_errorEKF[3]	int16	6	Error between calculated (from sun sensors) and estimated (from EKF) sun vector
OUT_rOP[3]	int16	6	Calculated position of the satellite in inertial frame by using NAV
TERMINATOR [4]	int16	8	value=0xFFFF
SUBTOTAL		***36***	***Bytes***
TOTAL (i/o data)		**200**	**Bytes**

The interface between the development board was made in MATLAB as shown below. The data is received and transmitted via UART communication protocol. The incoming and outcoming data is saved in MATLAB workplace and can be analysed after the PIL test.

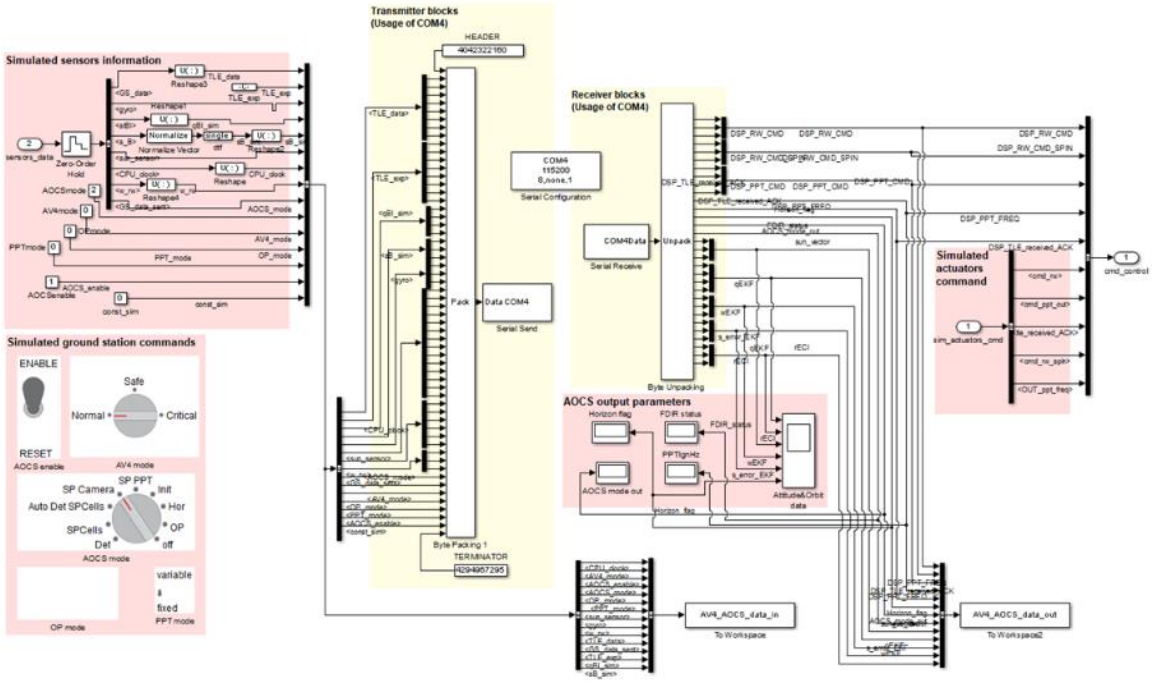

Figure 7.8. Screenshot of the interface between MATLAB simulator and development board

In case of the interface between MATLAB simulator and OBC, NTU team develop an interface as shown below. In addition to the MATLAB interface, an emulator (virtual serial port emulator VSPE) must be installed in the host PC which serves and an interface between MATLAB simulator and Mission Control Center (MCC) software. MCC is used in ground station to receive telemetry and send commands to AV4 in orbit. In case when AOCS software is updated, the OBC firmware must be updated too. To do so, a debug probe (Spectrum Digital XDS200 from Texas Instrument) is used to flash the OBC and program it with the new OBC firmware.

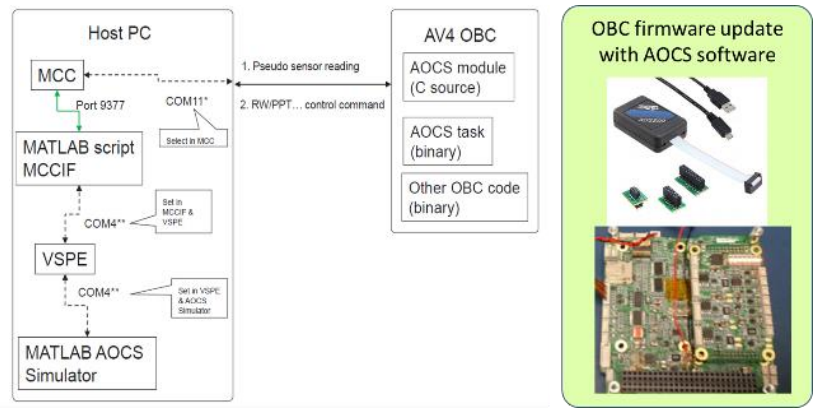

Figure 7.9. Interface between MATLAB simulator and AV4 OBC

7.2.1 Operation of the PIL testing platform

In Figure 7.10, the methodology to verify the AOCS software through PIL technique is shown. Once developed and validated an AOCS algorithm through SIL, it is coded and embedded into the AOCS software. Before updating the OBC firmware with the AOCS software, a development board is used to verify the functionality of the AOCS software. In case when the AOCS needs improvements, the AOCS software is updated and tested it again.

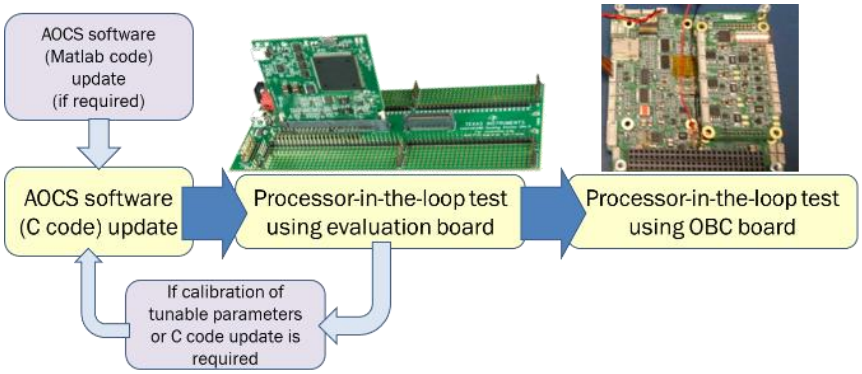

Figure 7.10. Verification process of AOCS software through PIL testing technique.

The verification process was done by confirming the correct execution of the modules according to the flowchart which is shown in Figure 7.11. In the case of orbit propagators and the attitude determination and control algorithms, their performance is also verified,

in terms of accuracy and execution time, and must be the same during the SIL test campaigns.

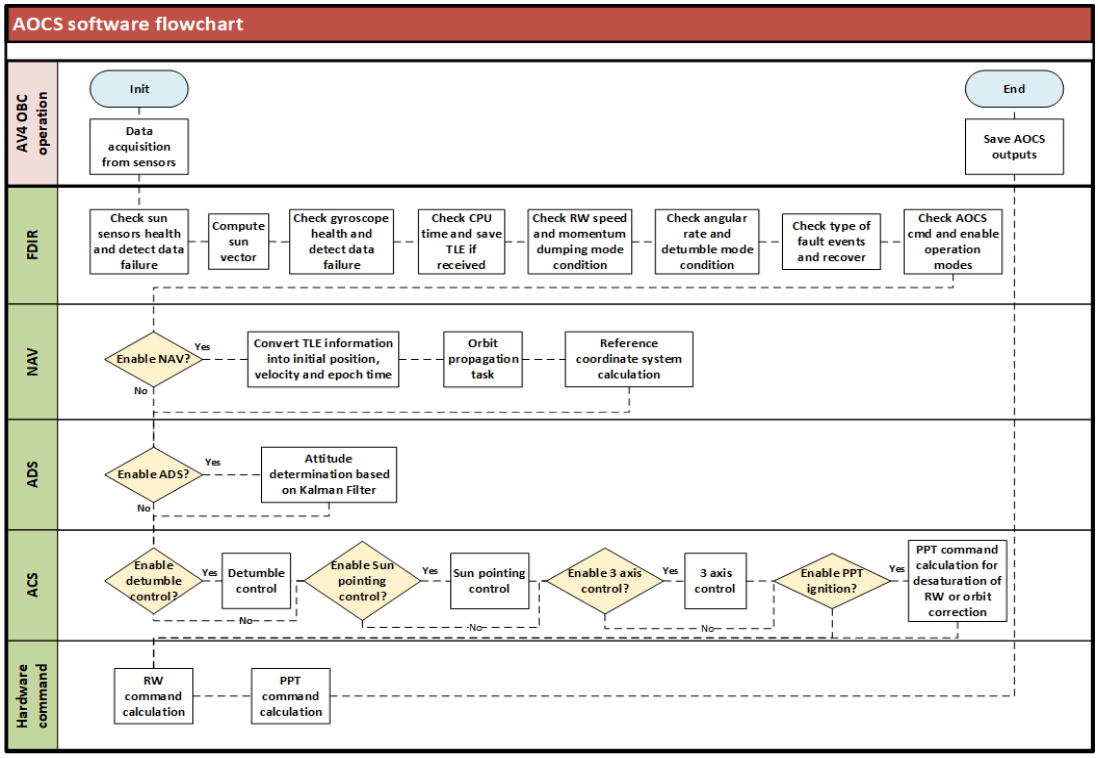

Figure 7.11. AOCS flowchart for the verification of AOCS software.

After the PIL test campaign by using the development board, the execution time of the AOCS code could be measured, as shown in next table. Since AOCS software has several modes of operation, the execution time of each AOCS was measured considering the maximum values obtained for each AOCS mode. It is possible to notice that the most complex algorithm in terms of execution time is the navigation module. For a safe operation, a simple 2-body propagator can be used, at the expense of the propagation accuracy.

Table 7.4. Execution time of each AOCS module.

AOCS subroutine	***Execution time (milliseconds)***
FDIR	0.0182
Navigation	0.05 with 2-body propagation 3.111 with SGP4 (0.1Hz) 20.0 with n-body propagator (0.1Hz)
ADS	1.171
ACS	0.022
AOCS hardware commands	0.012

Additionally, the size of the AOCS code per module could be measured, as shown in the next table.

Table 7.5. Size of each module of AOCS software.

AOCS subroutine	Files	Size on DSP (bytes)
FDIR	Aocs_FDIR.c, Aocs_FDIR.h	5,691
NAV	Aocs_NAV.c, Aocs_NAV.h	18,662
ADS	Aocs_ADS.c, Aocs_ADS.h	14,265
ACS	Aocs_ACS.c, Aocs_ACS.h	2,480
Hardware commands	Aocs_HW_CMD.c, Aocs_HW_CMD.h	1,363
Main	Aocs_code.c, Aocs_code.h	62

As an example of the performance analysis of AOCS software via PIL simulation, the Figure 7.12 shows a simulation run to evaluate the capability of the satellite to reduce its momentum through PPT ignitions. The MATLAB simulator sent the simulated sensor data to the development board, which contains the AOCS software. Then, the actuators commands are sent back the the MATLAB simulator and closing the loop.

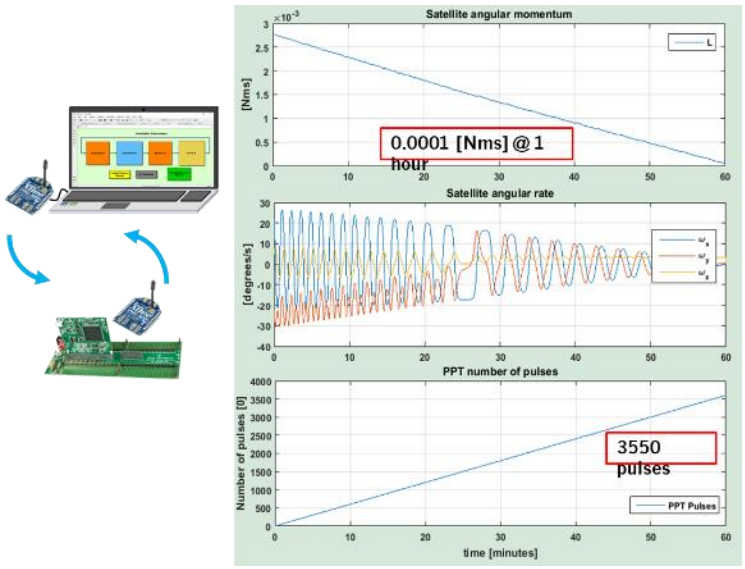

Figure 7.12. Example of a simulation run related with the momentum dumping of the satellite through PPT ignitions via PIL simulation method.

The debugging process (using the development board) could be done via the coding software used for the development of AOCS code in C programming language (Code Composer Studio from Texas Instruments). As shown in the next figure, any variable of the software could be supervised in such a way that, in case of an execution problem, the error source could be found in this way.

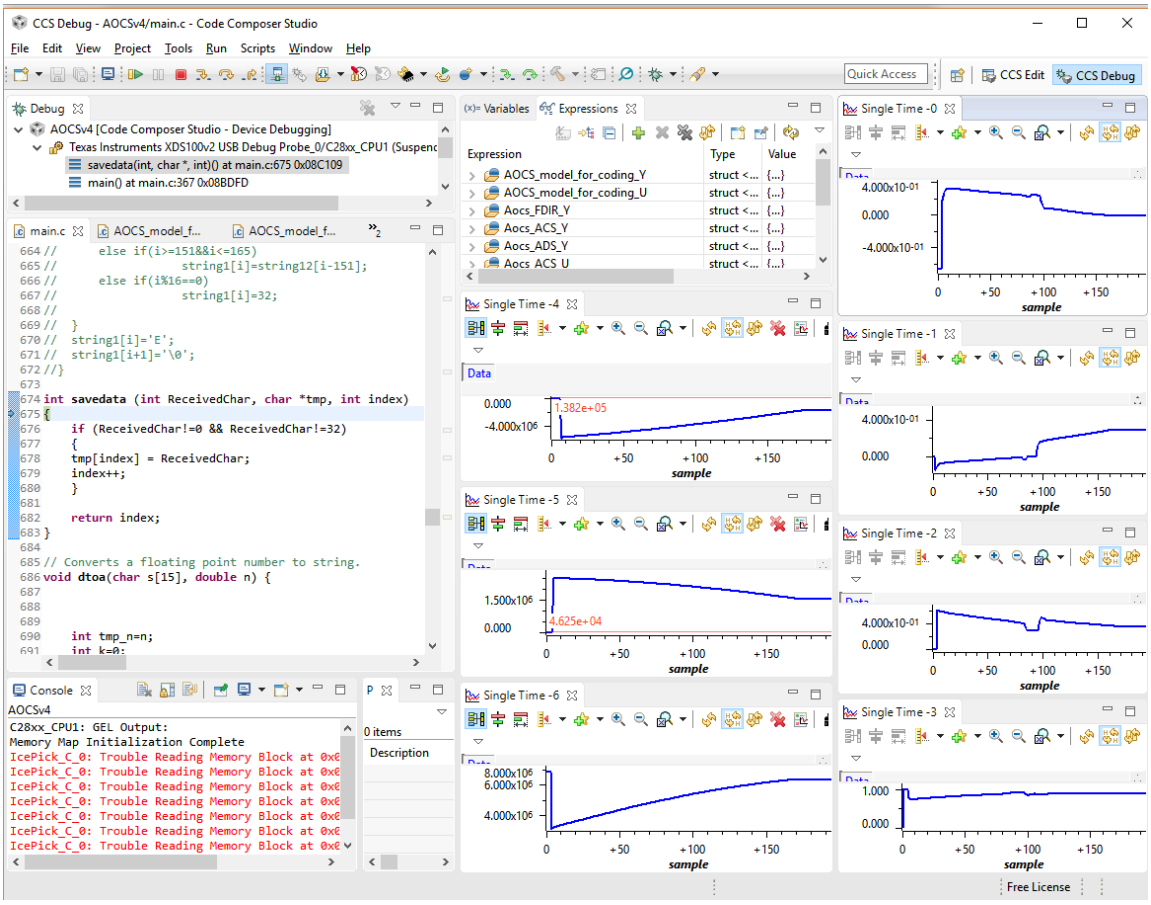

Figure 7.13. Screenshot of the debugging window of coding software Code Composer Studio, used for the debugging process of AOCS software.

When OBC is used, the AOCS code is verified by using the MCC software provided by NTU. Debugging of AOCS code is no longer available and the results obtained through PIL simulation must be the same as for PIL simulation with the development board. In the next figure, a screenshot of MCC is shown, where all the parameter of AV4, including information from other subsystems are displayed.

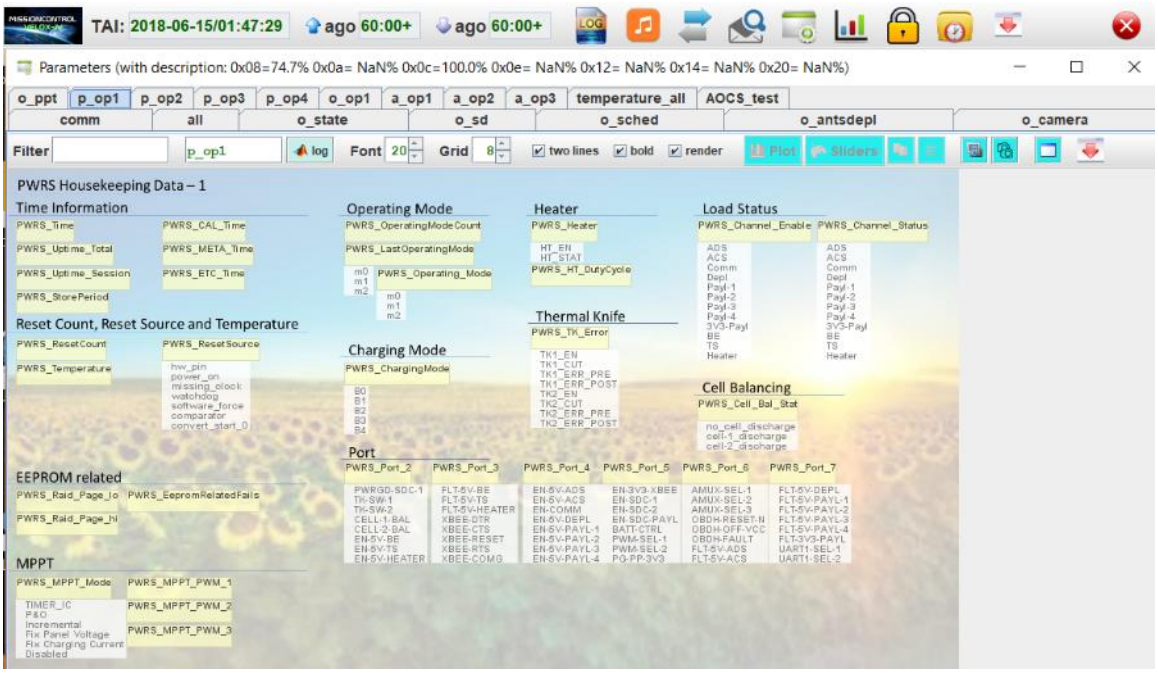

Figure 7.14. Screenshot of the MCC software, developed by NTU and used for the PIL test with the OBC.

7.3 Hardware-in-the-loop (HIL) testbed

Within the verification process of AV4 AOCS software, the HIL simulation technique is used by including real sensors and actuators placed in an air bearing table, which provide a three-axis frictionless movement which is similar in the outer space. In this way, the MATLAB simulator is| no longer required and it is used as data acquisition system only.

In order to verify the AOCS software, the HIL test was performed by considering two options: a functional test with similar attitude hardware as AV4, and the STM model (Figure 7.15). The functional test served to understand the capability and limitations of AOCS in terms of attitude knowledge and attitude correction performance. Additionally, it served as a prototype to develop and improve the PIL and HIL testbeds that must be compatible with the AV4 OBC. Although the HIL testbeds were conceived to operate in vacuum environment, an electric propulsion system was not available. Nonetheless, the HIL test could be performed successfully.

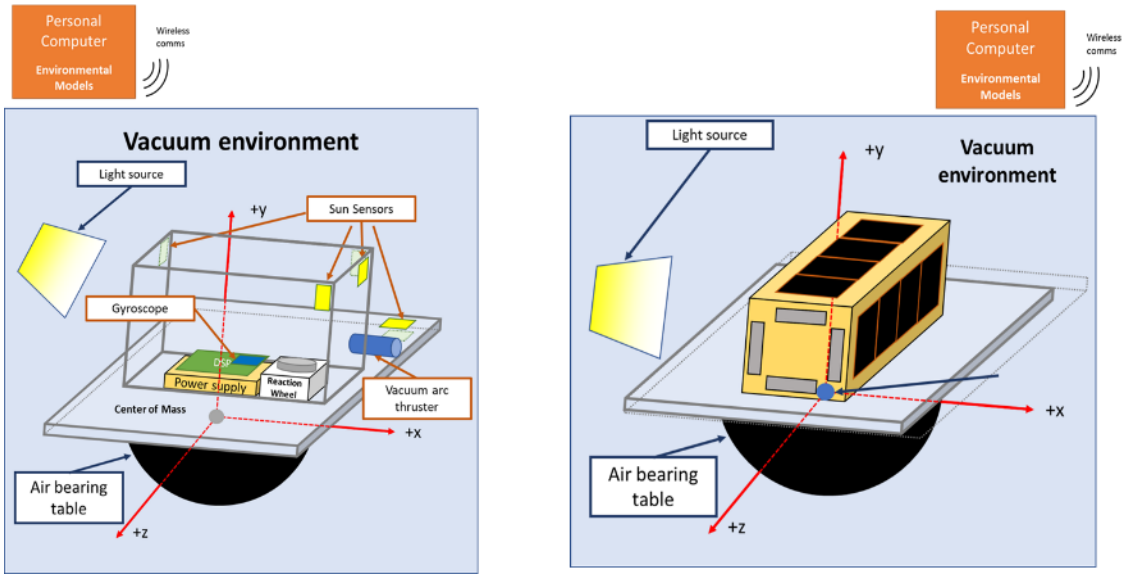

Figure 7.15. The HIL simulation method by using either a functional prototype (left) and the AV4 satellite (right).

The general architecture of the HIL testbed by using the functional prototype is shown in Figure 7.16. Similar to Figure 7.8, the interface between PC and the HIL platform was developed in MATLAB, where it is possible to send and receive data as well as to control the functional prototype. It can be also considered as the ground station since it has the same capabilities to receive telemetry and send commands via wireless communications.

In Figure 7.17, the functional testbed is illustrated, which was used to verify the following features:

- Detumble mode
- Sun tracking mode
- Navigation module
- EKF performance
- Science mode partially verified (PPT not available)

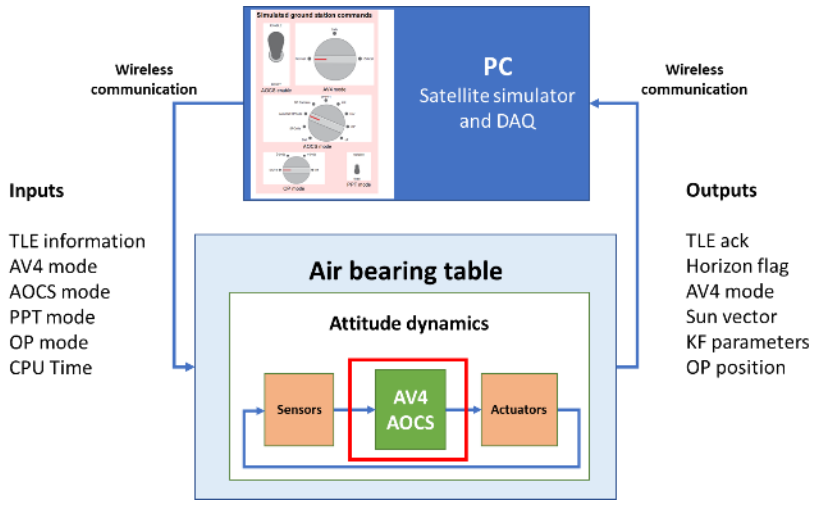

Figure 7.16, General architecture of the HIL testbed by using a functional prototype.

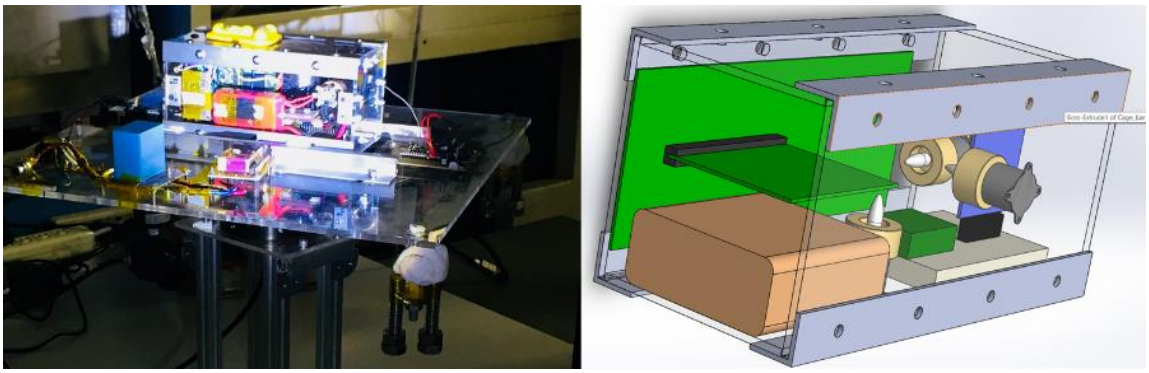

Figure 7.17. The functional prototype developed for the verification of AOCS software.

Regarding the use of AV4 STM in HIL test utilized for the verification of the AOCS software, the following elements were used:

- Air bearing table
- AV4 STM
- Lamp
- Mobile ground station

The air bearing table was balanced through masses (provided by NTU) whose position could be adjusted in such a way that the center of mass could be as close as possible to the center of rotation. The STM was fixed on the table by aluminum rails and PTFE blocks provided by Kyutech. The air bearing table was placed inside a dark room in order to reduce the environment light.

At the beginning of the test procedures, the STM downlink data was obtained through a wire for calibration purposes. Then, the NTU's mobile ground station was used to obtain the downlink data from STM during the test procedures. CSV files were generated during the operation of AV4, which contains the downlink data, including AOCS information, which were used to verify the functionality of AOCS software by operation the AV4 STM through the mobile ground station.

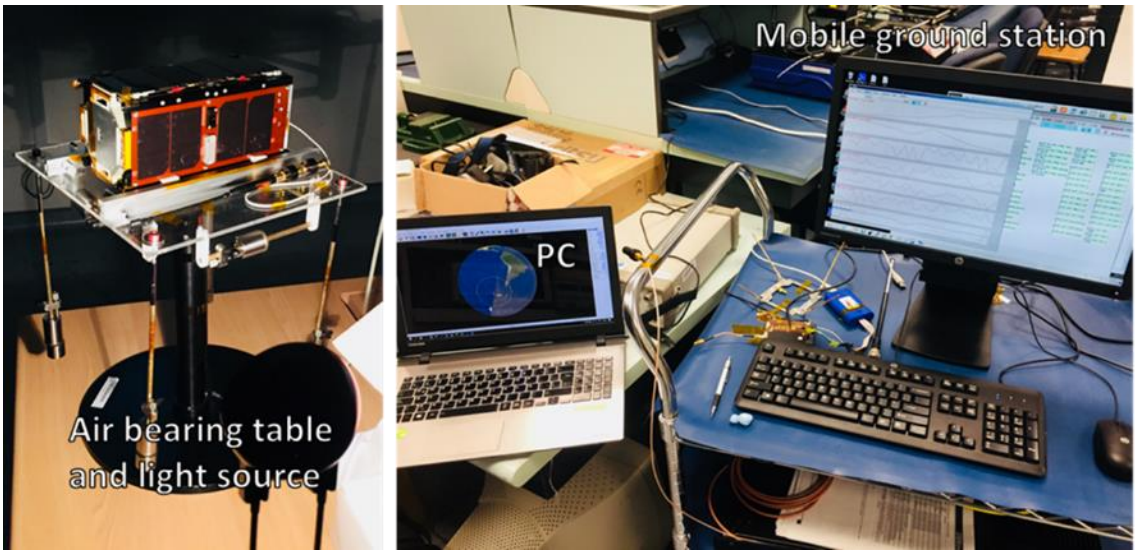

Figure 7.18. The HIL testbed using the AV4 STM and the mobile ground station from NTU.

After the test campaign of AV4 STM, the results obtained are listed as follows:

Test item	Results
Functionality test of the AV4 STM	• The STM could not be placed in vertical position on the air bearing table. Hanging up the STM was also not feasible. Instead, the Z-axis was tested by inducing disturbances on the air bearing table and checking the RWz response. • The weight of the testbed (STM + air bearing table) was too large for the RW. They reached their saturation very fast. So large attitude maneuvers were not possible. • A residual spin of the platform was present during each test, which leaded to the saturation of the RWy after few minutes. • A wireless communication via XBee modules were not feasible. Instead, the NTU's mobile ground station was used; however, the AOCS data could not be retrieved during the first test. This issue was updated and AOCS data can be downloaded during the mission. • AOCS was not initialized after turning on the STM due to the RESET command was enabled as default. That issue was fixed. • The AOCS tunable parameters could not be adjusted. This issue was fixed.
Sensor data health check, including the bias of the gyroscope	• Z-axis fine sun sensor was not available. • Y- axis coarse sun sensor was disconnected. We overcame that issue by placing the Y-axis STM in nadir position. • The bias of the gyroscope was too large and had been calibrated before each test. We also observed that the bias varies slightly after turning on the STM. For the flight model, we must check the bias values and calibrate. • The AOCS fault detection conditions were updated. If "no control" was selected and if AOCS detected a sensor failure, the AOCS mode was changed to "sun pointing" mode.

Calculation of the sun vector	• AOCS was expecting unsigned integer values from the fine sun sensor; however, OBC was sending signed integer values, causing miscalculations of the sun vector. That issue was solved by updating the AOCS instead of the OBC firmware.
Actuator response against a control command from AOCS	• The RWz was spinning in an opposite direction as specified by Richard in his last email regarding the AOCS. I tried to correct the spin direction via the AOCS tuning parameters but had no effect. This issue was solved by updating the AOCS. • The PPT ignition command was updated according to the latest information of the position of each PPT heads.
Detumble	• Correct operation, but control gains were adjusted
Sun-pointing	• Correct operation, but control gains were adjusted
AOCS default mode of operation (Auto change from detumble to sun tracking)	• Correct operation. We also move the light source to verify the sun-tracking capability of the STM.
Horizon mode through sun tracking controller (medium priority)	• Not fully completed since it required a 90 degrees attitude maneuver and RW become saturated; however, I verified that mode of operation in Kyutech by using our own testing platform and the AV4 OBC.
Conditions to activate the Momentum reduction controller (medium priority)	• Correct operation.

Since there were updates on the OBC firmware of the STM during the test, the AV4 flight model firmware must be updated too. In order to proceed with the update of the AV4's OBC, the following items were scheduled and performed in the following sequence:

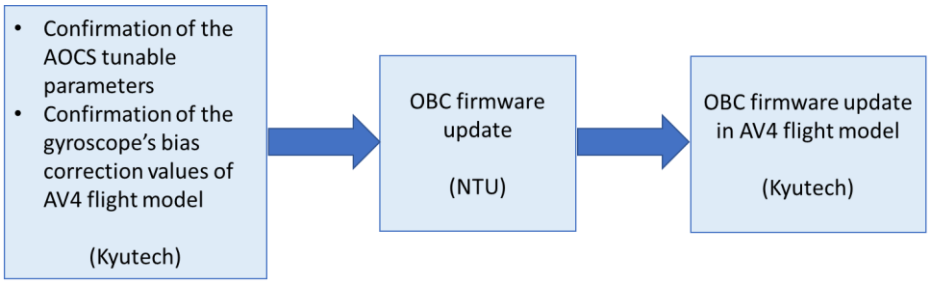

The AOCS default tunable parameters were sent to NTU after their verification by using the Kyutech PIL testbed, with the AV4 calculated moment of inertia and estimate the time of each attitude maneuver.

The gyroscope's bias values of AV4 flight model were verified before updating the OBC firmware. The AV4 flight model was used with the MCC software. Through video conference, NTU supervised this task. Then, the gyroscope's bias correction values were sent to NTU.

After updating the OBC firmware, Kyutech (with NTU connected via video conference) flashed the AV4 OBC (FM).

CHAPTER 8. CONCLUSIONS AND FUTURE WORK

This research made a valuable contribution to the development of testing platforms for the full validation and verification of AOCS systems in laboratory, where AV4 satellite served as a device under test.

The validation test was performed via SIL test method. Through a flight simulator developed in MATLAB Simulink, the AOCS software was developed to meet the mission requirements of AV4, which are the momentum dumping through PPT ignitions, the observation of the Earth rim and orbit correction maneuvers, considering the available attitude sensors and actuators.

Then, development of PIL testbed served as a tool for verification process of AOCS software written in C code. The simulation results obtained through SIL and PIL tests must be the same. By using the development board (which contains the same micro-controller as AV4 OBC), it was possible to perform debugging routines and execution errors could be detected and solved. As the last stage of PIL simulation, the AV4 OBC was used to test the AOCS software which was embedded into the OBC firmware. In this stage, the correct execution of OBC firmware with the AOCS software, as well as the interface with the MCC software (the software used in ground station to send commands and receive telemetry of AV4 in orbit).

The HIL testbed was useful to demonstrate the capabilities of AOCS software by using a prototype with similar AOCS hardware, as well as the AV4 STM. This testing procedures served to verify the operation of AV4 by using its AOCS in a functional prototype and the STM model placed on an air bearing table. Regarding the use of the AV4 STM, even when the overall weight of the testbed was too large for the AV4 RWs, the verification of the detumble and sun-tracking control algorithms were done, as well as the momentum reduction controller by simulating the torque induced by PPT ignitions through manual disturbances on the air bearing table (the PPT module could not be activated in STM model due to a failure in the OBC board). Also, several issues related with the interface between AOCS software, OBC and MCC software were found and solved successfully by updating

the OBC firmware (including the AOCS software and default values) and the MCC. Therefore, the OBC of the AV4 flight model was flashed with the new firmware afterwards. From the test results and following updates on the OBC firmware and its AOCS software, the risk of any anomaly related with the operation of AV4 in orbit by using its AOCS was reduced.

Regarding the numerical demonstration of the mission lifetime extension capability of a CubeSat equipped with PPT in lunar orbit, this research made a valuable contribution by demonstrating the feasibility on the extension of mission lifetime, which is limited by the satellite's inclination and features of an electric propulsion system. Even if a CubeSat is deployed into the unstable regions, it is feasible to overcome the unstable orbit condition by performing orbit correction maneuvers to guarantee a long lunar mission lifetime and extend the possibilities of a successful mission for a CubeSat. Further development of electric propulsion systems with higher I_{bit} and ΔV values will enhance the orbit correction capabilities of future CubeSat missions.

Future work

Even when the validation of verification of AV4 AOCS through several testing methods including SIL, PIL and HIL, were performed successfully, the electric propulsion system as part of the attitude actuator of AV4 was not available for testing; however, the momentum dumping algorithm could be verified by inducing manual disturbances on the air bearing table. As a future work, an electric propulsion system must be developed and integrated on the air bearing table to demonstrate its capability to reduce the momentum of the satellite body and RW in a HIL simulation.

Further improvements in the satellite simulator can be performed in several modules, such as orbital and attitude dynamics, actuators and sensor models, and interface with the device under test (either a satellite or a functional prototype), in terms of execution speed and efficiency (orbital propagator), simulation accuracy (actuators and sensor models) and appearance (through a user interface). For further satellite projects, this simulator is a valuable tool to validate any AOCS algorithm. Also, the functional prototype developed for this project can also be used for educational purposes. Therefore, further improvements in circuitry, structure or case, and the user interface are needed.

Regarding the feasibility analysis for the extension of mission lifetime of a CubeSat orbiting the Moon, this research assumes scenarios where attitude and orbital ephemeris are known. Therefore, this research can be improved by considering the technical

limitations of a CubeSat to determine its attitude and orbit with the available state-of-the-art attitude hardware and capabilities of a deep space ground station network to determine the spacecraft orbit, in order to achieve the extension of mission lifetime reported in this research.

CHAPTER 9. REFERENCES

[1] K. Lemmer, «Propulsion for CubeSats,» *Acta Astronautica,* vol. 134, pp. 231-243, 2017.

[2] B. Yost, "State of the Art of Small Spacecraft Technology, 04. Propulsion," 12 04 2019. [Online]. Available: https://sst-soa.arc.nasa.gov/04-propulsion. [Accessed 27 04 2019].

[3] D. Lev, R. M. Myers, K. M. Lemmer, J. Kolbeck, M. Keidar, H. Koizumi, H. Liang, D. Yu, T. Schnherr, J. G. del Amo, W. Choe, R. Albertoni, A. Hoskins, S. Yan, W. Hart, R. R. Hofer, I. Funaki, A. Lovtsov, K. Polzin, A. Olshanskii and O. Duchemin, "The technological and commercial expansion of electric propulsion in the past 24 years," in *35th International Electric Propulsion Conference*, Georgia Institute of Technology, Atlanta, Georgia, United States of America, 2017.

[4] M. Benetti, *Feasibility study of an electrospray propulsion system for a 6U CubeSat to the Moon,* Politecnico di Milano, Italy: Master Thesis, 2017.

[5] A. R. Tummala and A. Dutta, "An Overview of Cube-Satellite Propulsion Technologies and Trends," *Aerospace,* vol. 4, no. 4, 2017.

[6] H. Koizumi, J. Asakawa, Y. Nakagawa, S. Kojima, H. Kawahara, K. Komurasaki, M. Nakano, H. Sahara, M. Banno, J. Matsushima, M. Kaku, T. Iizuka and Y. Seto, "Micropropulsion Systems Enabling Full Active Debris Removal by a Small Satellite ADRAS-1," in *30th annual AIAA/USU Conference on small satellites,* Logan, Utah, United States, 2016.

[7] C. P. Bridges, S. Kenyon, P. Shaw, L. Visagie, T. Theodorou y B. Yeomans, «A baptism of fire: The STRaND-1 nanosatellite,» de *7th Annual AIAA/USU Conference on Small Satellites*, Logan, Utah, United States, 2013.

[8] "Tag Archives: Wren," AMSAT-UK, [Online]. Available: amsat-uk.org/tag/wren/. [Accessed May 2018].

[9] M. Keidar, «Micro-Cathode Arc Thruster for small satellite propulsion,» de *IEEE Aerospace Conference*, Montana, United States, 2016.

[10] G. Figueiró, «SERPENS CubeSat Mission,» de *11th Annual CubeSat Developers Workshop*, United States, 2014.

[11] "AOBA VELOX-III," Satellite Research Centre, NTU, Singapore, [Online]. Available: www.sarc.eee.ntu.edu.sg/Research/Projects/Pages/Aoba-Velox-III.aspx. [Accessed May 2018].

[12] C. Scharlemann, B. Seifert, D. Kohl, D. Birschitzky, L. Gury, F. Kerschbaum, C. Obertscheider, R. Ottensamer, A. Reissner, T. Riel, R. Sypniewski, M. Taraba, R. Trausmuth y T. Turetschek, «PEGASUS - An Austrian Nanosatellite for QB50,» de *EGU General Assembly Conference*, Vienna, Austria, 2015.

[13] H. S. Ousaloo, M. T. Nodeh and R. Mehrabian, "Verification of Spin Magnetic Attitude Control System using air-bearing-based attitude control simulator," *Acta Astronautica,* vol. 126, pp. 546-553, 2016.

[14] M. Paluszek, S. Thomas, J. Mueller and P. Bhatta, Spacecraft Attitude and Orbit Control, Princeton Satellite Systems Incorporated, 2009.

[15] S. Corpino and F. Stesina, "Verification of a CubeSat via Hardware-in-the-loop Simulation," *IEEE Transactions on Aerospace and Electronic Systems,* vol. 50, no. 4, 2014.

[16] M. Ghorbani, M. Pasand, A. G. Bayati and N. Baheri, "Real-Time Hardware-in-the-Loop test for a Small Uper Stage Embedded Control System," in *The CSI International Symposium on Real-Time and Embedded Systems and Technologies,* Tehran, Iran, 2018.

[17] J. L. Schwartz, M. A. Peck and C. D. Hall, "Historical Review of Air-Bearing Spacecraft Simulators," *Journal of Guidance, Control, and Dynamics,* vol. 26, no. 4, pp. 513-522, 2003.

[18] A. Macedo de Oliveira, H. K. Kuga and V. Carrara, "Air bearing platforms for simulation of spacecraft attitude control systems," in *DINAME 2015 - Proceedings of the XVII International Symposium on Dynamic Problems of Mechanics,* Natal, Rio Grande do Norte, Brazil, 2015.

[19] D. Y. Lee, H. Park, M. Romano and J. Cutler, "Development and experimental validation of a multi-algorithmic hybrid attitude determination and control system for a small satellite," *Aerospace Science and Technology,* vol. 78, pp. 494-509, 2018.

[20] D. C. Sternberg, C. Pong, N. Filipe, S. Mohan, S. Johnson and L. Jones-Wilson, "Jet Propulsion Laboratory Small Satellite Dynamics Testbed Simulation: On-Orbit Performance Model Validation," *Journal of Spacecraft and Rockets,* vol. 55, no. 2, pp. 322-334, 2018.

[21] K. Seweryn, T. Barciński, M. Ciesielska, J. Grygorczuk, T. Rybus, K. Skup and R. Wawrzaszek, "Validation of the control strategy of the free flying robot – application to the rendezvous manoeuvres," in *Proceedings of the12th Symposium on Advanced Space Technologies in Robotics and Automation (ASTRA'2013),* Noordwijk, The Netherlands, 2013.

[22] J. J. Rennilson and D. R. Criswell, "Surveyor observations of lunar horizon-glow," *The Moon,* vol. 10, no. 2, pp. 121-142, 1974.

[23] D. R. Criswell, «Horizon-glow and the motion of lunar dust,» *In Photon and particle interactions with surfaces in space,* vol. 37, pp. 545-556, 1973.

[24] J. E. McCoy, "Photometric studies of light scattering above the lunar terminator from Apollo solar corona photography," *Lunar and Planetary Science Conference Proceedings,* vol. 7, pp. 1087-1112, 1976.

[25] D. A. Glenar, T. J. Stubbs, M. J. E. and V. R. R., "A reanalysis of the Apollo light scattering observations, and implications for lunar exospheric dust," *Planetary and Space Science,* vol. 59, p. 1695–1707, 2011.

[26] H. A. Zook and J. E. McCoy, "Large Scale Lunar Horizon Glow and a High Altitude Lunar Dust Exosphere," *Geophysical Research Letters,* vol. 18, no. 11, pp. 2117-2120, 1991.

[27] T. J. Stubbs, D. A. Glenar, Y. Wang, M. T. P., M. D. C., K. J. W. and t. L. P. S. Team, "Searching for Lunar Horizon Glow with the LRO Star Tracker Cameras," in *47th Lunar and Planetary Science Conference*, The Woodlands, Texas, United States, 2016.

[28] D. A. Vallado and W. D. McClain, Fundamentals of Astrodynamics and Applications, Second ed., Microcosm Press, 2004.

[29] H. Curtis, Orbital Mechanics for Engineering Students, First ed., Elsevier Butterworth-Heinemann, 2005.

[30] I. Reda and A. Andreas, "Solar position algorithm for solar radiation applications," Technical Report, National Renewable Energy Laboratory, United States, 2008.

[31] B. A. Archinal, M. F. AHearn, E. Bowell, A. Conrad, G. J. Consol-magno, R. Courtin, T. Fukushima, D. Hestroffer, J. L. Hilton, G. A. Krasinsky, G. Neumann, J. Oberst, P. K.

Seidelmann, P. Stooke, D. J. Tholen, P. C. Thomas and I. P. Williams, "Report of the IAU working group on cartographic coordinates and rotational elements: 2009," *Celestial Mechanics and Dynamical Astronomy,* vol. 109, no. 2, p. 101–135, 2010.

[32] S. Gupta and R. K. Sharma, "Effect of altitude, right ascension of ascending node and inclination on lifetime of circular lunar orbits," *International Journal of Astronomy and Astrophysics,* vol. 1, no. 3, pp. 155-163, 2011.

[33] H. Schaub and J. L. Junkins, Analytical mechanics of aerospace systems, AIAA Education Series, 2009.

[34] J. B. Kuipers, Quaternions and Rotation Sequences, Princeton University Press, 1999.

[35] F. L. Markley and J. L. Crassidis, Fundamentals of Spacecraft Attitude Determination and Control, United States: Springer-Verlag New York, 2014.

[36] D. B. Guettler, *Satellite Attitude Control Using Atmospheric Drag*, United States: Master Thesis, Air Force Institute of Technology, 2007.

[37] T. S. Kelso, "NORAD Two-Line Element Sets," CelesTrak, [Online]. Available: https://www.celestrak.com/NORAD/elements/. [Accessed May 2018].

[38] S. W. Smith, Digital Signal Processing: A Practical Guide for Engineers and Scientists, Newnes, an imprint of Elsevier Sicence, 2003.

[39] R. Azor, I. Y. Bar-Itzhack and R. R. Harman, "Satellite Angular Rate Estimation from Vector Measurements," *Journal of Guidance, Control, and Dynamics,* vol. 21, no. 3, pp. 450-457, 1998.

[40] M. J. Sidi, Spacecraft Dynamics and Control, A Practical Engineering Approach, Cambridge University Press, 1997.

[41] F. R. Hoots and R. L. Roehrich, "Spacetrack Report No. 3, Models for Propagation of NORAD Element Sets," Aerospace Defense Command, United States Air Force, United States, 1980.

[42] J. Kiusalaas, Numerical methods in engineering with Python, Cambridge University Press, 2005.

[43] A. Ruggiero, P. Pergola, S. Marcuccio and M. Andrenucci, "Low-thrust maneuvers for the efficient correction of orbital elements," in *32nd International Electric Propulsion Conference*, Wiesbaden, Germany, 2011.

[44] R. D. Falck and W. K. Sjauw, "Comparison of low-thrust control laws for application in planetocentric space," in *50th AIAA/ASME/SAE/ASEE Joint Propulsion Conference*, American Institute of Aeronautics and Astronautics, Ohio, United States of America, 2011.

[45] T. E. Xiang, "Design and on-orbit performance of the attitude determination and control system for the ZDPS-1A pico-satellite," *Acta Astronautica,* vol. 77, pp. 182-196, 2012.

[46] R. G. Brown, Introduction to Random Signal Analysis and Kalman Filtering, John Wiley & Sons, 1983.

[47] M. S. E. Grewal, Kalman Filtering: Theory and Practice using MATLAB, John Wiley and Sons, 2001.

[48] K. Xiong, T. Liang and L. Yongjun, "Multiple model Kalman filter for attitude determination of precision pointing spacecraft," *Acta Astronautica,* vol. 68, no. 7-8, pp. 843-852, 2011.

[49] X. Tang, Z. Liu and J. Zhang, "Square-root quaternion cubature Kalman filtering for spacecraft attitude estimation," *Acta Astronautica,* vol. 76, pp. 84-94, 2012.

[50] I. y. Bar-Itzhack and Y. Oshman, "Attitude Determination from Vector Observations: Quaternion Estimation," *IEEE Transactions on Aerospace and Electronic Systems,* Vols. AES-21, no. 1, pp. 128-136, 1985.

[51] B. Wie, Space Vehicle Dynamics and Control, AIAA Education series, 2008.

[52] A. S. Konopliv, R. S. Park, D.-N. Yuan, S. W. Asmar, M. M. Watkins, J. G. Williams, E. Fahnestock, G. Kruizinga, M. Paik, D. Strekalov, N. Harvey, D. E. Smith and M. T. Zuber, "The JPL lunar gravity field to spherical harmonic degree 660 from the GRAIL primary mission," *Journal of Geophysical Research: Planets,* vol. 118, p. 1–20, 2013.

[53] M. Lara, "Design of long-lifetime lunar orbits: A hybrid approach," *Acta Astronautica,* vol. 69, p. 186–199, 2011.

[54] D. Folta and D. Quinn, "Lunar frozen orbits," in *AIAA/AAS Astrodynamics Specialist Conference and Exhibit*, Colorado, United States, 2006.

[55] J. R. Cordova-Alarcon, N. C. Orger, S. Kim, A. W. Ai-Ling, T. Quang-Vinh, B. T. Duy-Vu, L. Soon and M. Cho, "Overview of Aoba VELOX IV missions; pulsed plasma thruster attitude and orbit control and earth-rim night image capture for a future lunar mission," in *The 7th Nano Satellite Symposium and The 4th UNISEC Global Meeting*, Varna, Bulgaria, 2016.

[56] A. D. Perez, "Lunar orbit stability for small satellite mission design," in *4th Interplanetary CubeSat Workshop*, London, United Kingdom, 2015.

[57] O. Zeile, M. Lachenmann, E. Baumstark, A. Mohr, D. Bock, R. Laufer, N. Sneeuw and H.-P. Roeser, "Analyses of orbital lifetime and observation conditions of small lunar satellites," *Acta Astronautica,* vol. 66, p. 516–527, 2010.

[58] Y.-J. Song, S.-i. Ahn y E.-S. Sim, «Development strategy of orbit determination system for korea's lunar mission: lessons from ESA, JAXA, ISRO and CNSA's experiences,» *J. Astron. Space Sci.,* vol. 31, nº 1, pp. 247-264, 2014.

[59] Y.-R. Kim, Y.-J. Song, J. Bae y B.-Y. Kim, «Influence of the choice of lunar gravity model on orbit determination for lunar orbiters,» *Math. Probl Eng.,* vol. 2018, p. 17, 2018.

[60] Spectrolab, "29.5% NeXt triple junction (XTJ) solar cells, Datasheet," 2018. [Online]. Available: http://www.spectrolab.com/DataSheets/cells/PV XTJ Cell 5-20-10.pdf. [Accessed 9 January 2018].

[61] W. K. Vaneman, "The system of systems engineering and integration "Vee" model," in *2016 Annual IEEE Systems Conference (SysCon)*, Orlando, Florida, United States, 2016.

[62] C. Hahn, "Implementing Hardware-in-the-Loop (HIL) Test Systems," National Instruments, [Online]. Available: https://www.fairfield.edu/media/fairfielduniversitywebsite/documents/academic/soe_chahn2-09.ppt. [Accessed 05 2018].

[63] B. O. Andresen, C. Gron, R. H. Knudsen, C. Nielsen, K. K. Sorensen and D. Taagaard, "Attitude Control System for AAUSAT-II," Aalborg University, Institute of Electronic Systems, Aalborg, Denmark, 2005.

[64] C. D. Brown, Elements of Spacecraft Design, AAIA Education Series, 2002.

[65] M. Kabganian, M. Nabipour y F. F. Saberi, «Design and implementation of attitude control algorithm of a satellite on a three-axis gimbal simulator,» *Proceedings of the Institution of Mechanical Engineers, Part G: Journal of Aerospace Engineering,* vol. 0, nº 0, pp. 1-15, 2014.

[66] M. K. Quadrino, D. Miller and K. Cahoy, "Testing the Attitude Determination and Control of a CubeSat with Hardware-in-the-Loop, Master Thesis," Massachusetts Institute of Technology, Massachusetts, United States, 2014.

[67] W. W. Whitacre, "An Autonomous Underwater Vehicle as a Spacecraft Attitude Control Simulator," in *International Astronautical Congress*, Vancouver, Canada, 2004.

[68] E. T. Bradley, "Testing a CubeSat Attitude Control System in Microgravity Conditions," NASA, 2018. [Online]. Available: https://flightopportunities.nasa.gov/technologies/101/. [Accessed 07 2018].